The Young and Nearby Normal Type Ia Supernova 2018gv: UV-optical Observations and the Earliest Spectropolarimetry

Yi Yang (杨轶)[1], Peter Hoeflich[2], Dietrich Baade[3], Justyn R. Maund[4], Lifan Wang[5,6], Peter. J. Brown[5],
Heloise F. Stevance[7], Iair Arcavi[8], Jamison Burke[9,10], Aleksandar Cikota[11], Alejandro Clocchiatti[12], Avishay Gal-Yam[1],
Melissa. L. Graham[13], Daichi Hiramatsu[9,10], Griffin Hosseinzadeh[9,10,14], D. Andrew Howell[9,10], Saurabh W. Jha[15,16],
Curtis McCully[9], Ferdinando Patat[3], David. J. Sand[17], Steve Schulze[1], Jason Spyromilio[3], Stefano Valenti[18],
József Vinkó[19,20,21], Xiaofeng Wang[22], J. Craig Wheeler[21], Ofer Yaron[1], and Jujia Zhang[23,24]

[1] Department of Particle Physics and Astrophysics, Weizmann Institute of Science, Rehovot 76100, Israel; yiyangtamu@gmail.com
[2] Department of Physics, Florida State University, Tallahassee, FL 32306-4350, USA
[3] European Southern Observatory, Karl-Schwarzschild-Str. 2, D-85748 Garching b. München, Germany
[4] Department of Physics and Astronomy, University of Sheffield, Hicks Building, Hounsfield Road, Sheffield S3 7RH, UK
[5] George P. and Cynthia Woods Mitchell Institute for Fundamental Physics & Astronomy, Texas A. & M. University, 4242 TAMU, College Station, TX 77843, USA
[6] Purple Mountain Observatory, Chinese Academy of Sciences, Nanjing 210008, People's Republic of China
[7] Department of Physics, University of Auckland, Private Bag 92019, Auckland, New Zealand
[8] The Raymond and Beverly Sackler School of Physics and Astronomy, Tel Aviv University, Tel Aviv 69978, Israel
[9] Las Cumbres Observatory, 6740 Cortona Drive, Suite 102, Goleta, CA 93117-5575, USA
[10] Department of Physics, University of California, Santa Barbara, CA 93106-9530, USA
[11] Physics Division, Lawrence Berkeley National Laboratory, 1 Cyclotron Road, Berkeley, CA 94720, USA
[12] Instituto de Astrofisica, Pontificia Universidad Catolica (PUC), Casilla 306, Santiago 22, Chile
[13] Department of Astronomy, University of Washington, Box 351580, U.W., Seattle, WA 98195, USA
[14] Harvard-Smithsonian Center for Astrophysics, 60 Garden Street, Cambridge, MA 02138, USA
[15] Department of Physics and Astronomy, Rutgers, the State University of New Jersey, 136 Frelinghuysen Road, Piscataway, NJ 08854, USA
[16] Center for Computational Astrophysics, Flatiron Institute, 162 5th Avenue, New York, NY 10010, USA
[17] Steward Observatory, University of Arizona, 933 North Cherry Avenue, Room N204, Tucson, AZ 85721-0065, USA
[18] Department of Physics, University of California, Davis, CA 95616, USA
[19] Konkoly Observatory, MTA CSFK, Konkoly Thege M. ut 15-17, Budapest, 1121, Hungary
[20] Department of Optics & Quantum Electronics, University of Szeged, Dom ter 9, Szeged, 6720, Hungary
[21] Department of Astronomy, University of Texas at Austin, Austin, TX 78712, USA
[22] Physics Department and Tsinghua Center for Astrophysics (THCA), Tsinghua University, Beijing, 100084, People's Republic of China
[23] Yunnan Observatories (YNAO), Chinese Academy of Sciences, Kunming 650216, People's Republic of China
[24] Key Laboratory for the Structure and Evolution of Celestial Objects, Chinese Academy of Sciences, Kunming 650216, People's Republic of China

Abstract

The nondetection of companion stars in SN Ia progenitor systems lends support to the notion of double-degenerate systems and explosions triggered by the merging of two white dwarfs. This very asymmetric process should lead to a conspicuous polarimetric signature. By contrast, observations consistently find very low continuum polarization as the signatures from the explosion process largely dominate over the pre-explosion configuration within several days. Critical information about the interaction of the ejecta with a companion and any circumstellar matter is encoded in the early polarization spectra. In this study, we obtain spectropolarimetry of SN 2018gv with the ESO Very Large Telescope at -13.6 days relative to the B-band maximum light, or ~ 5 days after the estimated explosion—the earliest spectropolarimetric observations to date of any SN Ia. These early observations still show a low continuum polarization ($\lesssim 0.2\%$) and moderate line polarization ($0.30\% \pm 0.04\%$ for the prominent Si II $\lambda 6355$ feature and $0.85\% \pm 0.04\%$ for the high-velocity Ca component). The high degree of spherical symmetry implied by the low-line and continuum polarization at this early epoch is consistent with explosion models of delayed detonations and is inconsistent with the merger-induced explosion scenario. The dense UV and optical photometry and optical spectroscopy within the first ~ 100 days after the maximum light indicate that SN 2018gv is a normal SN Ia with similar spectrophotometric behavior to SN 2011fe.

Unified Astronomy Thesaurus concepts: Spectro-polarimetry (1973); Galaxies (573); Type Ia supernovae (1728)

Supporting material: machine-readable table

1. Introduction

Thermonuclear supernovae (SNe Ia) have been very well calibrated at low redshift and are used as cosmic distance indicators out to redshift $z \sim 2$ (Riess et al. 1998; Perlmutter et al. 1999; Riess et al. 2016, 2018). However, this calibration is purely empirical and parametric, lacking a detailed physical foundation. The general consensus is that SNe Ia are powered by the ignition of degenerate nuclear fuel from carbon/oxygen white dwarfs (CO WDs; Hoyle & Fowler 1960; see, e.g.,

Howell 2011; Hillebrandt et al. 2013; Maoz et al. 2014; Branch & Wheeler 2017; Hoeflich 2017 for recent reviews). However, it is still unknown how the thermonuclear runaway is triggered and propagates throughout the progenitor star (Arnett 1969; Nomoto et al. 1976; Khokhlov 1991; Niemeyer et al. 1996; Reinecke et al. 2002; Plewa et al. 2004; Röpke 2007; Pakmor et al. 2011, 2012; Seitenzahl et al. 2013). A comprehensive summarize and comparison of these works is provided by Branch & Wheeler (2017). The principal contenders are double-degenerate (DD)

models, in which two WDs merge (Iben & Tutukov 1984; Webbink 1984), and single-degenerate (SD) models, in which a WD accretes matter from a companion (Whelan & Iben 1973) until the critical Chandrasekhar mass of $M_{Ch} \sim 1.4 M_{\odot}$ is reached. There is some evidence that the SN Ia population could consist of both the SD and DD progenitor systems (see, e.g., Maoz et al. 2014). It also remains unclear what the fractions are for various processes contributing to the SN Ia population.

Within this general picture for progenitors, three major classes of explosion have been proposed, which are distinguished by the triggering mechanism of the explosion:

1. Explosion of a single CO WD with a mass close to M_{Ch}. The explosion is triggered by compressional heating near the WD center as a *deflagration* front. Because the compressional heat release increases rapidly toward M_{Ch}, the exploding WD lands in a very narrow mass range (Hoeflich & Khokhlov 1996), though actual triggers may differ as much as slow accretion, pulsational instabilities, or nova eruptions. The donor star may be a moderately evolved Roche-lobe-overflowing star in an SD system (Whelan & Iben 1973) or a tidally disrupted WD in a DD system (Whelan & Iben 1973; Piersanti et al. 2004).

2. Dynamical merging of two CO WDs in a binary system after losing or shedding angular momentum via gravitational radiation (Iben & Tutukov 1984; Webbink 1984; Benz et al. 1990; Nugent et al. 1997; Pakmor et al. 2010). The thermonuclear explosion is triggered by the heat of the merging process or as a consequence of the WD–WD collisions. It is unclear whether the dynamical merging process or a violent collision of two WD leads to an SN Ia, an "accretion induced collapse" (AIC), or a WD with high-magnetic fields (Rasio & Shapiro 1994; Hoeflich & Khokhlov 1996; Segretain et al. 1997; Yoon et al. 2007; Lorén-Aguilar et al. 2009; García-Berro et al. 2012).

3. Another class involves explosions of a sub-M_{Ch} CO WD triggered by detonating a thin surface He layer on the WD, which triggers a detonation front (Woosley et al. 1980; Nomoto 1982a, 1982b; Livne 1990; Woosley & Weaver 1994; Hoeflich & Khokhlov 1996; Kromer et al. 2010).

In the SD channel, the explosions of SNe Ia are triggered by a subsonic ignition of degenerate material. If the pure subsonic deflagration (Reinecke et al. 2002) persists for the entire duration of the explosion, the front would result in a rather homogeneous angular distribution of the ejecta, in terms of both the material velocities and the chemical composition. The deflagration in M_{Ch} WDs, however, is not suitable to describe the class of normal SNe Ia because it fails to explain the rather high kinetic energy of the ejecta, the large amount of ^{56}Ni production (Hillebrandt et al. 2013), together with the presence of unburnt carbon and oxygen. A pure detonation scenario was also ruled out given the fact that the whole star is not burnt to iron and nickel. The delayed-detonation scenario initially requires a subsonic deflagration that, after a period of time, transitions to a supersonic detonation (Khokhlov 1991). The detonation front burns the outer layers to intermediate-mass elements (IMEs)— that is, from Si to Ca. The ejecta are predicted to be stratified in terms of density and chemical abundance, and hence exhibit significant homogeneity on large scales (Gamezo et al. 2005; Seitenzahl et al. 2013; Sim et al. 2013). Another mechanism suggests that the WD could explode at a sub-M_{Ch} (Fink et al. 2010). A CO WD accreting mass from a donor star, depending on the assumed mass-transfer rates and the mass of the CO WD, could be able to accumulate a layer of helium that may develop to a degenerate-helium-shell flash under the right physical conditions (Taam 1980). Such unstable thermonuclear shell ignition could trigger a second detonation in the sub-M_{Ch} WD (Shen et al. 2010).

In the DD channel, the explosion of the SN could be triggered through a dynamic merger of two CO WDs (Pakmor et al. 2010). Starting from two CO WDs with masses of $0.9 M_{\odot}$ and $1.1 M_{\odot}$, the so-called violent merger model is able to reproduce the peak brightness, the color, as well as spectral shape and the velocity profiles of most of the line features, although the predicted rise time of the B-band light curve is long compared to that of normal SNe Ia (Hayden et al. 2010). Other configurations (i.e., with very low mass-transfer rates) could fail to produce an explosive phenomenon and burn the C–O mixture into an O–Ne–Mg WD (Saio & Nomoto 1998) or form a single neutron star (Saio & Nomoto 1985). Thermonuclear explosions might also be triggered by direct, head-on collisions of WDs, and high-resolution numerical simulations are able to reproduce the primary observational signatures of SNe Ia (Kushnir et al. 2013).

One difficulty in distinguishing models reliably by means of conventional photometry or spectroscopy results from the ambiguity of the shape of the SN explosion. The geometry of the explosion and the structure of the SN ejecta, which are too distant to be spatially resolved, can only be probed with polarimetry. The polarized emission from an SN arises from a departure from spherical symmetry (Shapiro & Sutherland 1982). Electron scattering in asymmetric ejecta leads to the incomplete cancellation of electric field vectors (E-vectors), which produce nonzero degrees of observable polarization (Höflich 1991; Hoeflich et al. 1995). The continuum polarization tests whether the photosphere deviates from spherical symmetry, while line polarization traces mostly the distribution of elements in the SN ejecta. Material in the SN ejecta with considerable optical depth may unevenly block the photospheric light beneath, thereby producing a polarization variation and/or polarization position angle rotation in certain spectral features (Kasen et al. 2003; Wang et al. 2006).

Recent studies, in at least one case, have firmly established the progenitor as a compact object consistent with a WD (Nugent et al. 2011; Bloom et al. 2012). The same data also excluded any luminous red giant companion star (Li et al. 2011). The absence of luminous red giants in SN Ia progenitor systems is corroborated by studies of supernova remnants in the Milky Way (González Hernández et al. 2012) and in the LMC (Edwards et al. 2012). These results favor the DD channel for SNe Ia. This process could be sufficiently asymmetric and lead to a clear polarimetric signature (Bulla et al. 2016b). By contrast, observations consistently find a very low continuum polarization (i.e., $\lesssim 0.2\%$, Wang & Wheeler 2008), with a diversity in subluminous events (i.e., SN 1999by, Howell et al. 2001 and SN 2005ke, Patat et al. 2012). Spectropolarimetry has only been available from ~ 7 days past explosion and cannot penetrate the opaque ejecta that have already expanded beyond the innermost interaction zone. Low continuum polarization at these intermediate epochs indicates the photosphere is remarkably spherical (Wang & Wheeler 1996; Wang et al. 2003a; Maund et al. 2013; Hoeflich et al. 2017; Zheng et al. 2017). The approximate spherical symmetry is expected to be maintained in the SD models (Khokhlov 1991).

Recent high-cadence wide-field optical surveys and rapid follow-up observations of SNe, within hours of the explosion, are opening up a new phase in our understanding of SNe. This set of transients, discovered very early, will be extremely valuable for constraining the progenitor systems and explosion physics of SNe. The ejecta quickly sweep away almost all traces of the pre-explosion configuration within a few days. Such information is particularly valuable since it is directly connected to the final mass-loss history of the progenitor system right before the explosion. It is only accessible during the earliest phases. Early polarization measurements, before the pre-explosion configuration is left far behind by the rapidly advancing photosphere, can set constraints on the progenitor systems. Different degrees and types of asymmetry in the SN ejecta are produced by various multi-dimensional explosion models. Large departures in the global symmetry can be expected for dynamical processes (Pakmor et al. 2012; Bulla et al. 2016b). By contrast, M_{Ch} CO WD explosions triggered by a deflagration and sub-M_{Ch} CO WD explosions triggered by detonation of a He layer will mostly appear in the chemical distribution. Mergers can be expected to produce large, time-variant continuum polarization whereas the latter cases may produce abundance asymmetries manifesting themselves in line polarization. Early polarimetry also provides unrivaled clues for differentiating various progenitor scenarios—for example, high continuum polarization is expected for DD mergers (Pakmor et al. 2012, 2013; Moll et al. 2014; Raskin et al. 2014; Bulla et al. 2016b), low continuum but significant line polarization is predicted for delayed-detonation explosions (Khokhlov 1991; Hoeflich et al. 1995; Bulla et al. 2016a), and low-line and continuum polarization should prevail in homogeneously mixed structures of deflagrations (Gamezo et al. 2004).

Polarimetry can also provide diagnostics for other SN Ia hypotheses. Theoretical models by Kasen (2010) show that the ejecta-companion interaction may be detected a few days p0st-explosion. These predictions may be supported by a UV light-curve excess (iPTF14atg, Cao et al. 2015), a clearly resolved blue bump in the light curve of SN 2017cbv (Hosseinzadeh et al. 2017), as well as other SNe Ia that exhibit an early light-curve excess—for example, PTF10ops (Maguire et al. 2011); LSQ12gpw (Firth et al. 2015; Walker et al. 2015); iPTF14bdn (Smitka et al. 2015), SN 2012cg (Marion et al. 2016); MUSSES1604d with an early red flux excess (Jiang et al. 2017); iPTF16abc (Miller et al. 2018); SNe 2011 hr, 2015bq, 2017erp (Jiang et al. 2018), and SN 2018byg (De et al. 2019). See Jiang et al. (2018) for a recent review. Additionally, the 30 minutes cadence monitoring of the Kepler spacecraft also shows a prominent initial flux excess in the early light curve of SN 2018oh (Dimitriadis et al. 2019; Li et al. 2019; Shappee et al. 2019). Moreover, no signature of the SN ejecta-companions interaction has been found in the Kepler light curves of three other SNe (Olling et al. 2015). High-cadence monitoring by the Transiting Exoplanet Survey Satellite (Ricker et al. 2015) will provide a comprehensive characterization of the early-time light curves of more bright SNe (e.g., Fausnaugh et al. 2019).

The early blue excess could, however, also be explained by vigorous mixing of radioactive ^{56}Ni in the SN ejecta (Hosseinzadeh et al. 2017; Miller et al. 2018). If such an early blue bump was caused by ejecta-companion interaction, the brightest bump would be observed from looking straight down the companion, from which the view is symmetric so that there is no net polarization.

Large polarimetric signatures would come from an off-axis viewing angle in which the bump is fainter or invisible. Early polarimetry and its correlation with the light-curve morphology would provide an important diagnostic of the ejecta-companion interaction case.

We present extensive UV-optical photometry, optical spectroscopy, and optical spectropolarimetry of the nearby Type Ia SN 2018gv in the host galaxy NGC 2525. The organization of this paper is as follows. Observations and data reductions are detailed in Section 2. Section 3 describes the photometric evolution and estimates derived for the extinction arising in the host galaxy. Section 4 presents the spectral evolution, and Section 5 investigates the spectropolarimetric properties of the SN. Discussions and a brief summary of the study are given in Sections 6 and 7, respectively.

2. Observations and Data Reduction

SN 2018gv was discovered at UT 2018 January 15 16:21:06 with an 0.5 m/f6.8 telescope at an unfiltered magnitude of 16.5 mag (Itagaki 2018). Follow-up spectroscopy on UT 2018 January 16 12:41:15 (Siebert et al. 2018) reveals that SN 2018gv was a very young, normal SN Ia, at ∼11–13 days before the maximum luminosity according to the classification with SNID (Blondin & Tonry 2007). We measure its J2000.0 coordinates on the images obtained by the Sinistro cameras on Las Cumbres Observatory (LCO) Global Network of 1 m telescopes to be $\alpha = 08^h05^m34\overset{s}{.}58$, $\delta = -11°26'16\overset{''}{.}77$. SN 2018gv exploded $3\overset{''}{.}46$ W and $39\overset{''}{.}15$ S of the nucleus of the host spiral galaxy NGC 2525 (see Figure 1). We queried the SIMBAD[25] database to retrieve reported heliocentric radial velocity measurements of the host galaxy. Among six reported measurements, we adopt a median value of 1582 km s^{-1} with a standard deviation of 12.6 km s^{-1}, which falls into the value obtained by the 2MASS catalog (Tully 2015). This implies a redshift of $z = 0.00527 \pm 0.00004$ for SN 2018gv, which is used throughout the paper together with the adopted Hubble constant of $H_0 = 73.24 \pm 1.74$ km s^{-1} Mpc^{-1} (Riess et al. 2016).

2.1. Optical Photometry

2.1.1. Ground-based Photometry

Extensive $UBg'Vr'i'$ photometry was obtained with the Sinistro cameras on the LCO network of 1 m telescopes. The images were pre-processed, including bias subtraction and flat-field correction using the BANZAI automatic pipeline (McCully et al. 2018). Figure 1 shows the field around SN 2018gv. Because the SN is bright and in the outskirts of the galaxy, template subtraction and PSF-fitting are not necessary. Therefore, the flux of the SN and the local reference stars were measured with a circular aperture of $3\overset{''}{.}0$ in radius. The background was estimated by the median pixel value of an annulus around the SN with an inner radius of $9\overset{''}{.}0$ and an outer radius of $12\overset{''}{.}0$. We calibrated the instrumental BV and $g'r'i'$ magnitudes of SN 2018gv to the standard Johnson BV system (Johnson 1966) in Vega magnitude and the SDSS photometric system (Fukugita et al. 1996) in AB magnitude, respectively, based on the magnitude of local comparison stars from the AAVSO Photometric All-sky Survey (APASS) DR9 Catalogue (Henden et al. 2016, see Table 1). U-band magnitudes are only available for five of the comparison stars from the All-sky

---
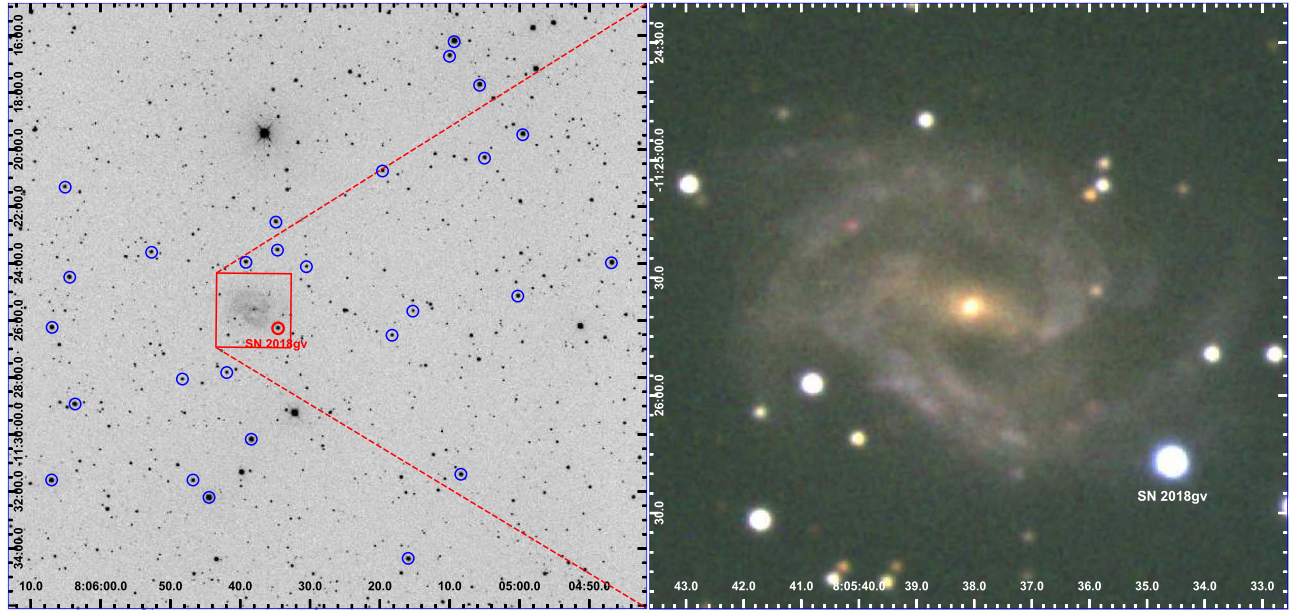
Figure 1. Left panel: LCO *V*-band image showing the location of SN 2018gv. Reference stars are marked with blue circles. The red square outlines the right panel. Right panel: color image of SN 2018gv in NGC 2525 from LCO *B*, *V*, and *r'*-band exposures. North is up; east is left.

Table 1
Photometric Standards in the SN 2018gv Field

ID	α (J2000)	δ (J2000)	U (mag)	B (mag)	V (mag)	g (mag)	r (mag)	i (mag)
1	8:05:39.190	−11:23:57.77		13.199(028)	12.707(015)	12.897(027)	12.590(044)	12.533(044)
2	8:05:34.667	−11:23:32.26		14.029(027)	12.973(023)	13.439(040)	12.640(047)	12.402(029)
3	8:05:38.418	−11:30:10.37	11.80	11.856(035)	11.494(010)	11.612(041)	11.417(038)	11.432(028)
4	8:05:34.874	−11:22:33.51		13.008(033)	12.655(022)	12.754(023)	12.598(043)	12.638(035)
5	8:05:44.471	−11:32:12.54	11.07	10.888(022)	10.714(017)	10.729(030)	10.772(074)	10.870(039)
6	8:06:03.681	−11:28:56.15		13.276(041)	11.996(022)	12.597(047)	11.549(041)	11.166(025)
7	8:05:15.921	−11:34:21.17		13.545(050)	11.890(051)	12.631(063)	11.243(090)	10.072(000)
8	8:05:08.379	−11:31:24.17		12.948(021)	12.450(020)	12.644(024)	12.308(048)	12.239(027)
9	8:06:06.937	−11:26:14.69		13.309(036)	11.904(026)	12.577(048)	11.366(045)	10.914(038)
10	8:06:07.016	−11:31:35.82		12.222(020)	11.694(026)	11.904(033)	11.551(051)	11.443(041)
11	8:06:04.411	−11:24:29.13		13.381(032)	12.293(019)	12.786(045)	11.944(044)	11.680(026)
12	8:04:46.849	−11:23:58.66		13.279(015)	11.684(033)	12.448(044)	11.076(045)	10.496(090)
13	8:04:59.549	−11:19:29.13	13.73	12.901(009)	11.726(017)	12.247(043)	11.312(037)	10.968(022)
14	8:05:09.374	−11:16:13.25	10.51	10.836(020)	10.839(024)	10.740(036)	10.959(055)	11.205(029)
15	8:05:52.649	−11:23:37.18		13.838(022)	13.274(029)	13.501(032)	13.112(041)	13.038(027)
16	8:05:41.910	−11:27:49.40		14.812(026)	13.737(033)	14.240(067)	13.356(043)	13.071(015)
17	8:05:30.515	−11:24:07.41		14.503(041)	13.956(018)	14.183(034)	13.792(048)	13.717(025)
18	8:05:48.271	−11:28:03.66		14.380(025)	13.840(016)	14.068(032)	13.699(044)	13.603(044)
19	8:06:05.047	−11:21:19.65		13.645(022)	13.253(030)	13.378(013)	13.200(029)	13.153(042)
20	8:05:15.276	−11:25:40.51		14.811(022)	13.774(036)	14.219(022)	13.460(033)	13.141(028)
21	8:05:19.620	−11:20:45.77		13.686(022)	13.208(016)	13.382(034)	13.089(053)	13.019(012)
22	8:05:05.024	−11:20:18.45		13.324(020)	12.814(011)	13.009(029)	12.678(056)	12.584(022)
23	8:05:00.250	−11:25:08.76		13.549(011)	12.696(031)	13.056(030)	12.391(039)	12.180(034)
24	8:05:10.005	−11:16:43.26		14.011(023)	12.622(035)	13.342(030)	12.007(047)	11.407(013)
25	8:05:46.770	−11:31:36.23		13.927(031)	12.901(030)	13.367(044)	12.530(046)	12.228(023)
26	8:05:18.257	−11:26:31.45		15.140(049)	14.023(020)	14.521(035)	13.636(041)	13.288(021)
27	8:05:05.733	−11:17:44.99	13.74	12.718(022)	11.826(013)	12.219(032)	11.544(050)	11.298(022)

spectrally matched Tycho2 stars catalog (Pickles & Depagne 2010). The final *Bg'Vr'i'* and *U*-band calibrations were carried out based on the median of the difference between catalog magnitude and the instrumental magnitude of the 27 comparison stars and 5 comparison stars, respectively. The field containing the comparison stars is also shown in the left panel of Figure 1.

2.1.2. SWIFT UVOT Photometry

Ultraviolet and optical photometry was obtained using the Ultra-violet/Optical Telescope (UVOT; Roming et al. 2005) on the Neil Gehrels Swift Observatory (Gehrels et al. 2004). Photometry was reduced using the pipeline of the Swift Optical Ultraviolet Supernova Archive (SOUSA; Brown et al. 2014) using the zero-points of Breeveld et al. (2011).

Table 2
Log of Spectroscopic Observations of SN 2018gv

UT Date (2018)	MJD	Phase[a] (days)	Range (Å)	Exposure (s)	Instrument/Telescope
Jan 16 12:08	58134.50	−15.18	3200−9900	2700	FLOYDS/LCO 2.0 m FTN
Jan 17 08:13	58135.34	−14.34	3200−9900	2700	FLOYDS/LCO 2.0 m FTN
Jan 17 11:53	58135.50	−14.19	3500−9900	300	GMOS-N/Gemini-N 8.1 m
Jan 18 02:20	58136.10	−13.59	4400−9200	4 × 900	FORS2/VLT 8.2 m
Jan 18 11:05	58136.46	−13.23	3200−9900	2700	FLOYDS/LCO 2.0 m FTN
Jan 19 06:55	58137.29	−12.40	3600−10200	767	LRS2/HET 10 m
Jan 20 10:04	58138.42	−11.27	3200−9900	2700	FLOYDS/LCO 2.0 m FTN
Jan 23 09:42	58141.41	−8.28	3200−9900	1800	FLOYDS/LCO 2.0 m FTN
Jan 25 07:57	58143.33	−6.36	3200−9900	1800	FLOYDS/LCO 2.0 m FTN
Jan 25 20:35	58143.75	−5.94	3500−8900	2401	RSS/SALT 11 m
Jan 28 06:33	58146.27	−3.41	3600−10200	507	LRS2/HET 10 m
Jan 29 08:50	58147.37	−2.32	3200−9900	1800	FLOYDS/LCO 2.0 m FTN
Jan 31 05:08	58149.21	−0.47	4400−9200	4 × 120	FORS2/VLT 8.2 m
Feb 4 10:13	58153.43	3.74	3200−9900	1800	FLOYDS/LCO 2.0 m FTS
Feb 8 10:45	58157.45	7.76	3200−9900	1800	FLOYDS/LCO 2.0 m FTS
Feb 13 06:38	58162.28	12.59	3200−9900	1800	FLOYDS/LCO 2.0 m FTN
Mar 1 12:06	58178.50	28.82	4800−9300	1800	FLOYDS/LCO 2.0 m FTS
Mar 9 13:45	58186.57	36.89	3300−9900	1800	FLOYDS/LCO 2.0 m FTS
Mar 17 11:28	58194.48	44.79	3400−9900	1800	FLOYDS/LCO 2.0 m FTS
Mar 22 03:49	58199.66	49.97	3800−9200	900	DIS/ARC 3.5 m
Mar 23 11:28	58200.48	50.79	3300−9900	1800	FLOYDS/LCO 2.0 m FTS
Mar 29 10:26	58206.43	56.75	4800−9300	1800	FLOYDS/LCO 2.0 m FTS
Apr 5 10:43	58213.45	63.76	3200−9900	1800	FLOYDS/LCO 2.0 m FTS
Apr 11 11:36	58219.48	69.80	3600−9300	2700	FLOYDS/LCO 2.0 m FTS
Apr 17 11:04	58225.46	75.77	3700−9200	2700	FLOYDS/LCO 2.0 m FTS
Apr 25 06:52	58233.29	83.60	3200−9900	2700	FLOYDS/LCO 2.0 m FTN

Note.
[a] Relative to the B-band maximum light, MJD_{Bmax} = 58,149.698 ± 0.510/2018 January 31 16:45.

2.2. Optical/Near-infrared (NIR) Spectroscopy

A journal of spectroscopic observations of SN 2018gv is provided in Table 2. The spectral sequence of SN 2018gv spans $t = -15.2$ to $+83.6$ days. All phases are given relative to the B-band maximum at MJD 58,149.698 or UT 2018-01-31.698 (see Section 3) throughout the paper.

2.2.1. LCO Optical Spectroscopy

LCO optical spectra were taken with the FLOYDS spectrographs mounted on the 2 m Faulkes Telescope North and South at Haleakala, USA, and Siding Spring, Australia, respectively, through the Global Supernova Project. A 2″ slit was placed on the target at the parallactic angle. One-dimensional spectra were extracted, reduced, and calibrated following standard procedures using the FLOYDS pipeline[26] (Valenti et al. 2014).

2.2.2. Gemini Optical Spectroscopy

We obtained an optical spectrum of SN 2018gv using the Gemini Multi-object Spectrographs (GMOS; Davies et al. 1997) on Gemini North telescope on 2018 January 17 UT with an air mass of 1.22 (GN-2017B-Q-12; PI Howell). For this spectrum, we obtained 2 × 300 s exposures in both the B600 and R400 gratings, with central wavelengths of 450 nm and 750 nm, respectively. We covered the chip gap by moving the central wavelength for the second exposure by 5 nm and 7.5 nm for the blue and red setups, respectively.

The Gemini data were reduced using the standard techniques using a combination of the Gemini-IRAF[27] and custom procedures written in Python. We obtained observations of the Hubble Space Telescope (HST) spectrophotometric standard star, HZ44, as part of the same program. The sensitivity function was derived using the HST spectrophotometric data. The telluric correction was then derived from the standard star observation.

2.2.3. Hobby–Eberly Telescope (HET) Spectroscopy

Additional spectra covering the optical regime between 3700 and 10500 Å were taken with the Low-resolution Spectrograph 2 (LRS2; Chonis et al. 2016) on the 10 m Hobby–Eberly Telescope (Ramsey et al. 1998). LRS2 is composed of two dual-arm spectrographs, LRS2-B and LRS2-R, each having two spectral regions with a ∼100 Å overlap. The LRS2-B UV-arm extends from 3700 Å to 4700 Å, while the orange arm covers the 4600–7000 Å interval, with a resolving power of 1900 and 1100, respectively. The red arm of LRS2-R records spectra from 6500 to 8420 Å, while the range 8180 to 10500 Å is covered by the far red arm, both having $R \sim 1800$ spectral resolving power. Both arms are fed by their own 12″ × 6″ integral field unit (IFU), which contains 280 densely packed fibers with lenslet coupling. The diameter of a single fiber/lenslet is ∼0″.6 on sky. The fill factor of both IFUs is ∼98%, which provides very good spatial sampling on the sky without the

---

[26] https://github.com/svalenti/FLOYDS_pipeline

[27] https://www.gemini.edu/node/11823

need for dithering (see Chonis et al. 2016 for additional details).

The reduction of the LRS2 IFU data was done with self-developed IRAF[28] and Python scripts. Fiber-to-fiber transmission variations were corrected by observing at least one frame of blank sky during twilight and requiring a homogeneous, flat, output signal on the reconstructed image within the field of view. Wavelength calibration was performed by a combination of Hg and Cd spectral lamp exposures for LRS2-B and an FeAr spectral lamp for LRS2-R. For sky subtraction, the mean sky spectrum was constructed by 3σ-clipping the fibers having signal exceeding the median of all fibers, then computing the median combination of all remaining fibers. Flux calibration was completed based on nightly observations of spectrophotometric standard stars taken at approximately similar air masses to the SN. Telluric lines were removed from the final spectra by using a mean telluric spectrum (constructed from multiple observations of telluric standard stars) scaled to the flux level of the actual SN spectrum.

2.2.4. SALT Optical Spectroscopy

We observed SN 2018gv with the Southern African Large Telescope (SALT) using the Robert Stobie Spectrograph (RSS; Smith et al. 2006) on 2018 January 25.8 UT under Rutgers University program 2017-1-MLT-002 (PI: SWJ). We used the PG0900 grating and 1″5 wide longslit with a typical spectral resolution $R = \lambda/\Delta\lambda \approx 1000$. Exposures were taken in four grating tilt positions to cover the optical spectrum from 350 to 930 nm. The data were reduced using a custom pipeline based on standard PyRAF (Science Software Branch at STScI 2012) spectral reduction routines and the PySALT package (Crawford et al. 2010).

2.2.5. ARC Optical Spectroscopy

On 2018 March 22 UT, we obtained one low-resolution spectrum with the Dual Imaging Spectrograph (DIS),[29] mounted on the 3.5 m Astrophysics Research Consortium (ARC) telescope at the Apache Point Observatory. The B400 and R300 gratings were used with central wavelengths of 4500 and 7500 Å, respectively. The instrument was rotated to the parallactic angle, and 3×300 s exposures were obtained. The data were reduced using standard procedures and calibrated to a standard star obtained the same night using the PyDIS package (Davenport 2018).

The $UBg'Vr'i'$ light curves and FLOYDS/LCO spectra were obtained as part of the Global Supernova Project. All photometry and spectroscopy will become available via WISeREP[30] (Yaron & Gal-Yam 2012).

2.3. VLT Spectropolarimetry

Spectropolarimetry of SN 2018gv was conducted using the Focal Reducer and Low Dispersion Spectrograph (FORS2) on UT1 (Antu) of the ESO Very Large Telescope (VLT). Observations were carried out in the FORS2 Polarimetry with Multi-Object Spectroscopy (PMOS) mode (Appenzeller et al. 1998) on 2018 January 18 (epoch 1) and 2018 January 31

(epoch 2), corresponding to $t = -13.6$ days and $t = -0.5$ day, respectively. Details of the VLT spectropolarimetry are available in Appendix A. The intensity-normalized Stokes parameters (I, Q, U) are binned in ~25 Å wide bins (~7.5 pixels) to further increase the signal-to-noise ratio (S/N). The observed degree of linear polarization ($p_{\rm obs}$) and its position angle (PA$_{\rm obs}$) are given by

$$p_{\rm obs} = \sqrt{Q^2 + U^2},$$
$$\mathrm{PA}_{\rm obs} = \frac{1}{2}\arctan\left(\frac{U}{Q}\right). \tag{1}$$

The calculated $p_{\rm obs}$ is by definition a positive number and is therefore biased toward larger values than the true degree of polarization p. We correct the polarization bias following the equation given in Wang et al. (1997),

$$p = (p_{\rm obs} - \sigma_p^2/p_{\rm obs}) \times h(p_{\rm obs} - \sigma_p),$$
$$\text{and } \mathrm{PA} = \mathrm{PA}_{\rm obs}, \tag{2}$$

where σ_p gives the 1σ uncertainty in $p_{\rm obs}$, h is the Heaviside step function. Calculation and bias correction of the polarization, as well as the estimation of associated uncertainties, were performed by our own specially written software, following the prescriptions described by Patat & Romaniello (2006) and the scheme presented by Maund et al. (2007).

3. Light Curves of SN 2018gv

In Figure 2, we show the LCO $UBg'Vr'i'$-band and the SWIFT UVOT $uvw2$, $uvm2$, $uvw1$, u, b, and v photometry without the extinction corrections. The magnitudes are in the same system as the calibration catalogs for consistency (i.e., the $g'r'i'$-band in the AB system), while other bands are in the Vega system. The $UBg'Vr'i'$-band light curves were sampled during the period $t \approx -15$ to $+137$ days relative to the B-band maximum. We conduct high-order polynomial fits to the light curves before day $+110$ and plot the fits between the first observation and day $+90$. Short lines on the top axis indicate the epochs of spectroscopy and spectropolarimetry.

We list the calibrated LCO $UBg'Vr'i'$ photometry in Table 3. The UBV and the $g'r'i'$-band photometry are presented in Vega and AB systems, respectively. All tabulated photometry was not corrected for the extinctions from the host and the Milky Way. Photometric parameters, including the times of the light-curve peaks, maximum brightness, the decline in the magnitude from the maximum light to the magnitude 15 days after (i.e., $\Delta m(15)$, which characterizes the width of the light curve), are reported in Table 4. K-corrections were applied to our photometry when calculating $\Delta m(15)$. The presented values of the peak brightness have been corrected for the extinction from the Milky Way but not the host galaxy because we estimate little or no extinction from the host galaxy toward SN 2018gv. A detailed analysis of the extinction will be provided in the following subsection.

3.1. Extinction

The Galactic reddening toward the SN 2018gv line of sight has been estimated as $E(B - V)_{\rm 18gv}^{\rm MW} = 0.051$ mag using the NASA/IPAC NED Galactic Extinction Calculator, adopting the $R_V = 3.1$ extinction law (Cardelli et al. 1989) and the extinction map given by Schlafly & Finkbeiner (2011). We consider the host-galaxy reddening to be low for the following

---

[28] IRAF is distributed by the National Optical Astronomy Observatories, which are operated by the Association of Universities for Research in Astronomy, Inc., under cooperative agreement with the National Science Foundation.
[29] https://www.apo.nmsu.edu/arc35m/Instruments/DIS/
[30] https://wiserep2.weizmann.ac.il/
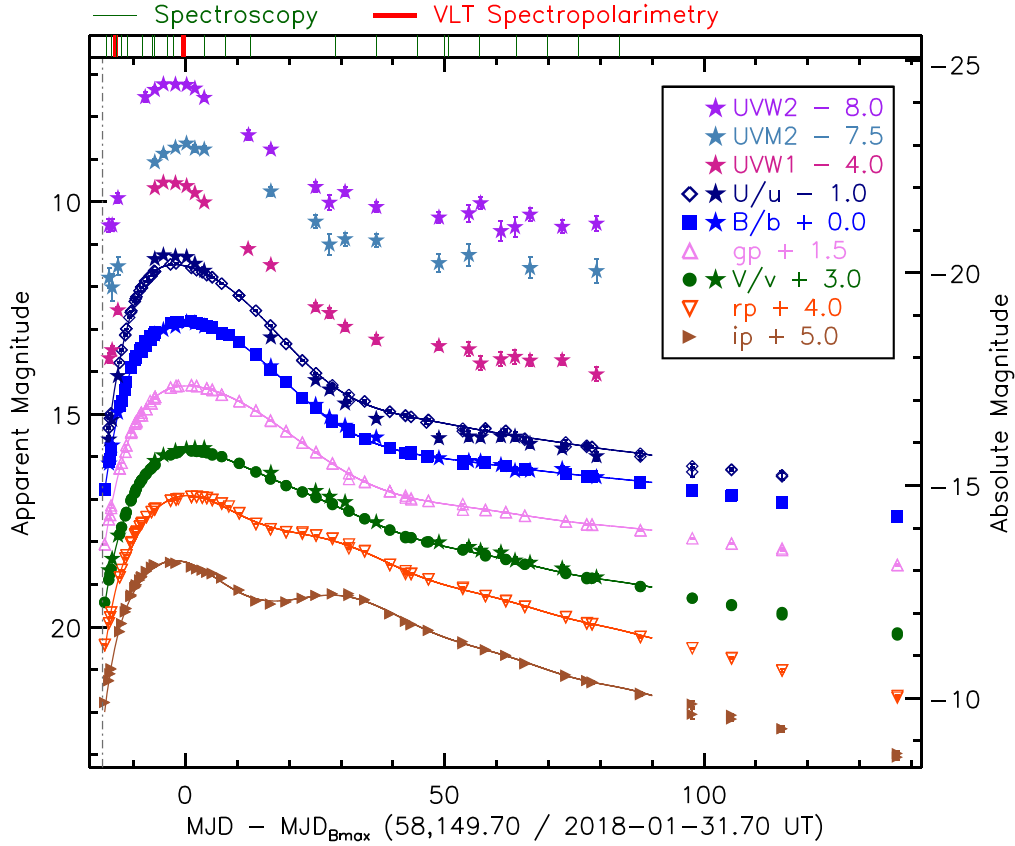
Figure 2. Optical light curves of SN 2018gv. The vertical dotted–dashed line shows the time of discovery. Short vertical lines at the top of the panel mark the spectroscopic and spectropolarimetric observations. Solid curves present polynomial fits to the LCO photometry.

Table 3
LCO $UBg'Vr'i'$ Photometry of SN 2018gv

MJD[a]	U (mag)	MJD[a]	B (mag)	MJD[a]	V (mag)	MJD[a]	g' (mag)	MJD[a]	r' (mag)	MJD[a]	i' (mag)
…	…	134.078	16.763(008)	134.086	16.426(008)	134.090	16.562(006)	134.094	16.417(008)	134.098	16.777(014)
…	…	134.082	16.772(008)	134.086	16.415(008)	134.094	16.552(006)	134.098	16.425(008)	134.102	16.769(014)
134.863	16.330(013)	134.871	16.123(005)	134.879	15.896(006)	134.883	15.969(004)	134.887	15.914(006)	134.891	16.254(011)
134.867	16.312(014)	134.875	15.111(005)	134.879	15.888(006)	134.887	15.964(004)	134.891	15.911(006)	134.895	16.269(012)
…	…	….	…	…	…	…	…	…	…	…	…
150.820	12.557(002)	150.828	12.813(002)	150.828	12.861(003)	150.832	12.818(002)	150.836	12.941(003)	150.836	13.593(006)
150.824	12.556(002)	150.828	12.817(002)	150.832	12.862(003)	150.832	12.817(002)	150.836	12.941(003)	150.836	13.582(006)
…	…	….	…	…	…	…	…	…	…	…	…
254.980	17.218(044)	254.984	16.920(013)	254.988	16.472(013)	254.992	16.542(009)	254.996	16.743(016)	254.996	17.164(034)
254.980	17.354(112)	254.988	16.899(013)	254.988	16.497(013)	254.992	16.536(008)	254.996	16.727(016)	254.996	17.072(031)
264.723	17.427(084)	264.727	17.061(030)	264.730	16.717(029)	264.734	16.653(017)	264.738	17.021(033)	264.738	17.393(064)
264.727	17.461(088)	264.730	17.094(031)	264.734	16.657(028)	264.734	16.691(018)	264.738	17.020(032)	264.742	17.390(065)
…	…	286.961	17.404(026)	286.965	17.136(023)	286.965	17.038(013)	286.969	17.620(031)	286.973	18.056(070)
…	…	286.961	17.400(026)	286.965	17.189(024)	286.969	17.047(013)	286.969	17.660(032)	286.973	17.972(064)

Note.
[a] MJD 58,000, MJD of the B-band maximum light.

(This table is available in its entirety in machine-readable form.)

reasons: (1) the SN's position in the outskirts of the host galaxy NGC 2525; (2) the evolution of the $B − V$ color of the SN, which is consistent with the Lira–Phillips relation at 30–90 days after the B-band maximum light (Phillips et al. 1999). Although an empirical relation between the amount of dust extinction and the strength of the absorption doublet of Na ID 5890 and 5896 Å has been proposed by Munari & Zwitter (1997) and widely used, the validity of the application of the

methodology has been questioned for use with low-resolution spectra (Poznanski et al. 2011). All spectroscopic observations discussed in this study were carried out in a low-resolution regime, and thus we have not considered extinction estimation based on Na ID absorption features.

A linear relationship between the B-band magnitude and the $B − V$ color evolution of SNe Ia within a few days to approximately a month relative to the B-band peak brightness

Table 4
Photometric Parameters of SN 2018gv

Band	λ_{pivot} (Å)	A_λ^{MW} (mag)	$A_\lambda^{\mathrm{Host}}$ (mag[b])	$t_{\max}$ [a] (days)	Δm_{15} (mag[c])	m_{peak} (mag[c])	M_{peak} (mag[c])
U	3600	0.251	0.131 ± 0.125	47.518(430)	1.027(050)	12.230(046)	$-19.442(048)$
B	4365	0.210	0.109 ± 0.110	49.698(510)	0.963(054)	12.609(051)	$-19.063(053)$
V	5362	0.159	0.087 ± 0.086	50.598(520)	0.626(028)	12.696(025)	$-18.976(027)$
g'	4736	0.191	0.102 ± 0.097	49.928(545)	0.726(043)	12.641(044)	$-19.031(045)$
r'	6232	0.132	0.068 ± 0.068	50.078(450)	0.703(018)	12.778(043)	$-18.894(044)$
i'	7529	0.098	0.053 ± 0.052	47.688(405)	0.878(016)	13.342(055)	$-18.330(066)$

Notes.
[a] Uncertainties of maximum-light dates in unit of 0.01 day. The date is MJD 58100.
[b] Uncertainties were not added when deducing the photometric parameters.
[c] Uncertainties are indicated by the number in parentheses and in unit of 0.01 magnitude.

has been found by Wang et al. (2003b). This color–magnitude (CMAG) relation provides a robust way (denoted as the "CMAGIC" method hereafter) to deduce the SN distance as well as the dust extinction from the host galaxy when the magnitude at the SN maximum light was also measured. Applying the "CMAGIC" method, we deduce the color excess of SN 2018gv as $E_{BV}^{18\mathrm{gv}} = 0.028 \pm 0.027$ mag (see Appendix B). A sanity test of the method based on the photometry of SN 2011fe (Munari et al. 2013) is also provided therein. Note that the color–magnitude relation has also been applied to the entire set of sample I of the Carnegie-Supernovae Program (CSP I; Krisciunas et al. 2017). For normal-bright SNe Ia like SN 2018gv, the color–magnitude diagram is stable but there is a systematic shift for transitional and subluminous SNe Ia, as predicted by models (Hoeflich et al. 2017).

We also compare the $B - V$ color of SN 2018gv at 30–90 days after the B-band maximum light to the color evolution described by the Lira–Phillips relation (Phillips et al. 1999; Folatelli et al. 2010; see Equations 3(a) and (b), respectively):

$$(B - V)_0 = 0.725 - 0.0118(t_V - 60), \qquad (3a)$$

$$(B - V)_0 = 0.732(0.006) - 0.0095(0.0005)(t_V - 55). \qquad (3b)$$

The mean difference between the $B - V$ color and the Lira law given by Equation 3(a) is $E(B - V) = 0.036 \pm 0.018$ mag, which has a dispersion of 0.06 mag (see the lower-left panel of Figure 4). This is in good agreement with the estimation based on the CMAGIC method. The mean difference between the SN 2018gv observations and the Lira law fitted by Folatelli et al. (2010) gives $E(B - V) = 0.092 \pm 0.036$ mag. Considering a dispersion of 0.077 mag in the Lira law suggested by Equation 3(b), we conclude that the extinction estimated by the CMAGIC method agrees with that interpreted from the Lira law.

The final estimated values of the Galactic and the host-galaxy extinction in different bandpasses are listed in Table 4. Here we have assumed that the dust in the host of SN 2018gv has similar properties as Galactic dust with $R_V = 3.1$. In this study, we only apply the extinction corrections for both the Galactic and the host component to SN 2018gv photometry when estimating the UV-optical pseudo-bolometric luminosities. This will be discussed in Section 4.2. Figure 3 illustrates the CMAGIC method applied to the B-band with $B - V$ color of SN 2018gv after correcting for the Galactic extinction. Similar diagrams derived from the well-sampled light curves of SN 2011fe are presented.

3.2. Color Curves

Figure 4 shows the color evolution of SN 2018gv ($uvw2 - uvw1$, $uvw1 - u$, $U - B$, $g' - r'$, $B - V$, and $r' - i'$), corrected for the Galactic and host reddening derived in Section 3.1. The color curves of SN 2018gv are overplotted with those of the Type Ia SNe 2011fe (Munari et al. 2013; Zhang et al. 2016), 2012fr (Contreras et al. 2018), and 2017cbv (Hosseinzadeh et al. 2017), corrected for reddening in both the Milky Way and the host galaxies.

The $uvw2 - uvw1$ and $uvw1 - u$ colors of SN 2018gv appear to have similar trends to those of the selected SNe, except that SN 2018gv has bluer colors than the comparison SNe before $t \approx -10$ days (i.e., by ~ 0.3 index). The early $U - B$ color of SN 2018gv shows a rapid decline and reached a minimum of ~ -0.5 mag at $t \approx -7$ days and then became redder in a linear fashion in magnitude space until $t \sim 25$ days. The color curve hereafter entered a plateau phase and slowly turns red over time. SN 2012fr exhibited a similar behavior, whereas SN 2017cbv and SN 2011fe became redder until $t \approx -14$ days, and then started to become bluer and reached the turning point at $t \approx -7$ days. The $B - V$ and the $g' - r'$ colors of the selected SNe show a similar evolution, except for SN 2017cbv, which displayed constant colors from the earliest epoch to $t \approx +7$ days. The $r' - i'$ color curves of SN 2018gv and other selected SNe have very similar shapes, but the rising phases to the secondary maximum display offsets of up to 10 days.

3.3. Estimating Light-curve Parameters with SNooPy

The peculiar velocity with respect to the Hubble flow might be relatively large due to the approximity of SN 2018gv. Therefore, we also estimated the luminosity distance to the SN using tools from the SuperNovae in object-oriented Python (SNooPy)[31] package (Burns et al. 2011). Based on the B- and V-band photometry after correcting for the galactic reddening and using the (Burns et al. 2011) calibration of the Phillips relation, we derived the distance modulus of SN 2018gv $\mu_0^{\mathrm{SNPY}} = 31.835 \pm 0.011 \pm 0.086$. This yields a distance of $D^{\mathrm{SNPY}} = 23.28 \pm 0.12 \pm 0.94$ Mpc, which is larger compared to the inferred distance assuming SN 2018gv is in the Hubble flow, $D = 21.60 \pm 0.19 \pm 0.51$ Mpc. For each parameter derived by SNooPy, the first and the second uncertainties represent the statistical error and the systematic error, respectively. Additionally, the SNooPY host reddening of SN 2018gv gives

---

[31] Analysis for this paper was done with SNooPy version 2.5.2, available at https://csp.obs.carnegiescience.edu/data/snpy.
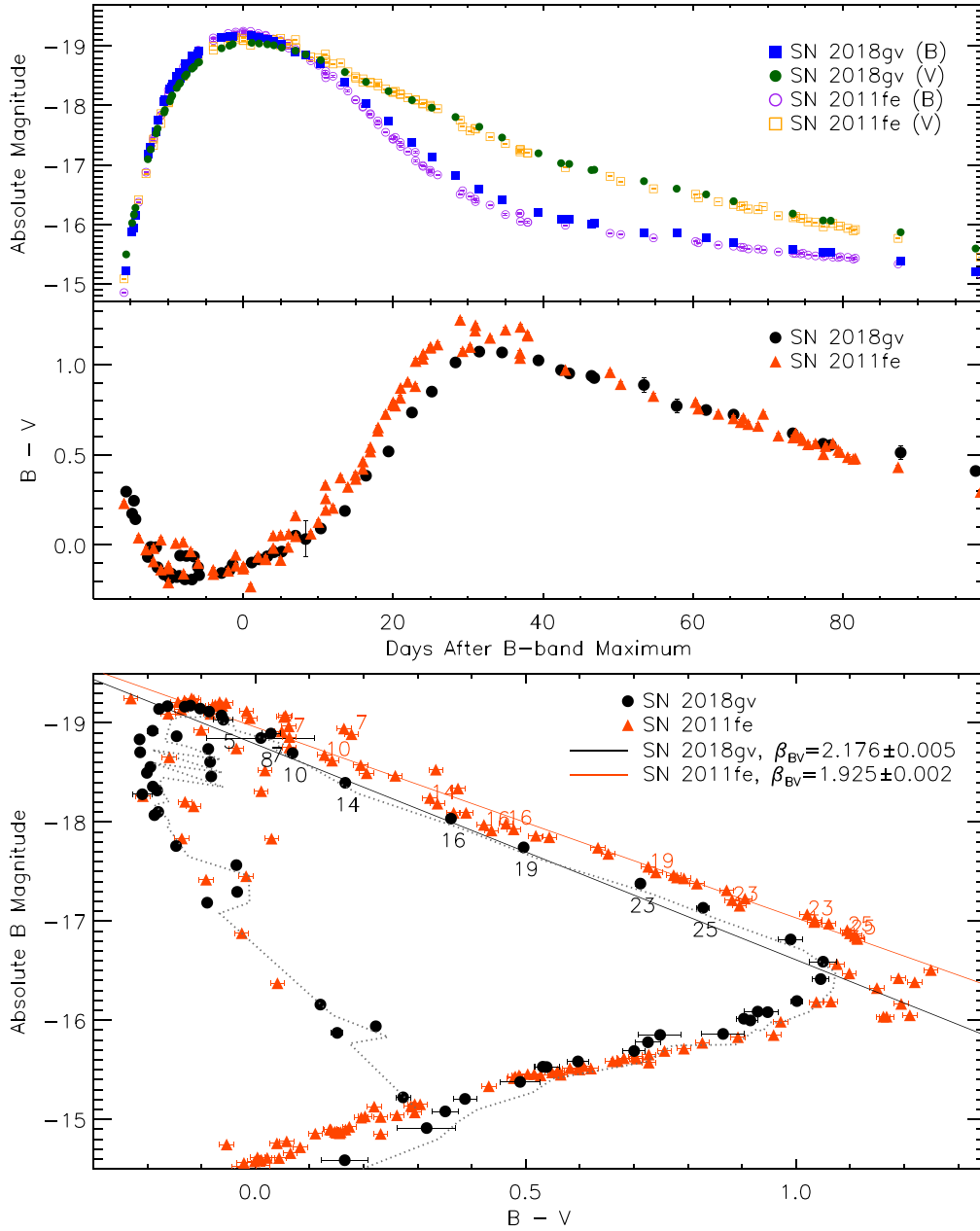
Figure 3. The upper panel presents the B- and V-band light curves of SN 2018gv and SN 2011fe. The middle panel shows the color versus rest-frame day plot. The dotted black line shows the $B - V$ color without the extinction correction of the host galaxy. In the bottom panel, the black circles and the orange triangles show the color–magnitude diagrams of SN 2018gv and SN 2011fe, respectively. The dotted black line is shown for comparison, which represents the color–magnitude plot of SN 2018gv before correcting for the host extinction. The epochs within the linear regions are labeled by corresponding rest-frame days. The black and orange solid lines are the linear fit to the linear regions of SN 2018gv and SN 2011fe, respectively.

$E(B - V)^{\mathrm{SNPY}}_{18\mathrm{gv}} = -0.148 \pm 0.004 \pm 0.060$, which is broadly consistent with the negligible reddening estimated by the CMAGIC method. The B-band light-curve decline in the first 15 days after peak gives $\Delta m_{15}^{\mathrm{SNPY}}(B) = 0.983 \pm 0.009 \pm 0.060$, consistent with the value deduced from the high-order polynomial light-curve fitting (e.g., see Table 4).

The negative value of $E(B - V)^{\mathrm{SNPY}}_{18\mathrm{gv}}$ derived for the host galaxy of SN 2018gv is unphysical. The reason is because SN 2018gv has intrinsically bluer colors compared to the subsample of unreddened SNe Ia in the SNooPY template from Folatelli et al. (2010). Therefore, the fitted luminosity distance suffers from a systematic uncertainty in the intrinsic color that is correlated with the width of the light curve. The very nearby host

galaxy of SN 2018gv may also have considerable peculiar velocity so it may deviate from moving with the Hubble flow. We found a relative difference of ~7% between the luminosity distance of the SN and the distance inferred based on the redshift of the host. We do not attempt to decide which method gives a more precise distance estimation, and we present the result of the bolometric light-curve calculations based on a distance derived form the redshift of the host in Section 4.2. We also mention the key results for adopting a SNooPy-fitted luminosity distance.

3.4. Early Light Curves

If SN 2018gv exploded as an ideal, expanding fireball with constant temperature and velocity, its luminosity should scale
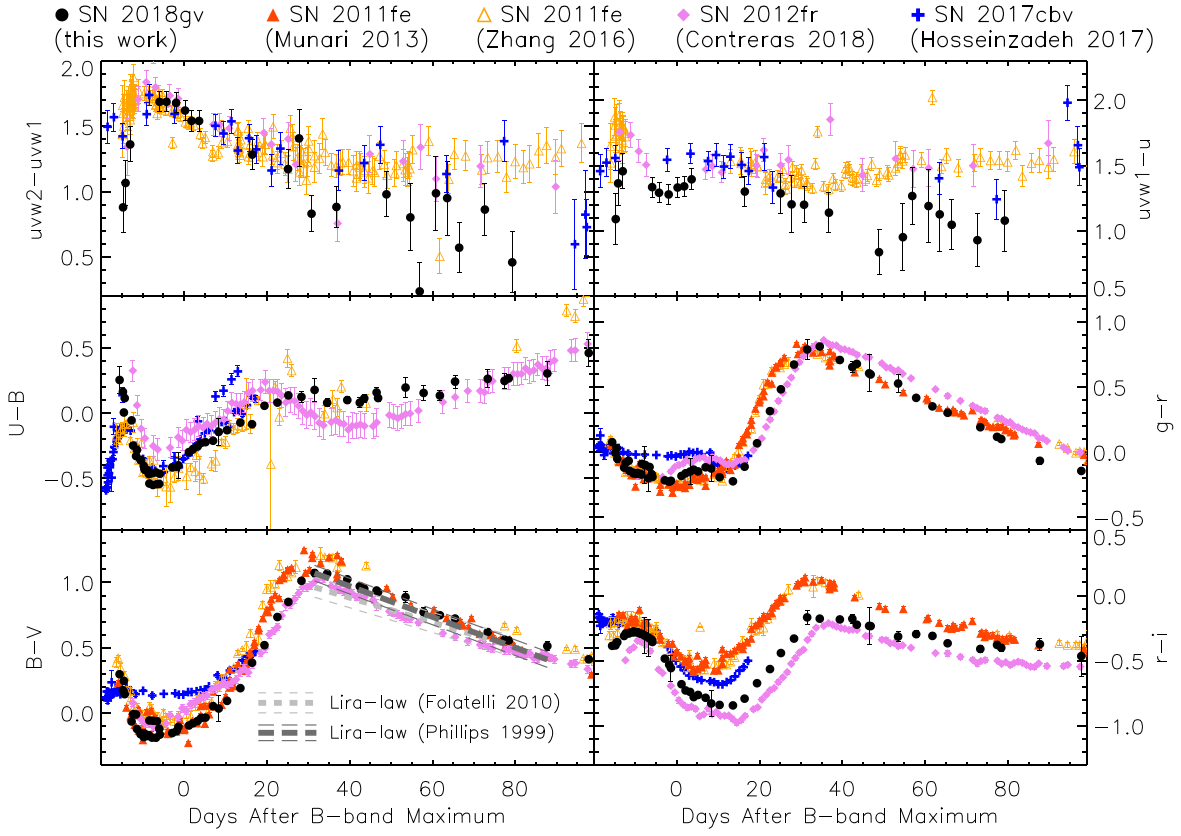
Figure 4. Galactic and host reddening-corrected $uvw2-uvw1$, $uvw1-u$, $U-B$, $B-V$, $g'-r'$, and $r'-i'$ color curves of SN 2018gv compared with the Galactic reddening-corrected color curves of SN 2011fe, SN 2012fr, and SN 2017cbv.

as the surface area of the expanding fireball, and therefore the SN flux (f) should increase quadratically with time (Riess et al. 1999). This $f \propto t^2$ relation reasonably describes the composite light curves collected from surveys (i.e., Riess et al. 1999; Goldhaber et al. 2001; Conley et al. 2006; Garg et al. 2007; Hayden et al. 2010; Ganeshalingam et al. 2011; Firth et al. 2015) and some of the very well-sampled individual SNe Ia (i.e., SN 2011fe, Nugent et al. 2011). A more fundamental explanation of the $f \propto t^2$ relation is provided by Arnett (1982), which considers radioactive heating and photon diffusion. Nonetheless, such an oversimplified expanding fireball may not be sufficient to explain the nonuniform and time-variant rising of SNe Ia in the first $\sim$3 days (for instance, SN 2013dy, Zheng et al. 2013, and iPTF16abc, Miller et al. 2018).

We model the early g'-band flux as a function of time from SN 2018gv as a power law:

$$f(t) \propto (t - t_0)^n, \qquad (4)$$

where t_0 gives the time of first light and n denotes the index of the power law. The best fit to the first 6.5 days after the estimated explosion gives $n = 2.43 \pm 0.48$ and a rise time $t_{rise} = t_{Bmax} - t_0 = 18.51 \pm 0.92$ days; this is consistent with the fit using the first 6.0 days light curve (i.e., $n = 2.59 \pm 0.56$ and $t_{rise} = 18.79 \pm 1.07$ days). The fit adopting the photometry within the first 7.0 days gives $n = 1.89 \pm 0.18$ and $t_{rise} = 17.53 \pm 0.38$ days. Different time ranges adopted to diverse early light-curve sampling makes it difficult to robustly compare the behaviors of various cases. We also fitted the early g'-band light curve using a single power law up to the point that the luminosity reaches 40% of the peak following the three

SNe Ia presented by Olling et al. (2015). The rising time and the power-law index yield 19.26 ± 0.67 days and 2.79 ± 0.28, respectively. One can see that the power-law index and the estimated rising time are broadly consistent with the mean values deduced by previous studies based on relatively arbitrary choices of the time range. Stringent constraints on the early photometric evolution of SN 2018gv, however, cannot be placed without a complete light-curve coverage of the early phases.

For comparison, the model was also fitted to the early g-band flux of SN 2011fe, which yields one of the most comprehensive observed normal SNe Ia with photometry at $\sim$1 day after the explosion. In addition to adopting the g'-band photometry from Nugent et al. (2011), we also apply the transformations of Jordi et al. (2006) to convert the photometry by Zhang et al. (2016) from the $UBVRI$ magnitude system to the Sloan $ugriz$ system. A better sampled early g-band flux curve of SN 2011fe was then obtained by combining the two sources. The $f \propto t^n$ power law was fitted to the early (i.e., within 4 days of the estimated time of explosion) g-band flux. We obtain $n = 2.20 \pm 0.09$, which is marginally consistent with $n = 2.01 \pm 0.01$ derived by Nugent et al. (2011). The same conclusion holds for the data within the first 5 days (e.g., $n = 2.03 \pm 0.14$).

In a few cases, the early flux from the SNe exhibits significant deviations from the $f \propto t^2$ model. For example, the blue bump in the U, B, and g'-band light curves of SN 2017cbv during the first 5 days can be explained by interactions between the ejecta and the companion or immediate circumstellar material (Hosseinzadeh et al. 2017). The flux evolution of iPTF16abc during the first $\sim$4 days can be modeled by the
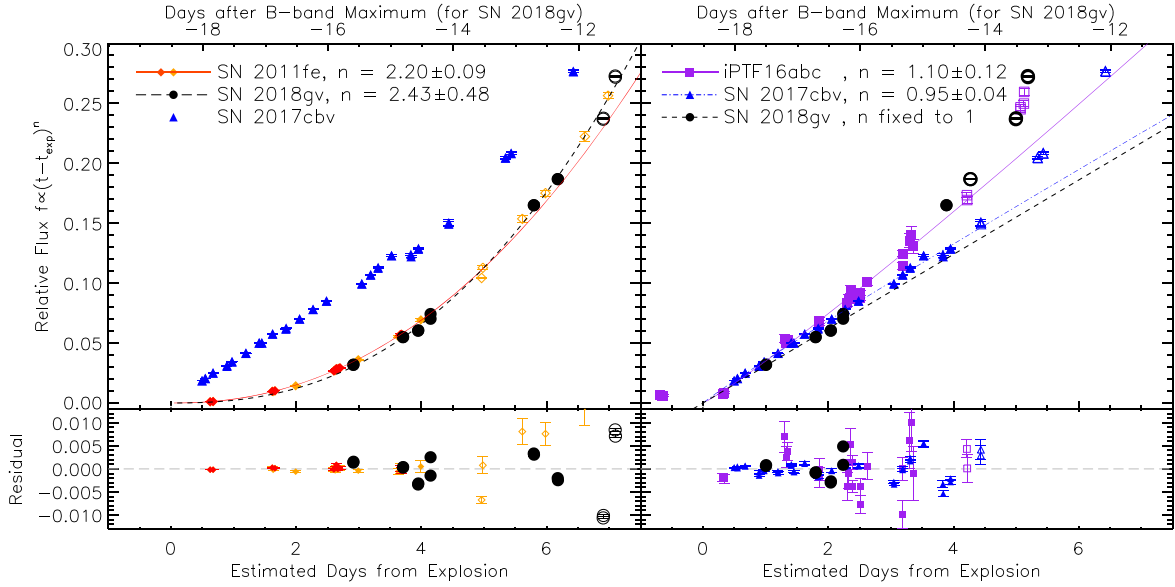
Figure 5. Best-fit $f \propto t^n$ model to describe the early g'-band flux from SN 2018gv compared to the early flux evolution of other SNe that have well-sampled early light curves. In the upper-left panel, the black-dashed line shows the fitting of SN 2018gv, which allows n to vary. The red-solid line fits the early g-band flux of SN 2011fe. The orange diamonds indicate the B-band flux of SN 2011fe. In the upper-right panel, the gray-dashed line indicates the linear fit, assuming the early flux evolution of SN 2018gv is similar to SN 2017cbv and iPTF16abc; a blue bump has been observed within 5 days after their estimated time of explosion. The residuals are shown in the bottom panels.

power law with $n = 0.98$ (Miller et al. 2018). The photometric and spectroscopic behaviors of iPTF16abc can be best explained by strong ^{56}Ni mixing in the SN ejecta. In these two cases, the early flux can be well characterized by $n \sim 1$.

To test whether SN 2018gv has such a nature, we fit the $f \propto t^n$ law to its early flux by fixing $n = 1$. The fluxes during the first 4 days after the estimated time of the explosion were adopted. After day 4, the fluxes of SN 2018gv display large deviations from the linear model. For comparison, the $f \propto t^n$ modeling to the fluxes of iPTF16abc and SN 2017cbv in similar phase spanning gives $n = 1.10 \pm 0.12$ and $n = 0.95 \pm 0.04$, respectively; both coincide with the linear model. We conclude that the early flux of SN 2018gv does not favor an $n \sim 1$ index due to the large deviations from the linear model after day 4. Figure 5 summarizes our investigation of the early flux evolution of SN 2018gv and several other SNe discussed previously. In all cases, the fits were forced to go through the origin, which determines the time of explosion. Filled symbols represent the data point used in each case. Data points shown by the corresponding open symbols were not used in the fitting. The left panel presents the fitting to the early flux curve of SN 2018gv, which allows n to vary. The right panel tests the case of n fixed to 1. The best fits for SN 2018gv and other SNe are shown by dashed lines and solid lines, respectively. Estimates based on different assumptions for the light-curve shape at early phases yield different times of explosion. We concede that the relatively sparsely sampled early light curve is not sufficient to constrain the first light of SN 2018gv. Overall, based on the test and comparisons provided, we consider that the early flux evolution of SN 2018gv more resembles the average behavior of normal SNe Ia.

4. Spectroscopy

Figure 6 presents the spectral sequence of SN 2018gv. A total number of 26 optical low-resolution spectra spanning from $t \sim -15.2$ to $+83.6$ days relative to the B-band maximum light

were obtained. All spectra were corrected for the redshift of the host galaxy and smoothed by rebinning the data to 3 Å. The wavelength scale was corrected to the rest frame using the host-galaxy recessional velocity (1582 km s^{-1}) as described previously.

Figure 7(a) compares the earliest spectrum of SN 2018gv at day -15.2 with the spectrum of SN 2011fe at day -16. The earliest spectrum of SN 2018gv exhibits several prominent broad and blueshifted absorption features near 3630 Å due to Ca II H&K, (rest-frame wavelength $\lambda_0 \sim 3969, 3934$ Å); the characteristic "W"-shaped S II lines of the SN Ia spectra before and around the peak ($\lambda_0 \sim 5454, 5640$ Å); the distinctive strong absorption features around 6020 Å due to Si II ($\lambda_0 \sim 6355$ Å, denoted as Si II $\lambda6355$ hereafter); and around 7890 Å due to the Ca II NIR triplet ($\lambda_0 \sim 8579$ Å, denoted as Ca II NIR3 hereafter). The C II $\lambda6580$ and the O I $\lambda7774$ are both identified in the earliest spectra. Oxygen in the ejecta of SNe Ia can be unburned fuel or a product of carbon burning. Apart from an absence of a shoulder on the red wing of the Ca II NIR3 in the SN 2018gv spectrum, we suggest that the spectral features and their strength in the earliest spectrum of SN 2018gv exhibit considerable similarities to those of the SN 2011fe.

By $t \sim -2$ days (shown in Figure 7(b)), the width of the broad absorption feature associated with Si II $\lambda6355$ develops into a narrower profile, while the adjacent C II $\lambda6580$ feature is no longer distinguishable in our observations of SN 2018gv. C II $\lambda6580$ is marginally detected in the comparison spectrum of SN 2011fe at an earlier epoch of -5 days. An asymmetric and broad absorption profile is identified in the wavelength range of Ca II NIR3, indicating the existence of a high-velocity (HV) component and a normal-velocity (NV) component of the Ca II feature. These two components were blended in the earliest spectra and become shallower. The decomposition and a detailed study of the Ca II NIR3 features of SN 2018gv will be presented in the following subsection. The HV and NV components of the Ca II NIR3 become shallower than those observed at -15 days. At $+13$ (Figure 7(c)) and $+84$ days (Figure 7(d)), significant similarities between the spectral
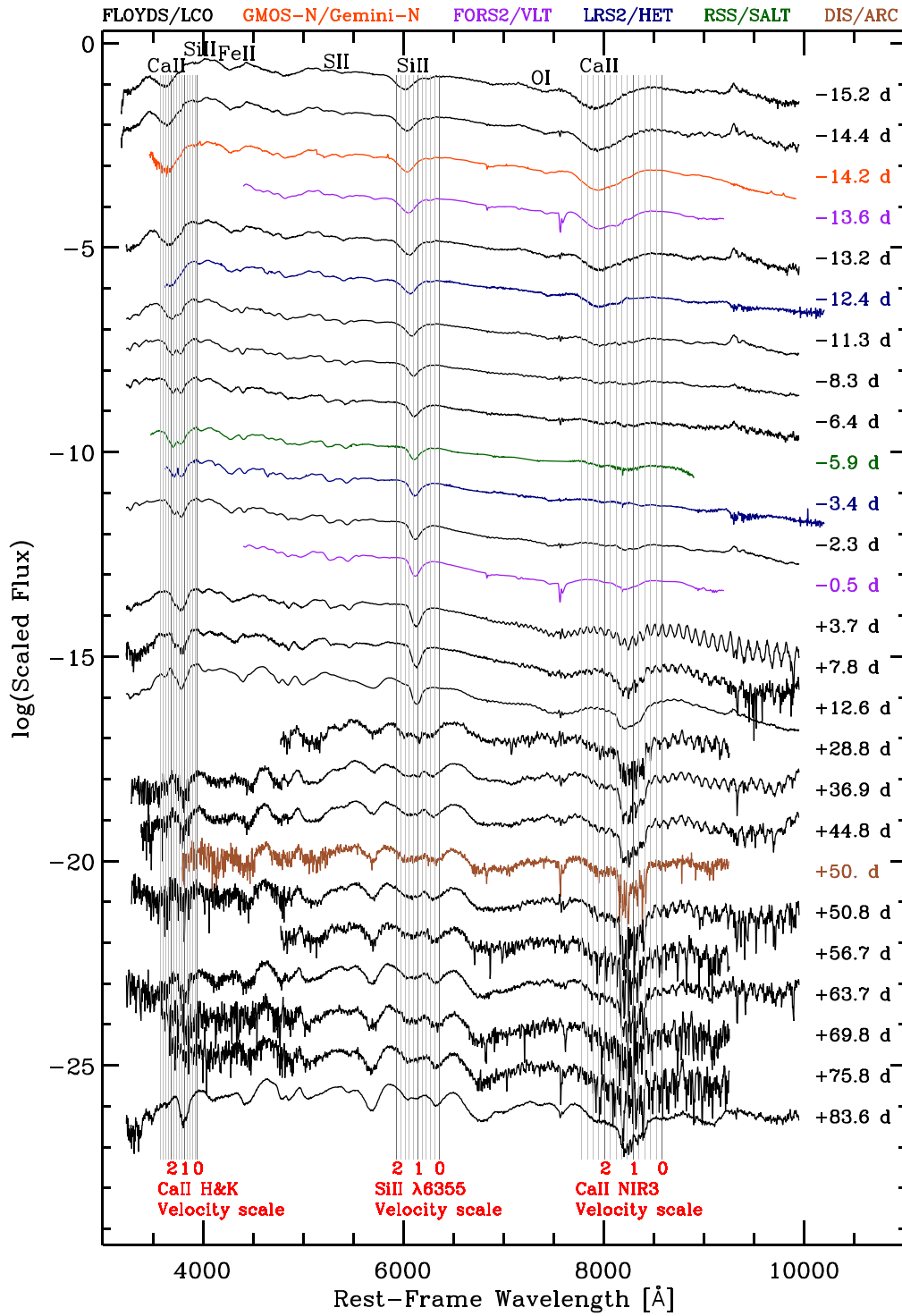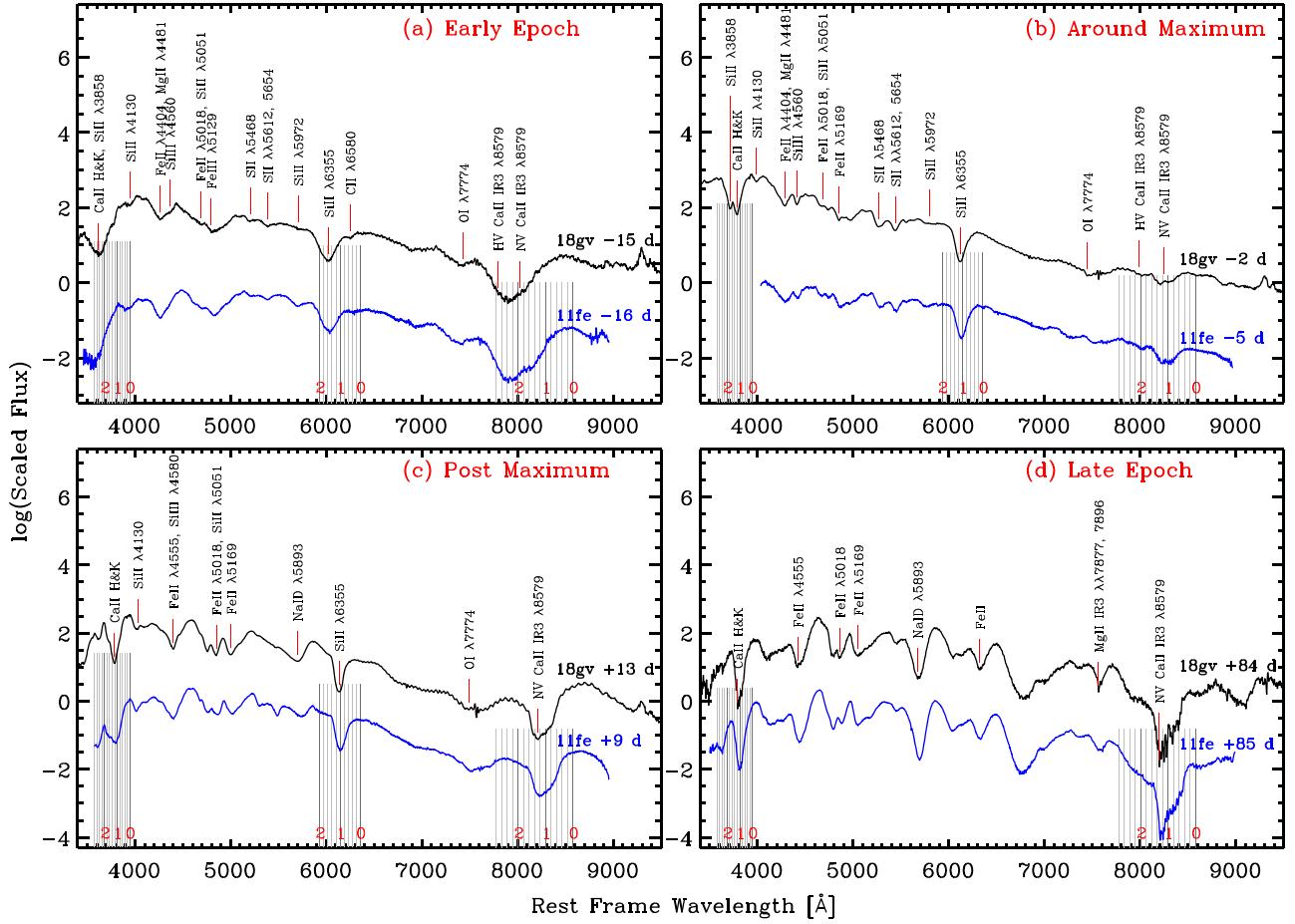
Figure 6. Spectral time series of SN 2018gv (solid curves; phase is the label on the right). The wavelengths corresponding to 0, $-10,000$ and $-20,000$ km s^{-1} around the features indicated by the text are shown as thick gray lines, with 2000 km s^{-1} intervals denoted by thin gray lines. For the purpose of presentation, all spectra were binned to 3 Å.

evolution of SN 2018gv and SN 2011fe can be identified. In the following subsections, we detail the spectral evolution of SN 2018gv within the first $\sim$100 days.

4.1. Evolution of the Features around Si II λ6355 and Ca II NIR Triplet

The prominent Si II λ6355 absorption feature in the early spectra suggests the spectral evolution of SN 2018gv resembles

other normal SNe Ia. The highest velocity measured across the Si II λ6355 line is $\sim$$-16,000$ km s^{-1} and a blue wing out to about 22,000 km s^{-1} at $t \sim -15.2$ days. The Si II λ6355 velocity for SN 2018gv measured from the spectra at -0.5 day is found to be $\sim$$-11,000$ km s^{-1}. This is consistent with the interpolation of the exponential fitting to the time-evolution of the velocity profile (i.e., $-10,870$ km s^{-1}). These measurements suggest that SN 2018gv should be classified as a normal-velocity

Figure 7. Spectra of SN 2018gv (black) at different epochs compared with the spectra of SN 2011fe (blue) at similar phases (Zhang et al. 2016). The wavelengths corresponding to 0, −10,000 and −20,000 km s^{-1} around the features indicated by the text are shown as thick gray lines, with 2000 km s^{-1} intervals denoted by thin gray lines. All spectra have been corrected for the redshift of the host galaxy. Several prominent lines at different epochs are labeled. The line identifications adopted here are obtained from Branch et al. (2005, 2006). For the purpose of presentation, all spectra were binned to 3 Å, shifted arbitrarily, and presented in logarithmic scale.

(NV) SN Ia in the scheme of Wang et al. (2009). The expansion velocity gradient calculated directly from the Si II λ6355 at day −0.5 gives $\dot{v} = 36.6 \pm 6.4$ km s^{-1} day^{-1}. The calculation is also consistent with the velocity gradient measured by interpolating the exponential fitting to the same velocities during the period from $t = 0$ to +10 days (i.e., $\dot{v} = 33.3$ km s^{-1} day^{-1}). This is below the threshold of the high-velocity gradient subclass in the classification scheme of Benetti et al. (2005; i.e., $\dot{v} \sim 70$ km s^{-1} day^{-1}). Therefore, we suggest that SN 2018gv belongs to the low-velocity gradient group.

Figure 8 provides the detailed evolution of the Ca II H&K, Si II λ6355, and Ca II NIR3. HV features (HVF) are ubiquitous in the Ca II NIR3 in early phases of SNe Ia (Mazzali et al. 2005). We find no sign of an HV component of Si II λ6355 in the spectral time-sequence of SN 2018gv. The broad and asymmetric Ca II NIR3 profiles indicate multiple velocity components associated with Ca II. The Ca II H&K line may have similar HV components, but they appear to overlap with the Si II λ3858 line at early phases.

In addition to displaying an absorption profile around the "photospheric" velocity, some elements show an HVF that would require noticeably higher velocities (typically a few thousand km s^{-1} above the photospheric velocity). These absorption lines can be attributed to the materials above the SN photosphere, and have been interpreted as the exponentially

declining abundances of Si and other intermediate-mass elements—a signature of detonations in C/O rich material (Quimby et al. 2007). The Doppler-broadened profiles at different velocities often overlap with each other as well as the continuum profile. In order to mitigate the line blending and identify different line profiles, we adopt multiple-component Gaussian functions to fit the Si II λ6355 and the Ca II NIR3, separately. Note that the shape of the absorption feature is dependent on the structure and the velocity distribution of the absorbing material; therefore the profile is intrinsically non-Gaussian and can be complex (Mulligan & Wheeler 2018; Mulligan et al. 2019). One should be cautious about the inferred line properties based on multiple-component Gaussian fitting.

First, following Childress et al. (2014), we assign the blue and red ends of the feature of interest by visually inspecting the data; second, we identify a line segment as the "pseudo-continuum" by connecting the blue and the red end; third, we subtract the flux of the segment profile from the feature of interest; finally, we fit the "pseudo-continuum" removed regions with the multiple-component Gaussian function:

$$f_c(\lambda) = \sum_{i=1}^{n} A_i \exp\left(-\frac{(\lambda_i - \lambda_i^{\text{rest}})^2}{2\sigma_i^2}\right). \tag{5}$$

The fitted parameters are the center wavelength in the rest frame (λ_i), pseudo-equivalent width (σ_i), and absorption depth
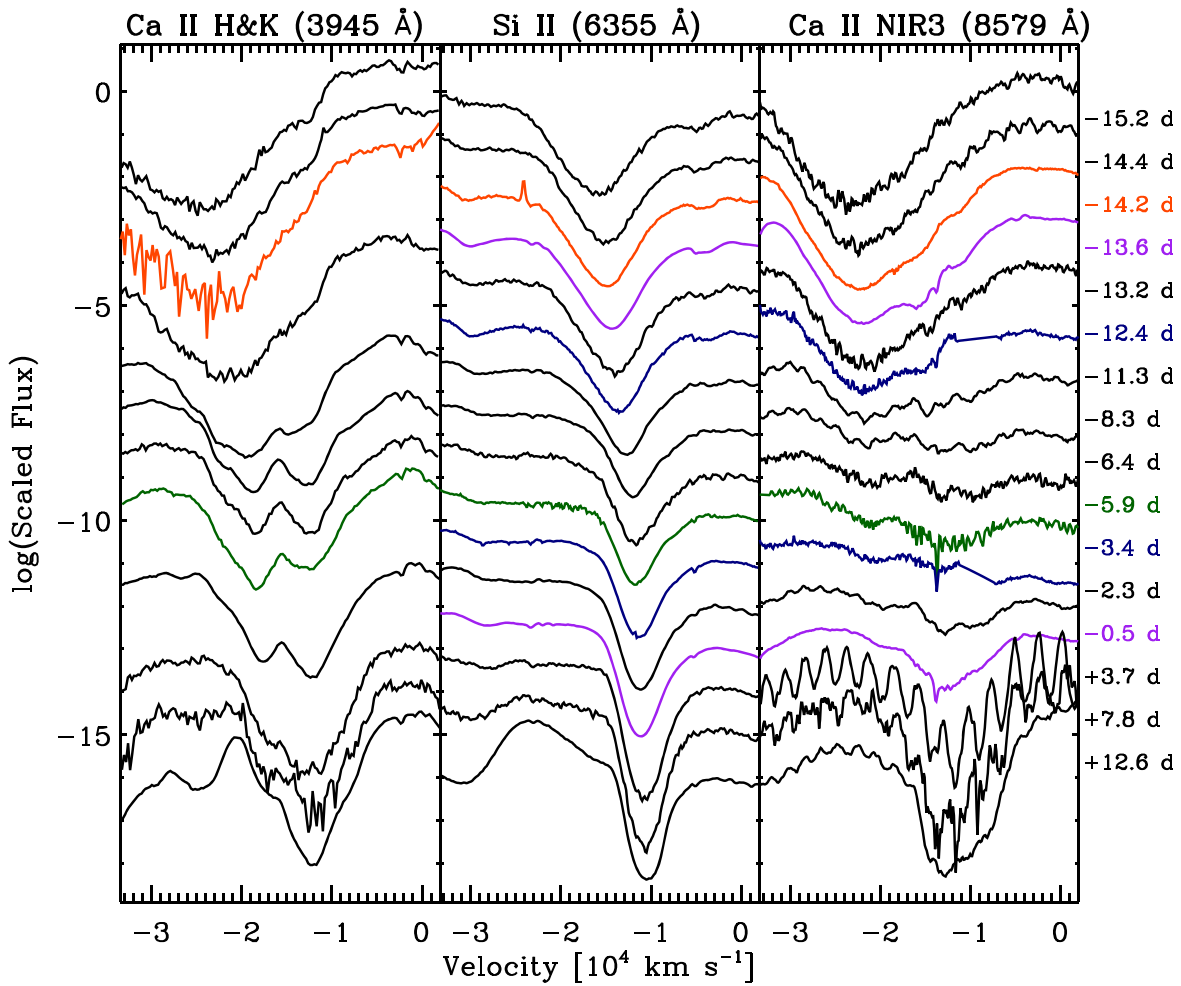
Figure 8. Evolution of Ca II H&K (left panel), Si II λ6355 (middle panel), and Ca II NIR3 (right panel) of SN 2018gv in velocity space. The semi-regular fluctuations in some of the Ca II NIR3 profiles are caused by fringing in the detectors.

(A_i) of each component. A three-component Gaussian function is used to fit the absorption features of the Si II λ5972, Si II λ6355, and C II λ6580 line complex before $t \sim -11$ days. A fourth-component Gaussian function did not find any signature of HV Si II λ6355. The unburned-carbon lines are typically singly ionized (Tanaka et al. 2008) and manifest themselves at the earliest spectra of SNe Ia as weak and time-evolving C II λ6580 absorption lines (e.g., see recent studies of Parrent et al. 2011; Thomas et al. 2011; Folatelli et al. 2012; Silverman & Filippenko 2012). The unburned carbon and oxygen would be accelerated with the expanding layers and trace the ejecta. The C II λ6580 line in SN 2018gv was as strong as the Si II λ5972 in the earliest spectra around 2 weeks before the B-band light-curve peak. It faded rapidly and became indiscernible in the spectra obtained after approximately 1 week before the B-band maximum light, suggesting it is mostly concentrated in the outer part of the ejecta. Therefore, the three-component Gaussian function fitting was only applied before $t \sim -11$ days. The two-component Gaussian fitting procedure has been carried out since $t \sim -11$ days to fit the Si II λ5972 and Si II λ6355 simultaneously. The HV and the photospheric velocity component of the Ca II NIR3 features around the rest-frame wavelength λ8579 Å are also fitted with a two-component Gaussian function. The HV feature was prominent at early phases and faded to almost unseen after

the B-maximum. The fitting procedure, together with the temporal evolution of these two line regions, is illustrated in Figure 9. The velocity evolution of SN 2018gv in early phases is presented in Figure 10.

Starting from about 2 weeks after the B-maximum, as the photosphere recedes more deeply into the ejecta, lines of intermediate-mass elements ($9 \leqslant Z \leqslant 20$) become significantly weaker while the iron-group elements ($21 \leqslant Z \leqslant 30$) like Fe II start to dominate the spectra. The Si II λ6355 absorption feature remains distinct at $v = 10{,}700 \text{ km s}^{-1}$ on day $+12.6$ and has become difficult to identify in the spectra on $+28.8$ and $+36.9$ days.

We measure the pseudo-equivalent width (pEW) of the absorptions of the Si II λ5972, Si II λ6355, C II λ6580, the HV and the NV Ca II NIR3 features and analyze their time evolutions. We also compare the results with those from SN 2011fe as shown in Figure 11. According to Figure 9, these features are all embedded in a well-determined pseudo-continuum. We calculate the pEW (e.g., Garavini et al. 2007; Silverman et al. 2012), defined as

$$\mathrm{pEW} = \sum_{i=1}^{n} \Delta\lambda_i \left(\frac{f_c(\lambda_i) - f(\lambda_i)}{f_c(\lambda_i)} \right), \qquad (6)$$

where λ_i denote the wavelengths of each one of the total N resolution elements in the pseudo-spectrum, ranging from the
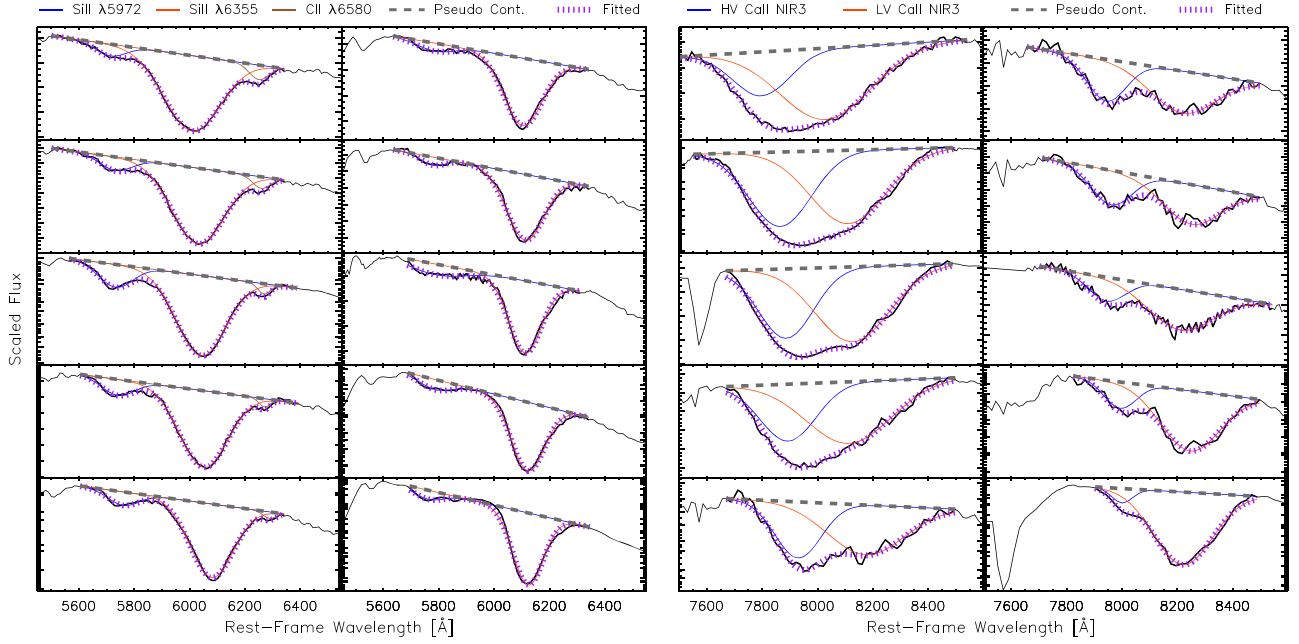
Figure 9. Gaussian fit to the early-time spectra of SN 2018gv. The left panel shows the fit to the region dominated by the Si II λ6355 feature. The fitting shown in the leftmost subpanels has taken into account the Si II λ5972, Si II λ6355, and C II λ6580 features, and the remaining five subpanels show the fitting that does not include C II λ6580. The right panel presents the fit for the region covering both the HVF and photospheric velocity Ca II NIR3 features.
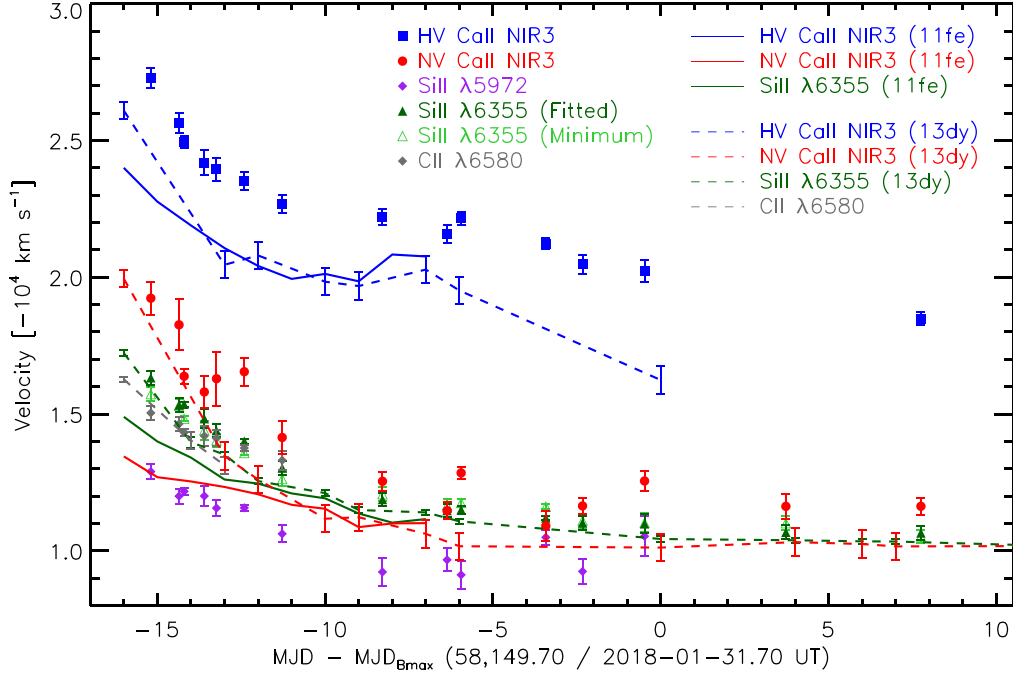

Figure 10. Evolution of the expansion velocity of SN 2018gv in early phases measured from different spectral features including Si II λ5972/6355, C II λ6580, and the HVF, together with the photospheric velocity features of the Ca II NIR3. The central wavelength of each absorption component was determined through the multiple-component Gaussian fitting procedure. The local minima of Si II λ6355 were also overplotted and examined to be consistent with the central wavelength of the same feature obtained by the fitting process. The velocity evolution of the line absorptions for SN 2011fe (Zhao et al. 2015) and SN 2013dy at similar phases (Zhai et al. 2016) is shown for comparison.

blue endpoint to the red endpoint, $\Delta\lambda_i$ gives the width of the ith resolution element, $f(\lambda_i)$ represents the spectral flux at λ_i, and $f_c(\lambda_i)$ is the flux of the pseudo-continuum at λ_i. The 1σ uncertainty of the pEW was derived by error propagation of the uncertainty in the measured flux at each resolution element.

In Figure 11, the pEW of the Si II λ6355 reached a minimum around 73 Å at ∼−6 days. The pEW of the NV component of

Ca II NIR3 reached a minimum of ∼25 Å at a similar epoch around −6 to −2 days and became larger until approximately 1 week after the *B*-band maximum light. The evolution of the pEW of SN 2011fe adopted from Zhao et al. (2015) is shown for comparison. The absorption strength of the HV Ca II NIR3 displays a slower decline in SN 2018gv compared to that of SN 2011fe. Other major absorption features exhibit similar
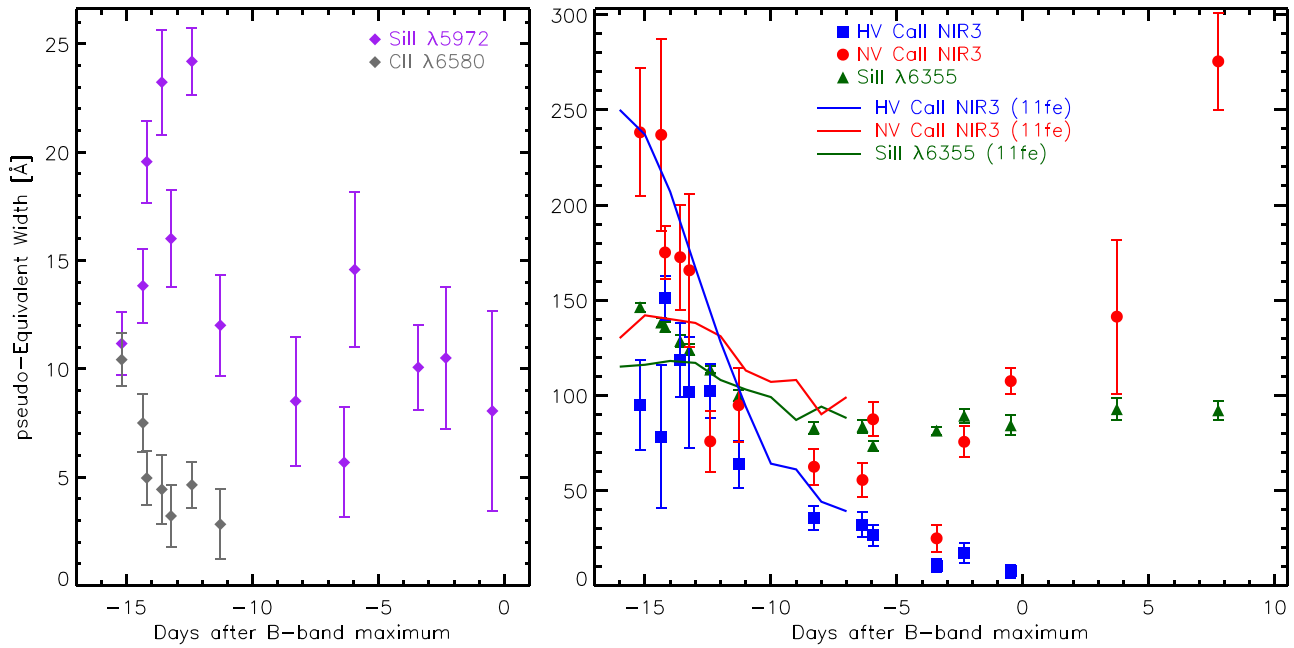
Figure 11. Evolution of the pseudo-equivalent width of SN 2018gv measured for the absorption lines Si II λ5972, C II λ6580 (left panel), Si II λ6355, HVF, and photospheric velocity Ca II NIR3 (right panel). In the right panel, we also compare the measurement of SN 2018gv with SN 2011fe.

trends, as seen in SN 2011fe, as well as several other SNe Ia (e.g., see Figure 15 of Zhang et al. 2016).

The fit results of the different velocity components are presented in Table 5. The uncertainty in the measurement of the absorption velocity was converted from the associated error in wavelength, which has been estimated by adding the propagated error of the fitted center wavelength (see Equation (5)), the rms value in wavelength calibration (typically less than 0.3 Å), and half of the size of the smallest resolution element ($\Delta\lambda/2 = \lambda/2R$), where R gives the spectral resolution in quadrature. The estimated uncertainty mainly depends on the spectral resolution and the S/N of the spectrum. We also conduct a Monte Carlo procedure by randomly choosing the start and end points of the pseudo-continuum within ±5 Å of the assigned values. The uncertainty due to the choice of the line segment that defines the pseudo-continuum is negligible in all quantities presented in Table 5 except the pEW of the C II λ6580. For this relatively weak, short-lived feature, such an effect contributes only less than a quarter of the total error budget of the pEW, even in the most extreme cases. Therefore, we do not include the uncertainty from the choice of the pseudo-continuum.

4.2. Pseudo-bolometric Luminosity

As discussed by Brown et al. (2016), estimating the bolometric luminosity of SNe Ia could be better carried out by employing flux-calibrated spectrophotometry. The diversity in the UV flux distributions, as well as the lack of NIR information, could introduce erratic systematical uncertainties. To better quantify the bolometric characteristics of SN 2018gv, we compute the pseudo-bolometric luminosity of SN 2018gv over a wavelength range from ∼1660 to 8180 Å based on the Swift *uvw*2, *uvm*2, *uvw*1, and the LCO *UBg'Vr'i'*-band photometry. We conduct a similar calculation for SN 2011fe and compare the result to SN 2018gv. As a sanity test, we also compare the pseudo-bolometric luminosity computed based on the spectra of SN 2018gv at different phases with that derived by warping the Hsiao's template. For example, we choose the

spectra of SN 2018gv with high S/N and broad wavelength coverage, register them to the nearest photometric phase, calibrate the spectra to match the photometry in the optical bandpasses, and integrate over the same wavelength range as the calculation based on the Hsiao's templates. The optical pseudo-bolometric luminosities computed from these two approaches are well agreed within the uncertainty. The construction of the spectral energy distribution (SED) of SN 2018gv is illustrated by Figure 12, and the steps are detailed in Appendix C.

The UV-optical pseudo-bolometric light curve of SN 2018gv is shown in Figure 13. For comparison, we also apply the same procedure to the Swift *uvw*2, *uvm*2, *uvw*1, and the *UBVRI* photometry (Zhang et al. 2016) of SN 2011fe. The presented results of SN 2018gv in the associated figures and tables are based on a distance derived from the host's redshift. We adopt a Cepheid distance modulus of 6.4 Mpc for SN 2011fe (Shappee & Stanek 2011), which is the same as the distance applied in the bolometric luminosity calculation conducted in Zhang et al. (2016). The calculated pseudo-bolometric light curve of SN 2011fe is also shown in Figure 13. The integration of the SN 2011fe SED was performed over the same wavelength range as SN 2018gv. The middle panel presents the ratio of the UV (1660–3200 Å) to optical (3270–8180 Å). The UV/optical flux ratio ($F_{UV}/F_{Optical}$) of SN 2018gv is comparable to that of SN 2011fe, both of which reached their peak about 6 days earlier than the bolometric luminosity. This suggests a relatively short diffusion time for their higher-energy photons. We also calculated the fraction of UV to optical flux relative to the total bolometric luminosity over the wavelength range of 1660–24000 Å ($F_{UV - Optical}/F_{Total}$) by integrating the composite spectral template created by Hsiao et al. (2007). This fraction was divided from the pseudo-bolometric luminosity for both SNe to provide a raw estimation of their bolometric luminosity, which is shown by the dashed lines in the first panel.

Table 5
Fit Results of the Different Velocity Components, Velocities Shown in Absolute Value

Phase (days)	Si II λ5972 v (km s⁻¹)	Si II λ5972 pEW (Å)	Si II λ6355 v (km s⁻¹)	Si II λ6355 pEW (Å)	C II λ6580 v (km s⁻¹)	C II λ6580 pEW (Å)	High-velocity Ca NIR3 v (km s⁻¹)	High-velocity Ca NIR3 pEW (Å)	Normal Velocity Ca NIR3 v (km s⁻¹)	Normal Velocity Ca NIR3 pEW (Å)
−15.18	12894(277)	11.2(1.4)	16321(245)	146.3(2.3)	15038(254)	10.4(1.2)	27297(369)	94.9(23.8)	19233(610)	238.2(33.6)
−14.34	11996(277)	13.8(1.7)	15322(245)	138.2(2.4)	14635(261)	7.5(1.3)	25636(373)	78.2(37.6)	18260(930)	236.9(50.6)
−14.19	12172(138)	19.6(1.9)	15354(92)	136.0(2.5)	14322(134)	5.0(1.3)	24942(203)	150.9(11.5)	16379(278)	175.0(14.0)
−13.59	11999(375)	23.2(2.4)	14769(343)	123.8(4.0)	14209(386)	4.1(2.1)	24187(456)	118.4(19.5)	15804(582)	172.5(27.5)
−13.23	11559(289)	16.0(2.3)	14390(246)	124.0(2.9)	14112(285)	3.2(1.4)	23941(424)	101.5(29.1)	16290(988)	165.7(40.3)
−12.40	11569(115)	24.2(1.5)	14004(86)	113.5(1.9)	13755(125)	4.6(1.1)	23528(330)	102.2(14.2)	16546(504)	75.7(16.0)
−11.27	10619(316)	12.0(2.3)	13029(247)	99.8(2.8)	13309(342)	2.8(1.6)	22686(336)	63.6(12.2)	14142(589)	94.7(19.3)
−8.28	9225(507)	8.5(3.0)	11873(248)	82.6(3.1)			22200(302)	35.5(6.3)	12539(341)	62.4(9.6)
−6.36	9667(422)	5.7(2.5)	11468(248)	83.6(3.3)			21579(316)	32.0(6.5)	11466(319)	55.4(8.7)
−5.94	9117(522)	14.6(3.6)	11499(154)	73.4(2.7)			22148(241)	26.3(5.5)	12846(216)	87.4(8.8)
−3.41	10490(275)	10.1(2.0)	11199(87)	81.4(2.1)			21217(199)	10.4(3.4)	10905(541)	24.8(7.2)
−2.32	9244(441)	10.5(3.3)	11022(248)	89.2(3.6)			20467(130)	17.3(5.2)	11639(283)	75.5(8.1)
−0.47	10533(727)	8.1(4.6)	10984(345)	84.2(5.3)			20227(410)	7.4(3.6)	12551(350)	107.4(6.8)
3.74			10673(251)	92.7(5.7)					11673(458)	141.3(40.5)
7.76			10650(249)	92.1(5.0)			18483[a]		11626(311)	275.5(25.3)

Note.
[a] Multi-Gaussian component fitting failed. Velocity assigned by the local minimum and no error estimation applied.
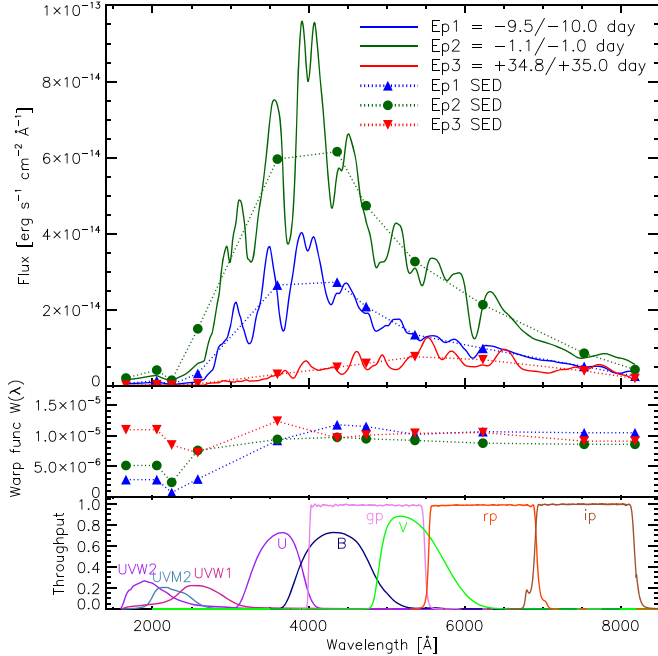
Figure 12. Constructed SED for SN 2018gv. In the upper panel, dots in three different colors show the bandpass monochromatic flux from each of three observations at their effective wavelengths. Dotted lines show the SED constructed with the warping procedure, and solid lines present the warped spectra from Hsiao's template (Hsiao et al. 2007) for the nearest integer epoch (see legend). The middle panel gives the value of the warp function. The lower panel presents the associated bandpasses throughput curves for the SN 2018gv observations.

We tabulate the pseudo-bolometric luminosity of SN 2018gv and SN 2011fe calculated within the UV to optical wavelength ranges within the first 100 days after the B-band peak in Table 6. For each SN, the estimated UVOIR luminosity is also presented, which has a similar error as the UV-Optical pseudo-bolometric luminosity. The maximum value of the UV-optical pseudo-bolometric luminosities of SN 2018gv is consistent with the peak value of SN 2011fe. Assuming SN 2018gv has

the same NIR/optical flux ratio ($F_{NIR}/F_{Optical}$) as SN 2011fe, we estimate the peak bolometric luminosity of SN 2018gv to be $\log L = (43.074 \pm 0.023 \pm 0.008)$ erg s⁻¹. The first and the second uncertainties represent the statistical error and the error due to the distance, respectively. Following Stritzinger & Leibundgut (2005), the peak bolometric luminosity produced by the radioactive ^{56}Ni can be written as

$$L_{max} = \left(6.45 e^{-\frac{t_r}{8.8 \text{ days}}} + 1.45 e^{-\frac{t_r}{111.3 \text{ days}}}\right)\left(\frac{M_{Ni}}{M_\odot}\right)$$
$$\times 10^{43} \text{ erg s}^{-1}, \tag{7}$$

where t_r is the rise time of the bolometric light curve and M_{Ni} denotes the synthesized nickel mass in the SN ejecta. A high-order polynomial fit to the bolometric light curve from $t = -15$ to $+15$ days suggests that the bolometric luminosity peaked around $t = -1.1 \pm 2.4$ days relative to the B-band maximum. This is consistent with the mean of the distribution of the time difference between the bolometric light-curve peak and the B-band maximum (see, e.g., Scalzo et al. 2014). Adopting a B-band rise time of 18.51 ± 0.92 days estimated in Section 3.4 and peak luminosity of $L = (1.186 \pm 0.064 \pm 0.022) \times 10^{43}$ erg s⁻¹, we derive a nickel mass of $0.56 \pm 0.08 M_\odot$ for SN 2018gv. The derived peak luminosity and the associated nickel mass based on a SNooPy-fitted luminosity distance yield $L \approx 1.38 \times 10^{43}$ erg s⁻¹ and $0.65 M_\odot$, respectively. These results are also consistent to the estimation assuming a typical bolometric rise time of 19 ± 3 days (i.e., $M_{Ni} \approx 0.59 \pm 0.09 M_\odot$), according to the Arnett law (e.g., see Arnett 1982, and Equation (7) in Stritzinger & Leibundgut 2005). These results are consistent with the nickel mass derived based on the peak of the UVOIR luminosity of $L = 1.191 \times 10^{43}$ erg s⁻¹.

Regarding the sanity test simultaneously performed on SN 2011fe, we noticed that the peak pseudo-bolometric luminosity of SN 2011fe derived over a wavelength range of 1660–8180 Å ($\log L = 43.011 \pm 0.016$ erg s⁻¹) is systematically lower than the UVOIR bolometric luminosity calculated
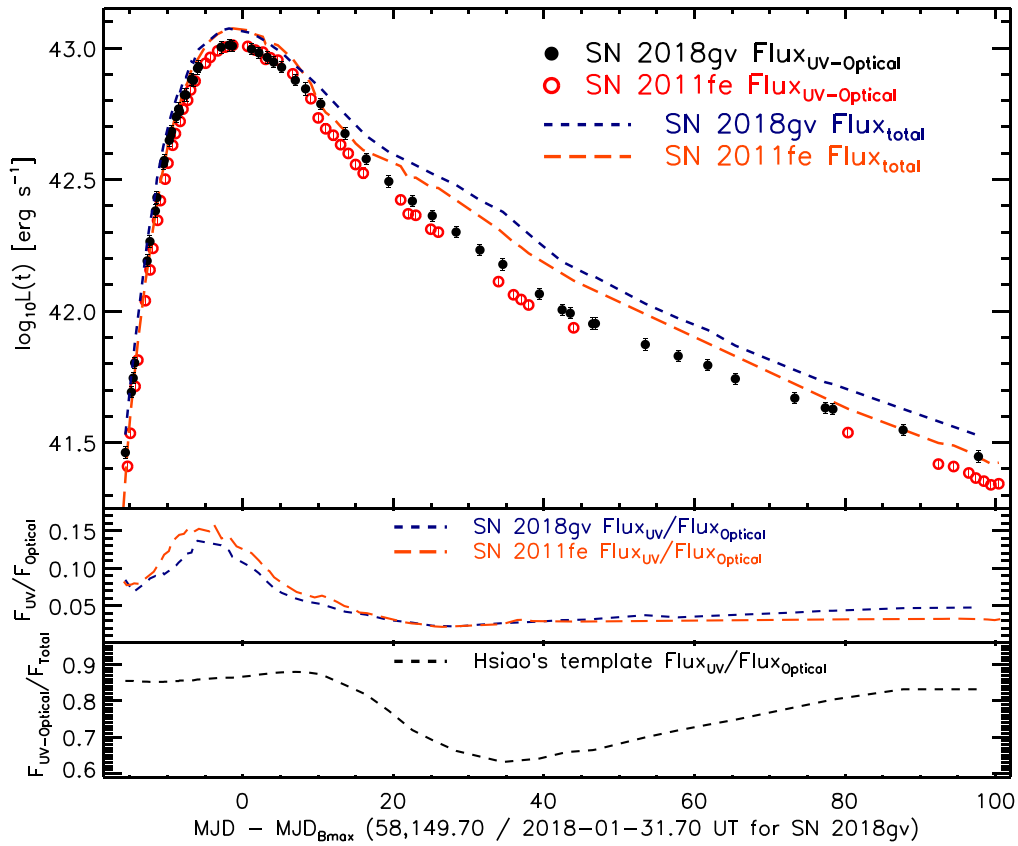
Figure 13. Constructed quasi-bolometric light curves of SN 2018gv (upper panel). The filled black circles represent the bolometric luminosity integrated within a wavelength range of 1660–8180 Å; the open red circles estimate the bolometric luminosity based on the fraction of optical to total bolometric luminosity computed using the Hsiao's template, which is shown by the gray line in the lower panel. The middle panel presents the ratio of the UV (1660–3200 Å) to optical (3270–8180 Å) flux of SN 2018gv, compared to that of SN 2011fe. The fluxes were derived by integrating the composite spectral template (Hsiao et al. 2007), as described in Section 4.2.

considering the SED over 1600–24000 Å (log L = 43.05 erg s^{-1}, with a typical uncertainty of 0.07 dex, dominated by the uncertainty in the distance Zhang et al. 2016). This discrepancy of ~8.6% in the peak bolometric luminosity is due to the construction of the pseudo-bolometric light curves because we do not account for the NIR fluxes. After correcting for the ~9% $F_{NIR}/F_{Optical}$ ratio around the peak, the bolometric luminosity of SN 2011fe log L = 43.07 erg s^{-1} is consistent with Zhang et al. (2016) and Pereira et al. (2013) and confirms the sanity of the method.

5. Spectropolarimetry

Spectropolarimetry of SN 2018gv obtained at day −13.6 (epoch 1) and day −0.5 (epoch 2) relative to the B-band maximum light, together with the associated flux spectra in the rest frame, is shown in Figures 14 and 15, respectively. Because of the low and decreasing level of the continuum polarization, the Stokes parameters measured at different wavelengths at the second epoch are overall close to zero, which leads the deduced position angle (PA) measured for interstellar-polarization (ISP)–subtracted data to display random orientations; therefore, we only show the PA calculated before ISP removal.

5.1. Interstellar Polarization

Light from SNe always suffers from the extinction caused by the interstellar dust grains along the line of sight, in both the

Milky Way and their host galaxies. Dichroic extinction by partially aligned nonspherical paramagnetic interstellar dust grains will polarize the traversed photons, which causes the observed ISP. The removal of the ISP is essential to determine the intrinsic polarization of SNe. An upper limit on the dichroic extinction-induced polarization by Milky Way–like dust grains yields $p_{ISP} < 9 \times E(B − V)$ (Serkowski et al. 1975). Assuming both the Galactic and the SN 2018gv host dust follow a similar $R_V = 3.1$ extinction law (Cardelli et al. 1989), the upper limits on the ISP derived from the Milky Way and the host galaxy NGC 2525 reddenings (derived from the values listed in Table 4) yield $p_{ISP}^{MW} < 0.46\%$ and $p_{ISP}^{Host} < 0.20\%$, respectively.

Following a similar procedure to the spectropolarimetric analysis of SN 2012fr (Maund et al. 2013), we estimate the ISP toward SN 2018gv as $Q_{ISP} = 0.07\% \pm 0.16\%$, $U_{ISP} = −0.49\% \pm 0.09\%$. The corresponding degree and position angle are $p_{ISP} = 0.50\% \pm 0.09\%$ and $PA_{ISP} = 139°.0 \pm 5°.2$, respectively. Detailed information of the ISP estimation is reported in Appendix D. Notice that due to the relatively low ISP suggested by the low extinction toward SN 2018gv, we adopted a wavelength-independent ISP correction to the observations. Before the maximum luminosity, the presence of Fe absorption wings and its line-blanketing depolarization over the wavelength ranges 4800–5600 Å may not be sufficient to characterize the true ISP. Therefore, we would like to stress that the ISP determination described here is only tentative. However, the ISP only resets the origin of the polarization on the Q–U diagram and should not alter the polarized spectral

Table 6
The Pseudo-bolometric (UVO) and the Estimated Bolometric (UVOIR) Luminosity of SN 2018gv (Left) and SN 2011fe (Right)

Phase[a] Day	log L (UVO) (erg s^{-1})	Error[b] (erg s^{-1})	log L (UVOIR) (erg s^{-1})	Phase[c] Day	log L (UVO) (erg s^{-1})	Error[b] (erg s^{-1})	log L (UVOIR) (erg s^{-1})
−15.61	41.463	0.022	41.532	−16.31	40.962	0.016	41.030
−14.81	41.693	0.022	41.761	−15.95	41.151	0.016	41.219
−14.57	41.747	0.022	41.815	−15.32	41.409	0.016	41.478
−14.38	41.805	0.022	41.874	−14.95	41.535	0.016	41.603
−12.72	42.192	0.023	42.261	−14.31	41.713	0.016	41.782
−12.34	42.266	0.023	42.335	−13.95	41.813	0.016	41.882
−11.62	42.382	0.023	42.452	−12.96	42.039	0.016	42.108
−11.42	42.434	0.023	42.503	−12.33	42.156	0.016	42.226
−10.55	42.562	0.024	42.631	−11.96	42.238	0.016	42.308
−10.45	42.574	0.024	42.643	−11.33	42.345	0.016	42.414
−9.78	42.651	0.024	42.720	−10.96	42.420	0.016	42.489
−9.60	42.670	0.024	42.739	−10.33	42.501	0.016	42.571
−9.47	42.685	0.024	42.753	−9.95	42.562	0.016	42.632
−8.87	42.740	0.024	42.809	−9.33	42.630	0.016	42.699
−8.54	42.770	0.024	42.838	−8.96	42.674	0.016	42.743
−8.41	42.760	0.023	42.827	−8.34	42.721	0.016	42.789
−7.78	42.824	0.024	42.891	−7.96	42.767	0.016	42.835
−7.55	42.823	0.023	42.890	−7.34	42.801	0.016	42.869
−6.83	42.883	0.023	42.950	−6.94	42.840	0.016	42.908
−6.57	42.879	0.023	42.946	−6.34	42.874	0.016	42.940
−6.03	42.924	0.023	42.991	−4.96	42.942	0.016	43.007
−5.88	42.931	0.023	42.997	−4.34	42.964	0.017	43.028
−2.89	43.005	0.023	43.069	−3.34	42.989	0.016	43.053
−1.83	43.012	0.023	43.076	−2.34	43.003	0.016	43.067
−1.40	43.010	0.022	43.073	−1.34	43.011	0.016	43.074
1.14	42.998	0.022	43.059	0.65	43.006	0.016	43.067
2.13	42.983	0.022	43.043	1.65	42.992	0.016	43.052
3.23	42.966	0.022	43.024	2.65	42.984	0.016	43.043
4.09	42.948	0.021	43.005	3.03	42.957	0.017	43.015
5.15	42.928	0.021	42.985	3.65	42.963	0.017	43.020
6.97	42.879	0.021	42.935	4.65	42.954	0.017	43.010
8.33	42.847	0.024	42.903	6.64	42.902	0.017	42.957
10.35	42.789	0.021	42.848	9.04	42.807	0.018	42.864
13.57	42.676	0.022	42.750	10.01	42.734	0.018	42.793
16.38	42.580	0.022	42.668	11.01	42.693	0.019	42.755
19.39	42.494	0.022	42.606	12.01	42.668	0.019	42.734
22.52	42.419	0.022	42.562	12.99	42.632	0.019	42.701
25.16	42.364	0.021	42.524	14.00	42.599	0.020	42.673
28.33	42.302	0.022	42.481	14.98	42.557	0.020	42.637
31.50	42.233	0.022	42.423	15.99	42.524	0.020	42.612
34.54	42.179	0.022	42.379	20.97	42.423	0.018	42.551
39.39	42.066	0.022	42.260	21.97	42.370	0.017	42.505
42.41	42.006	0.022	42.189	22.97	42.364	0.017	42.507
43.50	41.993	0.022	42.174	24.97	42.311	0.016	42.471
46.47	41.953	0.023	42.130	25.97	42.300	0.016	42.468
46.84	41.954	0.022	42.131	33.97	42.112	0.016	42.311
53.47	41.874	0.022	42.029	35.96	42.062	0.016	42.262
57.84	41.830	0.022	41.974	36.96	42.044	0.016	42.243
61.77	41.795	0.022	41.929	37.97	42.023	0.016	42.219
65.43	41.744	0.022	41.870	43.95	41.936	0.016	42.116
73.33	41.670	0.022	41.777	80.39	41.538	0.016	41.628
77.38	41.633	0.022	41.731	92.41	41.418	0.017	41.498
78.39	41.629	0.022	41.724	94.43	41.409	0.017	41.489
87.72	41.549	0.022	41.629	96.45	41.384	0.017	41.464
97.73	41.448	0.022	41.528	97.38	41.365	0.017	41.445
⋯	⋯	⋯	⋯	98.45	41.353	0.017	41.433
⋯	⋯	⋯	⋯	99.38	41.339	0.017	41.419

Notes.
[a] Relative to the epoch of B-band maximum of SN 2018gv (MJD = 58,149.698 ± 0.510).
[b] Uncertainty in the distance not included.
[c] Relative to the epoch of B-band maximum of SN 2011fe (MJD = 55,814.48 ± 0.03).
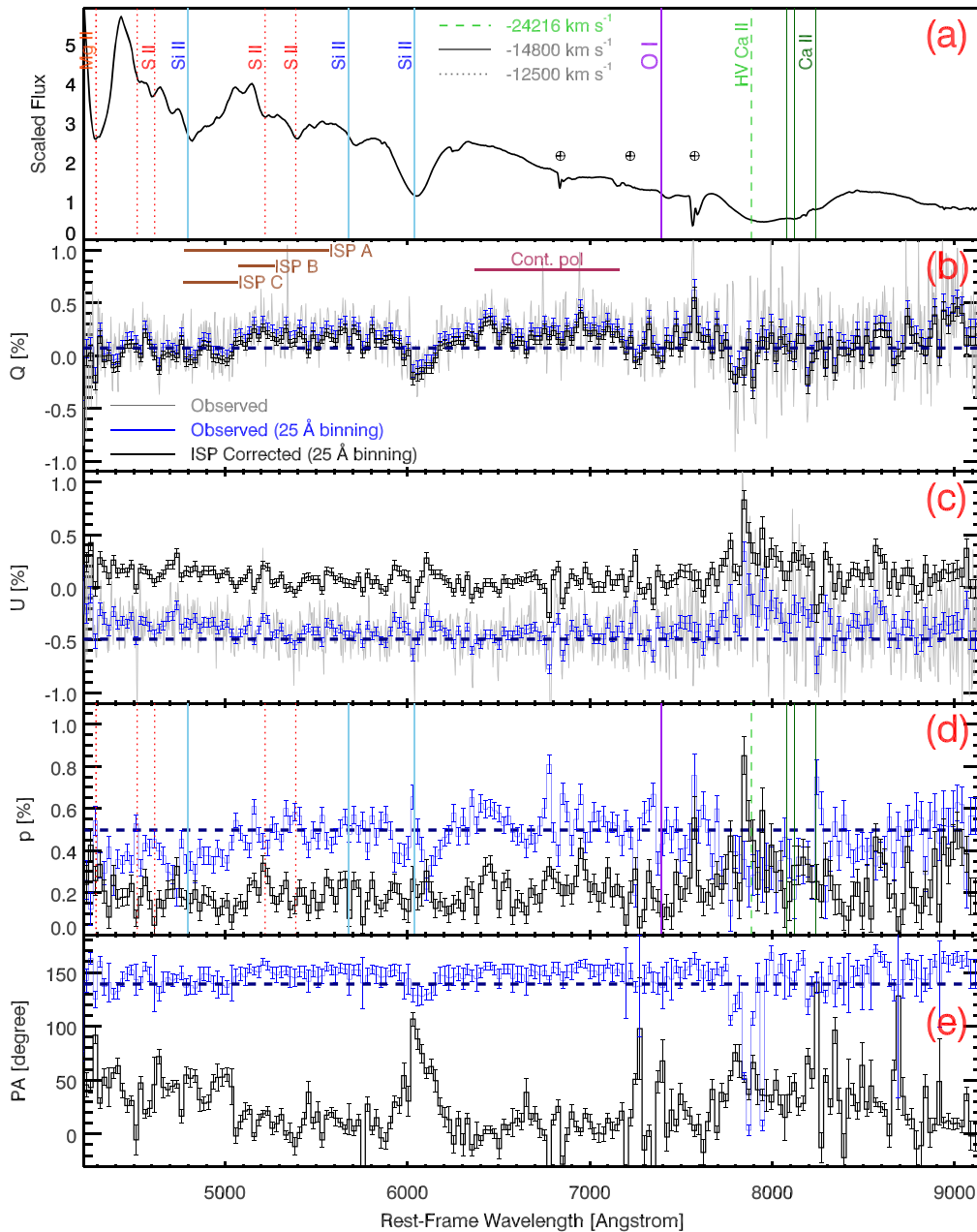
Figure 14. Spectropolarimetry of SN 2018gv at -13.6 days (epoch 1) relative to the B-band maximum light at MJD 58149.698. The five panels (from top to bottom) give (a) the scaled observed flux spectrum with Si II, Ca II, O I, and Mg II lines labeled for different velocities; (b) the normalized Stokes parameter Q; (c) the normalized Stokes parameter U; (d) the polarization spectrum (p); and (e) the polarization position angle PA. Line identifications are provided in the top panel. The diagrams in panels (b)–(e) represent the polarimetry before (blue) and after (black) the ISP correction. The Q and U components of the ISP and the corresponding p and PA are shown by the horizontal gray lines in panels (b)–(e), respectively. The data have been rebinned to 25 Å for clarity.

features. The consistent ISP estimates derived for the two epochs also suggest that the uncertainties in the ISP do not have a strong impact on the interpretation of the intrinsic polarization of SN 2018gv.

5.2. *The* Q–U *Plane and the Dominant Axis*

Plotting the observed spectropolarimetry on the Stokes Q–U plane provides an intuitive diagnostic for investigating the relative behavior of the Stokes parameters of the continuum and for different spectral features (Wang et al. 2001). In most of the cases, the observations indicate the roles of both axisymmetric and nonaxisymmetric components. In the latter case, axisymmetry may be broken by the presence of clumps of different composition, optical depth, and even different velocities. For an axially symmetric structure, the resulting polarization can be described by a single, straight line on the Stokes Q–U plane, namely the "dominant axis" (Wang et al. 2003a)—that is,

$$U = \alpha + \beta Q. \tag{8}$$

Recalling Equation (1), the slope of the line characterizes the PA, which is only related to the position angle of the symmetry axis on the sky. The distance to the origin gives the degree of
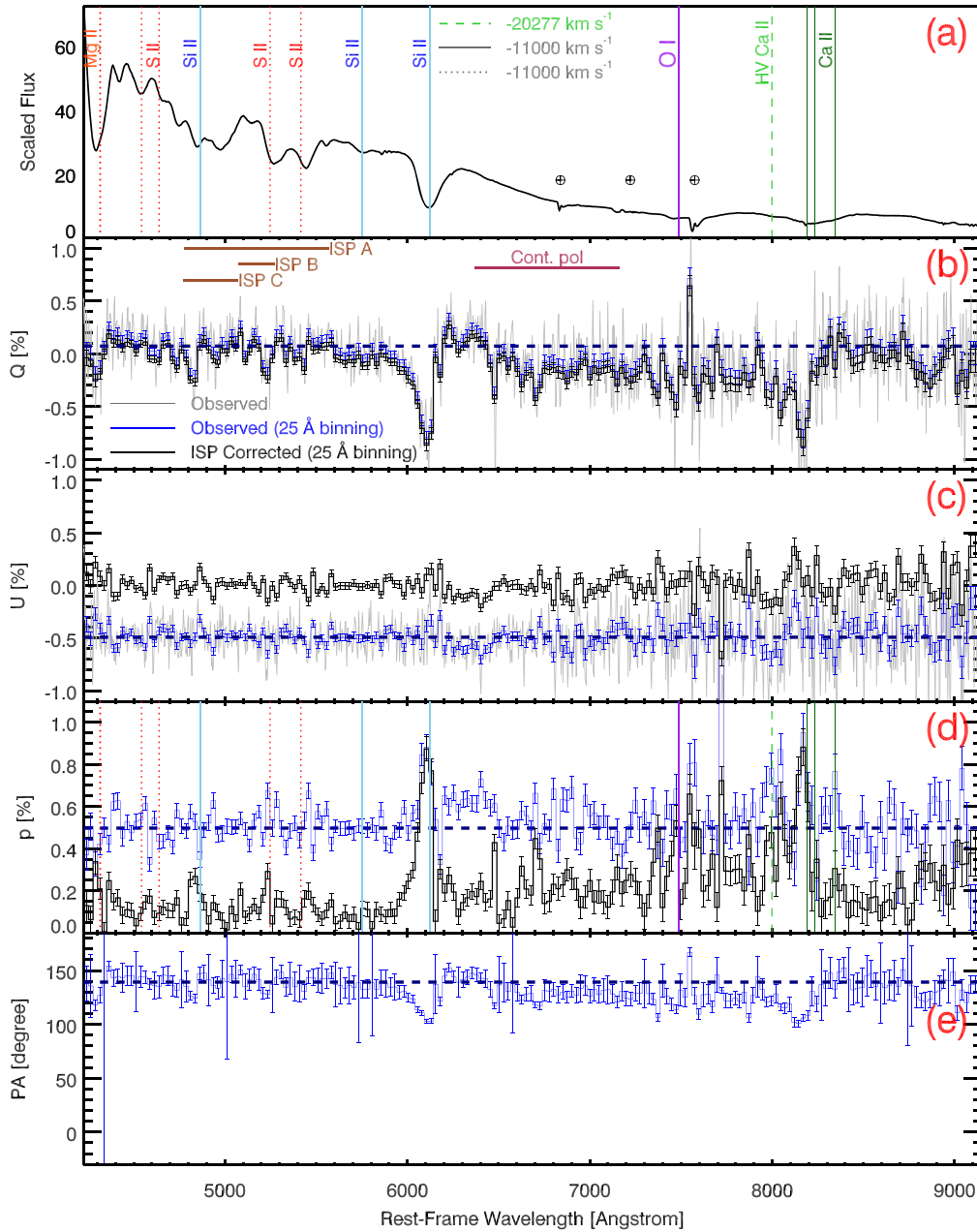
Figure 15. Same as Figure 14, but for spectropolarimetry of SN 2018gv at −0.5 day (epoch 2). Because the intrinsic continuum polarization is very low around maximum brightness, the ISP-subtracted PA exhibits quasi-random values. Therefore, in panel (e), we only present the PA before the ISP correction (blue).

polarization, which is determined by the scattering opacity of different elements.

The polarimetry can therefore be decomposed into two components relative to the dominant axis. Linear least-squares fitting to the polarimetry on the Q–U plane can be used to determine the dominant axis (axis d). Such a dominant direction can sometimes be recognized through the distribution of the points in the Q–U plane. Deviations from the dominant axis, in the perpendicular direction along the orthogonal axis (axis o), indicate departures from axial symmetry. This projection is equivalent to finding the first two principal components (P_d, P_o) of the data or applying a rotation to the Q–U plane; see Equations (1)–(2) of Wang et al. (2003a) and Equations (2)–(3) of Stevance et al. (2017).

Figure 16 shows the ISP-corrected Stokes parameters on the Stokes Q–U plane for both epochs. The determination of the dominant axis of SN 2018gv was conducted for both epochs, by performing an error-weighted linear least-squares fitting to the data. In Figure 16, the black long-dashed lines fit the dominant axis to the observed polarization in the wavelength range $4300 \leqslant \lambda \leqslant 9100\,\text{Å}$, representing the direction of axial symmetry. The direction of the dominant axis changed from $\text{PA} = 168^\circ\!.9 \pm 1^\circ\!.2$ to $178^\circ\!.3 \pm 0^\circ\!.7$. We suggest that a dominant axis seems to be present at both epochs, and it is almost parallel to the U-axis. Though the observations complied with a dominant axis, the large values of χ^2 as labeled on the lower-left corner of each panel indicate that the data are poorly described by just a linear relation. Large
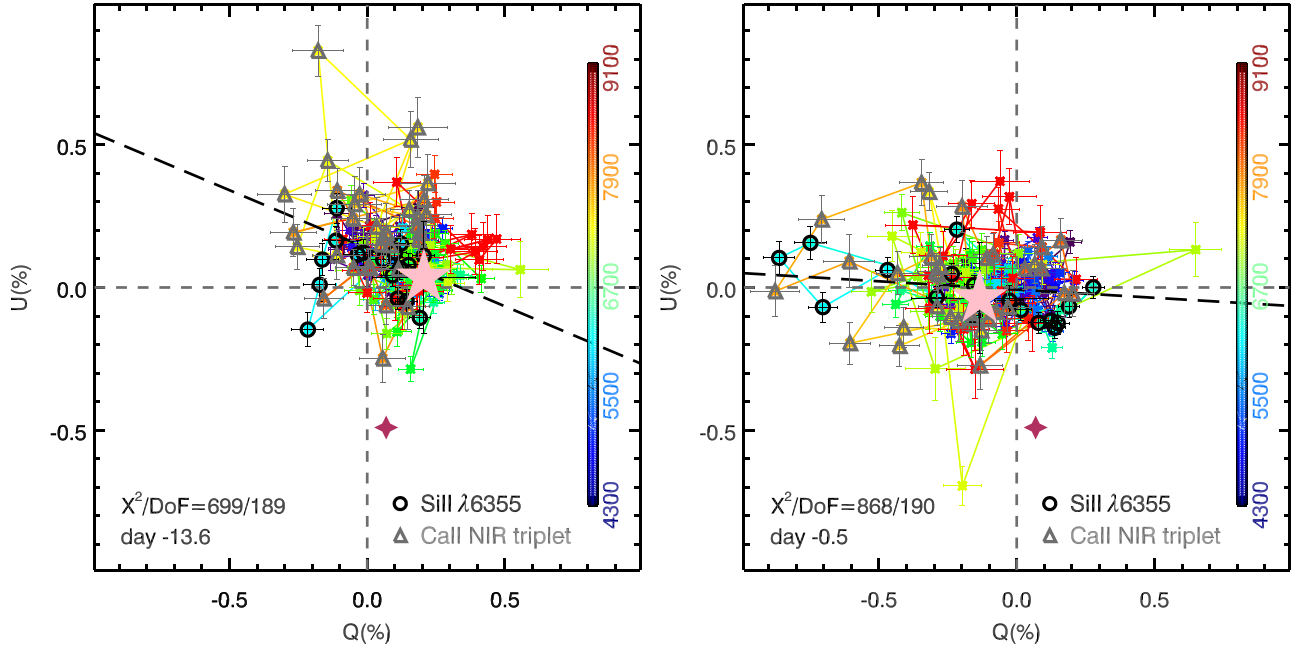
Figure 16. ISP-corrected Stokes parameters of SN 2018gv, on the Stokes Q–U plane. The data have been rebinned to 25 Å. In each panel, the color bar indicates the wavelength and the filled maroon star shows the position of the estimated ISP. The black line traces the dominant axis computed using the data in a wavelength range $4300 \leqslant \lambda \leqslant 9100$ Å. The solid pink ⋆ in each panel indicates the deduced continuum polarization over the wavelength range 6400 to 7200 Å. The open black circles and the open gray triangles mark the spectral regions covering the Si II $\lambda6355$ and the Ca II NIR3 features, respectively.

deviations on the Q–U plane from the dominant axis indicate a significant departure from axial symmetry. In the classification scheme of Wang & Wheeler (2008), the spectropolarimetry of SN 2018gv is an example of spectropolarimetric (SP) Type D1. This type is characterized by data that show an elongated ellipse in a Q–U diagram so that a dominant axis can be identified, but for which a straight line does not provide a satisfactory fit. Significant deviations are found orthogonal to the dominant axis.

5.3. Continuum Polarization

Linear polarization in the continuous spectrum is due to the Thomson scattering of free electrons, and it is independent of wavelength. After correcting for the ISP, the continuum polarization of SN 2018gv at the two epochs was estimated based on the Stokes parameters over the wavelength range 6400–7200 Å, which is known to be free of strongly polarized lines (Patat et al. 2009). Scattering in the degrees of polarization can still be seen within the selected polarized lines-free wavelength ranges that were used to estimate the continuum polarization. Such fluctuation arises from the bound-bound transitions, primarily of iron-peak elements, which modify the emergent radiation by depolarizing the continuum flux and produce some line polarization (Hoeflich et al. 1996; Höflich et al. 2006). The error-weighted mean across this region at the two epochs gives $Q_{Cont1} = 0.20\% \pm 0.08\%$, $U_{Cont1} = 0.04\% \pm 0.09\%$, and $Q_{Cont2} = -0.13\% \pm 0.13\%$, $U_{Cont2} = -0.04\% \pm 0.09\%$, respectively. The error has been estimated by adding the statistical uncertainties and the standard deviation calculated from the 25 Å binned spectra within the continuum wavelength range in quadrature. At epoch 1, the level of continuum polarization of SN 2018gv is consistent with the low levels of continuum polarization measured from SNe Ia at early epochs— that is, $0.06\% \pm 0.12\%$ at day -11 for SN 2012fr (Maund et al. 2013), and $\sim0.3\%$ at -9.1 days for SN 2016coj without the

removal of ISP (Zheng et al. 2017). At epoch 2, a difference of $\Delta Q_{Cont} = -0.33\% \pm 0.15\%$ and $\Delta U_{Cont} = -0.08\% \pm 0.13\%$ can be identified. This marks the time evolution of the degree and the position angle of the continuum polarization— that is, from $p_{Cont1} = 0.20\% \pm 0.08\%$, and $PA_{Cont1} = 4°.8 \pm 11°.3$, to $p_{Cont2} = 0.14\% \pm 0.13\%$ and $PA_{Cont2} = -82°.4 \pm 27°.2$, respectively. At both epochs, the measured degrees of continuum polarization are consistent with the low levels typically measured for SNe Ia (Wang & Wheeler 2008), indicating an approximately spherical symmetry.

5.4. Line Polarization

In addition to the wavelength-independent continuum polarization arising from a globally axisymmetric ejecta, we observe wavelength-dependent polarization features associated with spectral lines at both epochs, in association with spectral lines identified in the Stokes I flux spectrum. This indicates a departure from axisymmetry. The most likely interpretation of line polarization in the context of SNe Ia gives that the underlying electron-scattering photosphere is covered by certain element-rich clumps with high optical depth. These indicate additional asymmetries that are dependent on the chemical composition, ionization, and velocity structure of the ejecta, exterior to the photosphere. Different elements may have different electron-scattering opacities, as well as different geometric distributions. Polarimetry measures the degree of incomplete cancellation of photon "E-vectors" as the photons interact with line transitions in possibly asymmetrically distributed material.

For prominent, broad lines, the polarization profile over wavelength probes the structure of the ejecta in velocity space. For complex structures, which depart from a simple axial symmetry, the resulting polarization across the wavelengths associated with particular spectral features, may deviate from the straight line which is the tracer of axial deviation from
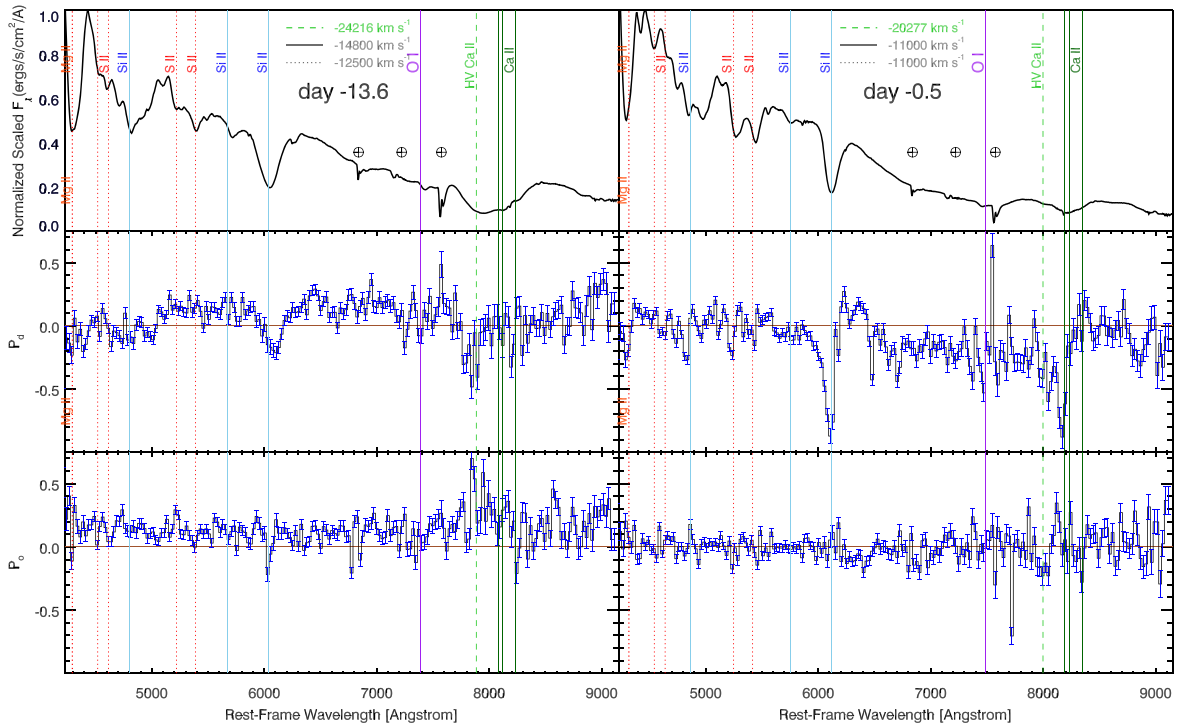
Figure 17. Normalized flux spectra together with the PCA of SN 2018gv spectropolarimetry at −13.6 days (epoch 1, left panels) and −0.5 day (epoch 2, right panels). The top row gives the flux spectra normalized to the maximum value within the range. The middle and the bottom rows illustrate the polarization spectra projected onto the dominant axis and the orthogonal axis, respectively. The vertical solid lines mark the positions of certain spectral features at different velocities as labeled in the figure. Some major tellurics are labeled by ⊕. At −13.6 days, the Si II λ6355 and the Ca II NIR3 features exhibit similar but not identical deviations from the dominant axis, suggesting that the geometrical structures of Si II, Ca II, and the photosphere are different. No polarization is detected across other weaker lines. At −0.5 day, as shown by the right panels, the Si II λ6355 and the Ca II NIR3 features appear to have the same dominant axis. Over the wavelength range 6400–7200 Å characterizing the continuum polarization, the error-weighted mean of P_O has evolved from 0.109% ± 0.095% to −0.044% ± 0.089% from −13.6 to −0.5 days, indicating a more spherically symmetric geometrical structure of the inner ejecta. Notice that the two epochs are characterized by different position angles of the dominant axis and therefore do not share the same orientation of the photosphere.

spherical symmetry (Wang & Wheeler 2008). The presence of asymmetric structures in the ejecta can be inferred from the observation of loops in the Q–U plane. Such loops are defined as a gradual rotation of the PA as a function of observed wavelength across a spectral line. The SN with loops across spectral lines on the Q–U diagram were assigned SP Type L in Wang & Wheeler (2008). The presence of one or more loops across a specific spectral feature indicates a significant variation in the degree of polarization and the polarization position angle at different velocities (corresponding to different depths into the ejecta; Wang & Wheeler 2008).

5.4.1. Si II Lines

At −13.6 days, the peak around 5900–6200 Å in Q and the troughs at similar wavelengths in the U spectrum can be attributed to the Si II λ6355 line at $v \sim -14,000$ km s^{-1} (see Figure 14). After correcting for the ISP, the degree of polarization across this line did not show any distinguishable features in p (see the black line in Figure 14(d)) but exhibited a difference of ∼90° in PA compared to the continuum (see Figure 14(e)). Such a pattern in the PA over the Si II λ6355 feature indicates that the Si-rich portion of the ejecta is likely to be oriented perpendicular to the principal axis of symmetry of the total ejecta. The line profile at ∼4810 Å can be identified as the blueshifted Si II λλ5041, 5056 doublet that has a similar velocity to Si II λ6355; however, the feature is also blended with a series of iron lines (i.e., Fe II λ4913, 5018, 5169). At −0.5 day, the polarization peak around Si II λ6355 occurs at ∼6100 Å. The central velocity of the feature is measured as

∼−11,000 km s^{-1}. The polarization is the highest at the absorption minimum of this feature. The polarization profile is asymmetric with a sharp drop toward lower velocities.

5.4.2. Ca II NIR Triplet

At −13.6 days, troughs in q and peaks in u are also seen between 7800 and 8300 Å (see Figure 14). Though the observed line profiles of Ca II NIR3 at early phases can be well fit by a double Gaussian function describing a normal and HV components with separate central wavelengths, the polarization spectra (with low levels of S/N) do not exhibit separate features for the HV and photospheric velocity components. One can still identify a "notch" around 7800–7900 Å in Q, accompanied by a "peak" at a similar wavelength in U. These features are associated with the HV Ca II NIR3 at ∼−24,200 km s^{-1}. Less obvious features can be seen within the wavelength region of 8000–8300 Å. These features have velocities similar to that inferred for the photosphere from the Si II λ6355 at ∼−14,000 km s^{-1} and also deviate from the overall spectral ranges in p and PA. After correcting for the ISP, the PA across the Ca II NIR3 shows different values compared to that of either the continuum or the Si II λ6355, indicating the configuration of the Ca-rich ejecta is not identical to the Si II λ6355 line-forming regions and distinct from the photosphere as well. At −0.5 day, the Ca II NIR3 is dominated by the photospheric component at ∼−11,500 km s^{-1}. The HV component is still discernible and located at ∼−20,200 km s^{-1}. The polarization behaviors over the HV regions and the photosphere do not show distinct variation.
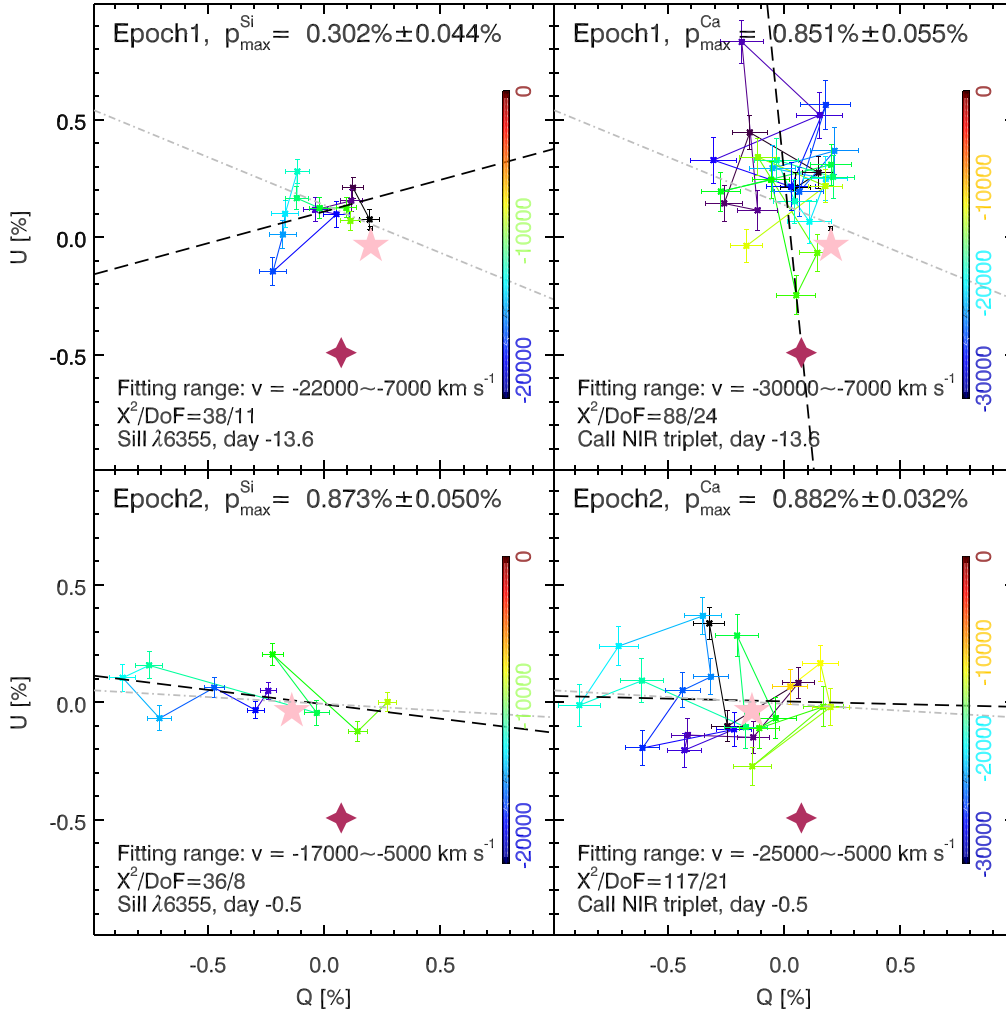
Figure 18. Polarization for the Si II λ6355 (left panels) and the Ca II NIR3 (right panels) features on the Stokes Q–U plane at −13.6 and −0.5 days. The data have been rebinned to 25 Å. In each panel, the points are color-coded according to the velocity relative to the respective wavelengths measured in the rest frame for the two features. The data were corrected for the ISP (the location of which is indicated by the filled maroon star), and the continuum polarization is shown by the solid pink ⋆. The maximum polarization across the feature after ISP correction is also presented. The dashed black line fits the displayed data points, and the dotted gray line traces the dominant axis computed in the wavelength range $4300 \leqslant \lambda \leqslant 9100$ Å.

5.4.3. Mg II λ4481, Si II λ5041, Si II λ5454, 5640, and O I λ7774 Lines

Despite approaching the blue end of spectral coverage, a ~0.3% polarization can be marginally identified with the line of Mg II λ4481 after ISP correction (see Figure 14(d)). Si II λ5041 does not exhibit clear polarization, but the PA across Si II λ5041 and Mg II λ4481 are both larger compared to the PA from 5100 to 7200 Å, except for the Si II λ6355 and telluric features (see Figure 14(e)). This suggests some commonality in their geometry. The same interpretation also holds for epoch 2, in which Mg II λ4481 and Si II λ5041 polarized at ~0.3%–0.4%. At all epochs, the distinctive "W"-shaped S II (λ5454, 5640) absorption features appear at lower velocities compared to the velocity derived from the Si II λ6355 line. For instance, from epoch 1 to epoch 2, the S II λ5454, 5640 velocities evolve from −13,800 km s^{-1} and −13,500 km s^{-1} to −10,100 km s^{-1} and −10,400 km s^{-1}, respectively. The slower velocities measured for S II λ5454, 5640 are due to this feature being optically thin at larger radii compared to Si II and Ca II. This is corroborated by the consistent low polarization measured across this feature, which suggests that sulfur is more concentrated in lower-velocity

regions than calcium and silicon. Additionally, we find that the O I λ7774 line appears to be weak in the flux spectrum, and no sign of that feature can be identified in the polarization spectrum. The primordial oxygen from the WD maintains its initial spherically symmetric distribution despite the asymmetric explosion. This gives an important constraint on the explosion models (Höflich et al. 2006).

5.5. The Inferred Ejecta Geometry

Following from Section 5.2, we present the dominant and the orthogonal polarization components after correcting for ISP in Figure 17. The dominant component—that is, the polarization projected onto the dominant axis—represents global geometric deviations from spherical symmetry. Any polarization signal orthogonal to the dominant axis carries information about deviations from axial symmetry. In Figure 18, we show the loops across the Si II λ6355 and Ca II NIR3 features. At epoch 1, the polarization modulations associated with Si II λ6355 are principally observed in the dominant polarization component P_d (i.e., the middle-left panel in Figure 17). In the orthogonal polarization component (see the bottom-left panel in Figure 17),
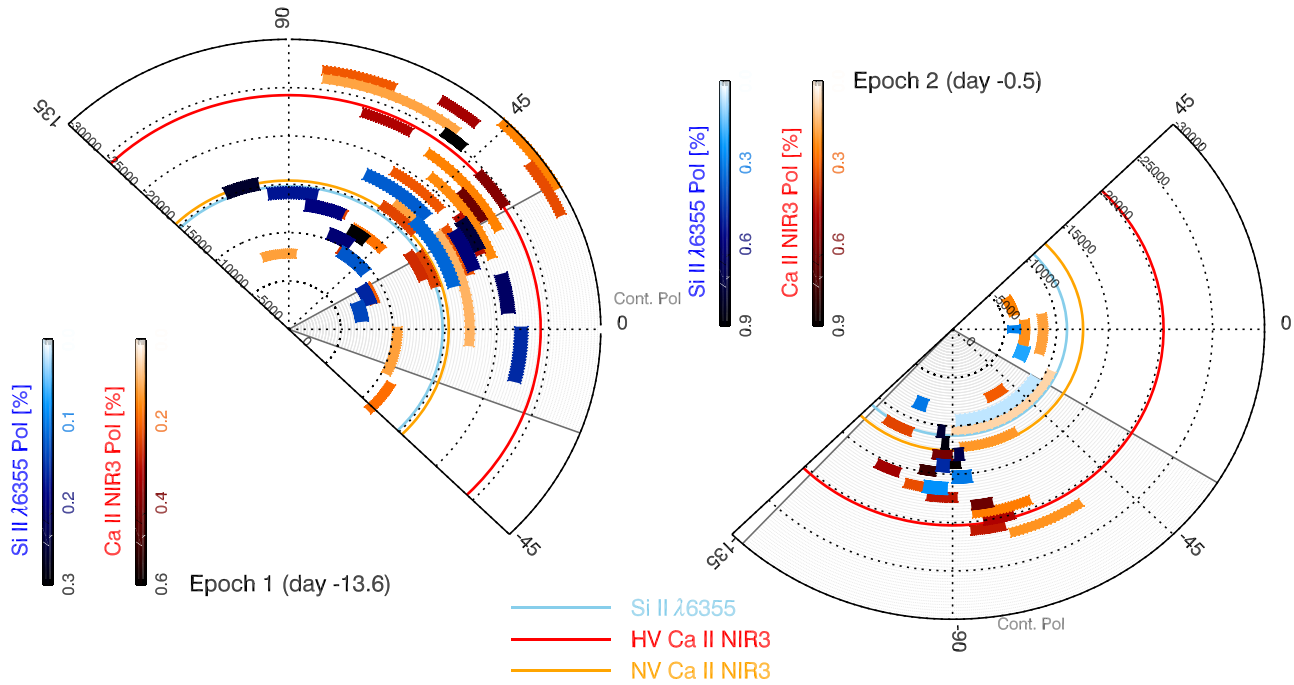
Figure 19. Polar plots of SN 2018gv showing the velocity and polarization angle across the profiles for Si II λ6355 and Ca II NIR3 as a function of radial velocity. In each panel, the color bars indicate the ISP-corrected polarization degrees with the continuum polarization not subtracted. The numbers along the radial and position angle are labeled in km s^{-1} and in degrees, respectively. The data have been rebinned to 25 Å for better visualization. The center and the angular extent of each colored-bin represent the average PA and the associated error, respectively. Note that larger angular extent suggests greater uncertainty on the PA. The continuum polarization angle is shown in gray, and its angular extent indicates the 1σ uncertainty. Typical uncertainties in the data points are smaller in epoch 2 compared with epoch 1, due to higher S/N. Velocities measured at the minima of the flux spectra of each species are indicated by colored semicircles, as labeled.

a narrow polarization profile can be identified at the wavelength coincident with the position of the absorption minima of Si II λ6355. Such a residual indicates that the bulk orientation of Si-rich ejecta is different from that of the dominant axis of the photosphere (as inferred from the continuum polarization). A line complex can be observed in the polarization modulations associated with Ca II NIR3. The HV component shows modulation in both the dominant and the orthogonal polarization components. The NV component, however, exhibits significantly less modulation in both the dominant and orthogonal components.

At epoch 2, the polarization modulations associated with Si II λ6355 and Ca II NIR3 both fall predominantly along the P_d axis. The signal in the orthogonal polarization component, over the observed wavelength range, is consistent with the expected level of uncertainty. The rotation of the PA over Si II λ6355 (i.e., see Figure 18) can be interpreted as the rotation of the principal axis of symmetry with depth into the ejecta. The HV component of Ca II NIR3 has become significantly shallower by epoch 2. Due to insufficient S/N, it is unclear if the HV Ca II NIR3 component carries the same axial asymmetry as other lines. The polarization signal associated with Ca II NIR3 is dominated by the NV component. Moreover, the PA of the Ca II NIR3 are almost aligned with the Si II λ6355 at epoch 2, suggesting that the line-forming regions of silicon and calcium have already settled to a relatively similar geometric configuration.

In epochs 1 and 2 (see Figure 18), the Si II λ6355 and the Ca II NIR3 both exhibit loops in the Q–U space. In epoch 1, linear fittings of Stokes Q–U data points across each line suggest that the Si-rich and the Ca-rich regions reside in different positions of the ejecta, which are also incompatible with the global geometry indicated by fitting all the data points across the entire observed wavelength. In epoch 2, the data

points across the Si-rich and the Ca-rich ejecta tend to fall along a single locus. The orientation of these ejecta is also consistent with the overall shape of the ejecta.

The geometry of the Si-rich and the Ca-rich ejecta can also be visualized in polar plots (e.g., see Maund et al. 2009; Reilly et al. 2016; Hoeflich et al. 2017; Stevance et al. 2019). Such plots present the position angles measured for selected spectral features at different radial velocities in polar coordinates. Figure 19 depicts polar plots for the Si II λ6355 and the Ca II NIR3 profiles at both epochs. At epoch 1 (−13.6 days, left panel), the large offset in the radial profile of Si II λ6355 (shown in blue) compared to the total ejecta (the gray sector) confirms the large deviations from the dominant axis of the continuum polarization. The even more erratic radial profile of the Ca-rich component also indicates a complex structure of the line-forming regions. At epoch 2 (−0.5 day, right panel), the change in the position angle of the continuum polarization (see Section 5.3) can be seen as the rotation of the gray-shaded sector. The radial profiles of both the Si-rich and the Ca-rich components have settled to a similar orientation as the total ejecta indicated by the gray sector.

6. Discussion of the Spectropolarimetry Observations

6.1. The Si II λ6355 Polarization Compared with a Larger Sample

First, we notice that the polarization of Si II on the Q–U diagram can be well fitted by a straight line (e.g., see the right panel of Figure 16 and the lower-left panel of Figure 18). With a clearly defined dominate axis, SN 2018gv would thus be classified as SP Type D0 (Wang & Wheeler 2008). Such a significantly polarized Si II feature is suggestive of a global asymmetry of silicon layer.

The peak polarization across the Si II $\lambda6355$ line evolves with time. In order to compare with different SNe at similar phases, Wang et al. (2007) fitted the data with a second-order polynomial to describe the time dependence of the degree of the Si II polarization: $p_{\mathrm{Si\,II}}(t) = 0.65 - 0.041(t-5) - 0.013(t+5)^2$. Here t denotes the time (in days) after the B-band maximum light and $p_{\mathrm{Si\,II}}(t)$ gives the measured polarization (in percent) of Si II $\lambda6355$. Wang et al. (2007) derived a correlation between the maximum line polarization of Si II $\lambda6355$ and Δm_{15} (B):

$$p_{\mathrm{Si\,II}}^{\mathrm{corr}-5} = 0.48(03) + 1.33(15)(\Delta m_{15} - 1.1), \qquad (9)$$

where $p_{\mathrm{Si\,II}}^{\mathrm{corr}-5}$ is defined as the polarization of the Si II $\lambda6355$ corrected to -5 days in a unit of percent. This correlation indicates that at a given epoch, dimmer SNe exhibit higher Si line polarization and hence higher chemical nonuniformity. This can be understood if the dimmer the SN, the less material was burnt. Such an incomplete burning is not sufficient to erase chemically lumpy configurations. The quantity $p_{\mathrm{Si\,II}}^{\mathrm{corr}-5}$ can be obtained by applying the correction given by Wang et al. (2007):

$$P_{\mathrm{Si\,II}}(t) = P_{\mathrm{Si\,II}}^{\mathrm{corr}-5} - 0.041(t-5) - 0.013(t+5)^2. \quad (10)$$

For SN 2018gv, adopting $p_{\mathrm{Si\,II}}(t) = 0.87\% \pm 0.05\%$ at $t = -0.5$ day gives $p_{\mathrm{Si\,II}}^{\mathrm{corr}-5} = 0.91\% \pm 0.05\%$. This is significantly larger than the typical 1σ upper range of polarization shown as Figure 2 of Wang et al. (2007).

Such a significant discrepancy does not necessarily mean that SN 2018gv has a peculiar Si II $\lambda6355$ polarization because the empirical relationship proposed by Wang et al. (2007) does not account for the considerable intrinsic polarization variations from SN to SN. The high degree of polarization observed for SN 2018gv suggests the presence of large-scale departure from spherical symmetry. Cikota et al. (2019) reanalyzed this relationship using a larger sample of 35 SNe Ia and found a significantly larger scatter. The observed degree of silicon polarization of SN 2018gv at -0.5 day falls in the $\sim0.1\%$–1.7% range determined from a larger sample. Future high-precision spectropolarimetry of more SNe Ia with complete coverage of the rising phase is essential to determine the commonality and probe the intrinsic diversity in the geometric structure of the ejecta.

According to Maund et al. (2010), the peak polarization degree of the Si II $\lambda6355$ line at -5 days is correlated with the average daily decline rate of the expansion velocity measured from the same line:

$$P_{\mathrm{Si\,II}}^{\mathrm{corr}-5} = 0.267 + 0.006 \times \dot{v}_{\mathrm{Si\,II}}. \qquad (11)$$

The velocity gradients were derived based on the measurements taken between maximum and approximately 2 weeks after, when the Si II feature disappears (Benetti et al. 2005), while the corrected day -5 Si II polarizations were obtained based on Equation (10). Adopting the velocity gradient of SN 2018gv around the peak or between days 0 to $+10$ (i.e., $\dot{v}_{\mathrm{Si\,II}} = 36.6 \pm 6.4\,\mathrm{km\ s^{-1}}$ or $34.3\,\mathrm{km\ s^{-1}}$), the estimated polarization gives $p_{\mathrm{Si\,II}} = 0.49\% \pm 0.04\%$ or 0.47%, respectively. These values are lower compared to the determined $p_{\mathrm{Si\,II}}^{\mathrm{corr}-5}$.

Cikota et al. (2019) explored the possible correlations among the polarimetric and other observational properties of SNe Ia.

Based on an archival data sample of 23 SNe that have at least one observation between day -11.0 and day 1.0, they found a strong linear correlation between the Si II $\lambda6355$ polarization and the expansion velocity traced by the same line:

$$P_{\mathrm{Si\,II}} = (6.40 \pm 1.28) \times 10^{-5} \times v_{\mathrm{Si\,II@}-5\mathrm{d}}$$
$$- (0.484 \pm 0.147), \qquad (12)$$

where $p_{\mathrm{Si\,II}}$ is the maximum polarization of the Si II $\lambda6355$ line between day -11 and $+1$, and $v_{\mathrm{Si\,II@}-5\mathrm{d}}$ gives the velocity measured from the Si II $\lambda6355$ profile at -5 days relative to the B-band peak brightness. Adopting an interpolated $v_{\mathrm{Si\,II@}-5\mathrm{d}} = -11,300\,\mathrm{km\ s^{-1}}$ at day -5 and a typical uncertainty of $27\,\mathrm{km\ s^{-1}}$, Equation (12) yields a maximum Si II $\lambda6355$ polarization of $0.24\% \pm 0.21\%$. Therefore, we conclude that SN 2018gv is consistent with the Si II velocity-polarization relationship at day -13.6 ($p_{\mathrm{Si\,II}} = 0.30\% \pm 0.04\%$) but exhibits a significantly higher Si II $\lambda6355$ polarization at day -0.5 ($p_{\mathrm{Si\,II}} = 0.87\% \pm 0.05\%$).

6.2. The Asymmetric Polarization Profile of Si II $\lambda6355$

We notice that the most prominent Si II $\lambda6355$ feature in the polarization spectrum around the $B-$maximum exhibits an asymmetric profile. Figure 20 portrays the polarization profiles of Si II $\lambda6355$ and Ca II NIR3 at day -0.5 with an 8 Å bin size. In Figure 20(d1), one can see that the polarization signal across the Si II $\lambda6355$ feature declines gradually from the absorption minimum in the flux spectrum toward shorter wavelengths. In contrast, the polarization profile exhibits a sharp drop from its peak toward longer wavelengths. We roughly estimated the blue side of the wing ranges from 5950 to 6120 Å, and the red side covers 6120–6170 Å, corresponding to $-19,100$ to $-11,100\,\mathrm{km\ s^{-1}}$ and $-11,100$ to $-8700\,\mathrm{km\ s^{-1}}$ in velocity space, respectively. Considering the Si II $\lambda6355$ velocity measured from the same spectrum as $-10,984 \pm 345\,\mathrm{km\ s^{-1}}$, the velocity range measured from the polarized spectrum gives -8100 to $+2400\,\mathrm{km\ s^{-1}}$ relative to the SN photosphere velocity traced by the same line. Such an asymmetric profile was not identified at epoch 1. The Ca II NIR3 displays a complex polarization profile. At epoch 2, a weaker separate peak over ~8020–8080 Å (see Figure 20(d2)) can be identified between the HV and NV Ca components, corresponding to a radial velocity of $\sim-18,000\,\mathrm{km\ s^{-1}}$. Without a finer temporal sampling of the spectropolarimetric evolution, it is not clear whether this component could be the analog of the asymmetry observed in Si II $\lambda6355$.

Around maximum light, the broad and symmetric flux profile across the Si II $\lambda6355$ feature suggests the absence of a distinct chemical "boundary layer" at any drastically different velocities. Therefore, the sharp cutoff in the corresponding polarization profile at the low-velocity end can be attributed to the presence of a separate Si-rich component at a slightly higher velocity. It may be indicative of Si-rich matter at lower velocity and with similar geometry as the Thomson-scattering photosphere. The apparent asymmetry of the HV components of the Si-rich ejecta is consistent with an off-center delayed detonation. Such an asymmetric explosion would compress the core more significantly toward the direction away from the center, therefore pushing the intermediate-mass elements and developing the asymmetric HV components (e.g., see Section 4.3 of Fink et al. 2010 and Figure 1 of Bulla et al. 2016a). The absence of a similar structure at the first epoch would imply that the asymmetry becomes visible as more inner
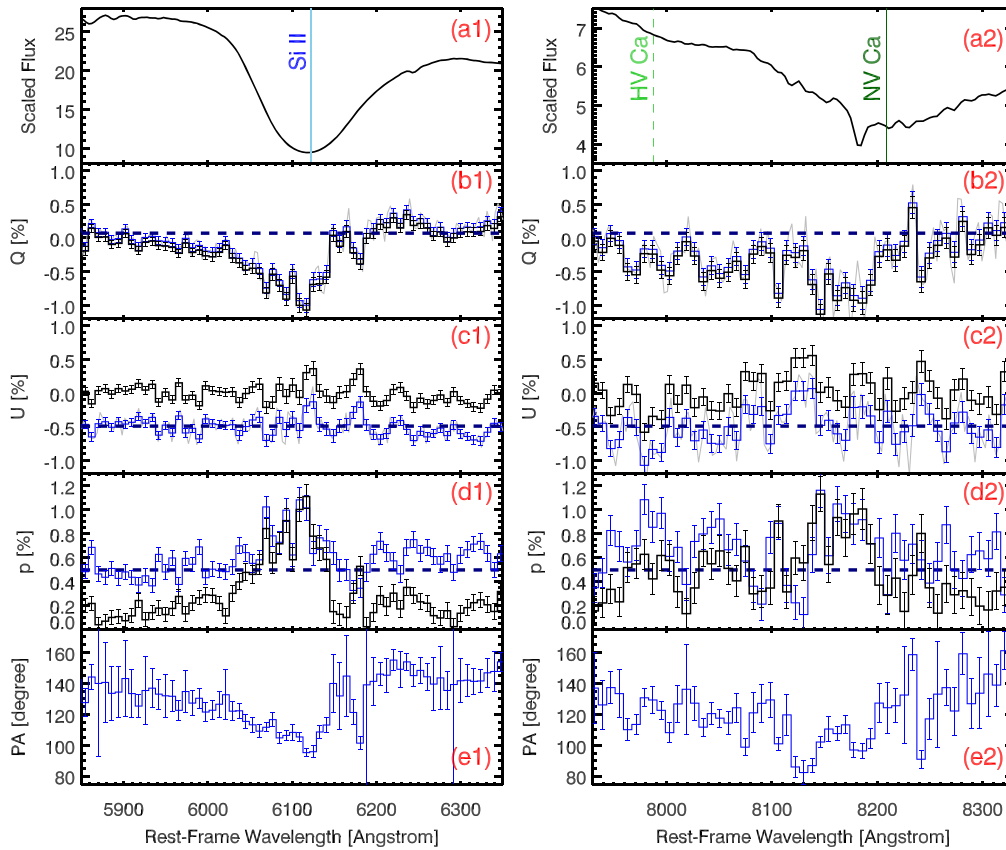
Figure 20. Same as Figure 15, but on the spectroplarimetry of SN 2018gv across Si II λ6355 (the left panels) and the Ca II NIR3 (the right panels) at day −0.5 (epoch 2). The data have been rebinned to 8 Å. In the left panels (i.e., d1), the Si II polarization declines much faster from its peak around ∼6200 Å ($v \sim -11{,}000$ km s^{-1}) toward longer wavelengths compared to shorter wavelengths. Multiple peaks around ∼6100 Å may indicate the presence of various Si-rich components, which were not identified in the flux spectrum.

parts of the WD are exposed. This seems consistent with an off-center delayed detonation.

We suggest that the width of the wing toward the lower velocities characterizes the scale height of the Si-rich ejecta above the photosphere. Such an asymmetric polarization profile may not necessarily be a ubiquitous phenomenon since ignition of detonation at small off-center distances would lead to a relatively uniform distribution of silicon (see Höflich et al. 2002, 2006). A slightly off-centered detonation leads to a relatively uniform distribution of the elements synthesized near the central region. The velocity spread is, therefore, smaller so that there would be no splitting into NV and HV components of Si II λ6355. This is in agreement with the study based on larger samples (Silverman et al. 2015). For example, HV features of Si II λ6355 are seen in only ∼one-third of the SNe Ia, even at early times ($t < -5$ days). Such HV features tend to appear at the earliest phases and in objects with large photospheric velocities (Silverman et al. 2015). By contrast, HV features of Ca II NIR3 are observed in ∼91% of the SNe Ia with spectra obtained earlier than day −4 (Silverman et al. 2015). Spectro-polarimetry of a solid sample would deliver an alternative method of identifying and resolving the different components in the ejecta, which often are ambiguous in flux spectra. At earlier phases, the absence of such asymmetry would suggest that the Si-rich ejecta are well above the photosphere. A gradually changing polarization profile toward the higher velocities may imply that the outer part of the Si-rich ejecta has already developed a diffuse structure above the photosphere. If indeed the polarized Ca-rich component at

∼8020–8080 Å (∼−18,000 km s^{-1}) is related to the asymmetric polarization profile of Si II λ6355, it could be interpreted as an HV Ca-rich layer in the ejecta formed further out relative to the Si-rich layers. This is corroborated by the higher velocities measured across the NV Ca II NIR3 feature.

6.3. Implications of the Polarization and Different Models

We compare the polarization of SN 2018gv to simulations by Bulla et al. (2016a, 2016b), who calculated polarization spectra for different SN Ia explosion models at various equatorial viewing angles and off-center delayed-detonation models with various off-center points for a delayed-detonation model for a normal-bright SNe (Höflich et al. 2006). The low continuum and line polarizations as early as day −13.6 contradicts the high polarization levels of violent merger models (Pakmor et al. 2012; Bulla et al. 2016b). The observed low continuum, the moderate levels of Si II and Ca II NIR3 line polarizations, and the low polarization of O I λ7774 lead us to consider that SN 2018gv is broadly consistent with the overall geometric properties predicted by off-centered delayed-detonation models (i.e., Seitenzahl et al. 2013; Bulla et al. 2016a) and sub-M_{Ch} double-detonation models (i.e., Fink et al. 2010; Bulla et al. 2016a).

Regardless of the presence of HV Si II wing, which is unresolved in the flux spectra, the observed pre- and near-maximum-light polarization properties of SN 2018gv are similar to those of other normal SNe Ia—that is, SNe 1996X (Wang et al. 1997), 2001el (Wang et al. 2003a), 2004dt
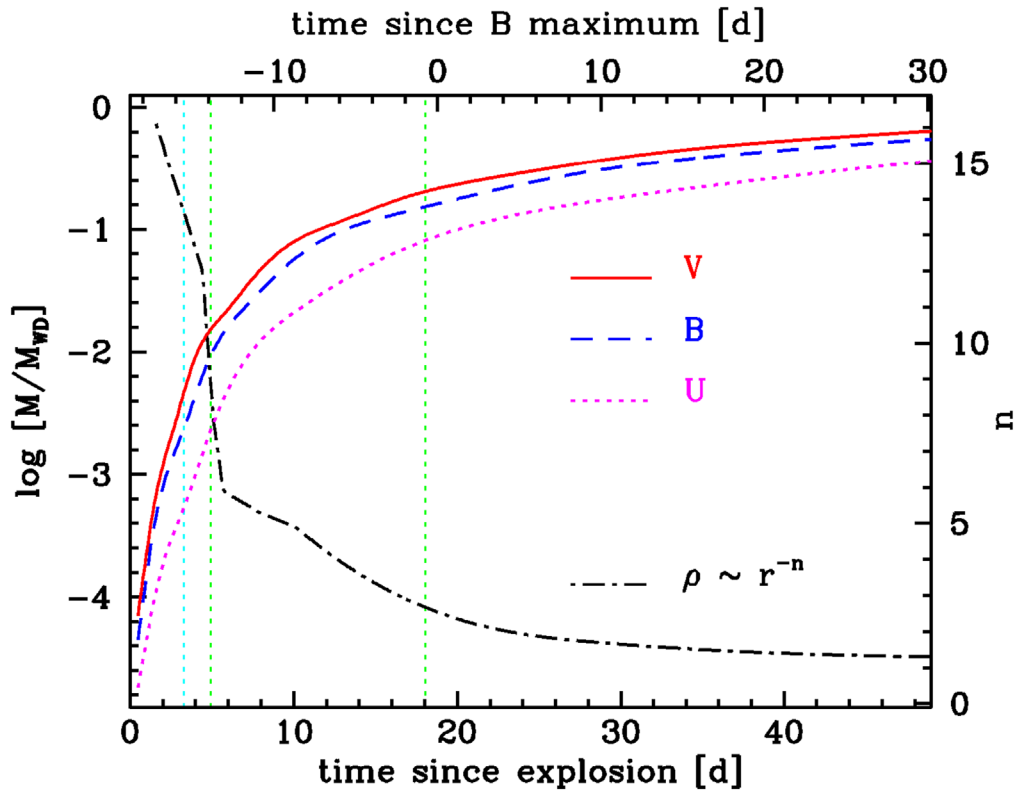
Figure 21. Mass above the photosphere as a function of time for the normal-bright delayed-detonation model 27 (Hoeflich et al. 2017). In addition, we give exponent n, which approximates the density structure at the photosphere in B and V. The vertical lines at 3.3, 4.9, and 18.0 days since the explosion mark the times with the first flux (cyan) and the polarization spectra (green), respectively. The uncertainty in the phase are ≈ 0.92 day corresponding. In the V-band range, we probe the outer $(0.3–1) \times 10^{-2} M_\odot$, $(1–3) \times 10^{-2} M_\odot$, and $0.2–0.3 M_\odot$, respectively.

(Wang et al. 2006), 2006X (Patat et al. 2009), 2011fe (Milne et al. 2017), 2012fr (Maund et al. 2013), 2014J (Porter et al. 2016), and 2016coj (Zheng et al. 2017). Kasen et al. (2003) presented models of SN 2001el and provided a comprehensive parameterization for several possible configurations of the HV Ca II loop. The complex Ca II loop profile observed from SN 2018gv could be interpreted as multiple clumped shells or a superposition of multiple clumped shells with a characteristic ellipsoidal shell. More work is needed to account for the formation of such a complex HV polarization feature and its different orientation from the photosphere.

Additionally, comparing SN 2018gv to the simulations of Bulla et al. (2016a), we infer that the relatively high line polarization of SN 2018gv around the peak (i.e., ~0.87% ± 0.05%) does not favor a large number of ignition kernels in delayed-detonation models (Seitenzahl et al. 2013). A large number of ignition kernels (i.e., $N > 100$) would lead to a more symmetric distribution of intermediate-mass elements and thus produce a generally lower degree of line polarization. More theoretical modeling is needed to account for the HV features observed in Si II $\lambda 6355$ and Ca II NIR3 lines and to investigate the shape and time-evolution of the flux and polarized spectra (Mulligan & Wheeler 2018).

In the following and guided by the flux spectra, we discuss the polarization characteristics of SN 2018gv in terms of off-center delayed detonations (Höflich et al. 2006) that are based on spherical delayed-detonation models for the deflagration phase (Hoeflich et al. 2017). In addition, we perturb the underlying structure to use the observed polarization to identify and quantify the underlying aspherical components—namely asymmetry in density and abundances. The treatment of the

asymmetries as perturbation is justified because, overall, they are small. We use spherical models as baseline because they suppress deflagration mixing, a requirement from the discussion herein and many observations from other research (Höflich & Stein 2002; Fesen et al. 2007; Diamond et al. 2015, and references therein). Possible reasons may include the effect of high-magnetic fields as indicated by late-time light curves, near mid-IR spectra (Penney & Hoeflich 2014; Remming & Khokhlov 2014; Hristov et al. 2018). We choose deflagration to detonation transition (DDT) models for normal-bright SNe Ia because the photometric characteristics of SN 2018gv are very similar to the observations of the light curves, color curves, and color–magnitude diagrams, as shown and discussed in Section 3. As a baseline-model, we use model 27 with the velocity, density, and abundance distribution given in Figures 1 and 2 of Hoeflich et al. (2017). Model 27 has a rise time of 18.8 days and $\Delta m_{15}(B/V) = 0.62/0.98$ mag compared to 18.51 ± 0.92 days and $0.63/0.96$ mag of SN 2018gv.

In Figure 21, we show the mass above the photosphere as a function of time and the corresponding density slope n for $\rho \propto r^{-n}$ of the delayed-detonation model cited previously. Note that the overall structures are rather similar for a wide range of models, including sub-M_{Ch}, but the mass fraction scales with the total mass.

As discussed in previous sections, SN 2018gv shows many characteristics of model 27. First, we see little C II and O I early on corresponding to the outer layers at $\approx 5 \times 10^{-3} M_\odot$. Second, line wings of Si II $\lambda 6355$ extend to the very outer layers (i.e., $>23,000$ km s^{-1}) and evolve smoothly with time, which starts at about $3 \times 10^{-3} M_\odot$ in the wings, and the Si II line extends down to about $0.3–0.4 M_\odot$ from the outside. We note that this

early start and such a large, continuous range for Si is barely compatible with double-detonations of a sub-M_{Ch} mass WD, which would require at least 2×10^{-2} and $3 \times 10^{-3} M_{\odot}$ for a WD with 0.6 and $1.2 M_{\odot}$, respectively (Shen & Moore 2014). The long, logarithmic decline of the Si abundances until close to the surface is inherent to detonations going through C/O matter in M_{Ch} mass models. It also leads to the inverted-triangular-shaped Si line wings (∇) visible until about -13.2 days in Figure 8, corresponding to a photospheric velocity of $\approx 15{,}000$ km s^{-1}, which, in the model, marks the transition to the Si/S dominated layers in the envelope. A linear line wing is a consequence of the logarithmic decline of the Si abundance, combined with low optical depth (Quimby et al. 2007).

Based on the delayed-detonation model, we want to discuss the polarization of SN 2018gv in terms of parameterized asphericity. Polarization can be formed by (i) aspherical density distributions (van de Hulst 1957; Höflich 1991), (ii) partial obscuration of the underlying Thomson-scattering dominated photosphere by line-absorption (Höflich et al. 2006; Kasen et al. 2006), and (iii) off-center energy sources (Chugai 1992; Hoeflich et al. 1995). SN 2018gv does not show a flip in the polarization angle, and thus this case is not applicable.

We first want to consider asymmetric chemical distributions produced by off-center DDT models in which the axis of chemical asymmetry is given by the center of the density distribution and the point of the DDT. The polarization of SN 2018gv can be understood in very similar terms as SN 2004dt—a normal-bright SN Ia but with a slightly steeper decline rate (i.e., $\Delta m_B (15) = 1.13 \pm 0.04$ mag; Wang et al. 2012). At about 1 week before maximum, the polarization in SN 2004dt was high in Si II lines but weak in Mg II without showing O I polarization (Höflich et al. 2006; Wang et al. 2006). The observation was reproduced by an off-center DDT model seen from $30°$ relative to the axis of symmetry. At this phase, the photosphere passes the interface between explosive carbon and incomplete silicon burning. It could be understood in terms of covering the underlying scattering photosphere by optically thick lines, in combination with the chemical gradients. Namely, all strong Si II lines show similar polarization because both are optically thick at this phase; the magnesium polarization is formed in a thin shell produced by explosive carbon burning. Oxygen shows little polarization because, in a C/O WD, in explosive carbon, burning increases O to about 70%, but the contrast is too small, with the unburned C/O layers at about 50%.

Similarly, SN 2018gv shows no O I polarization because there is no abundance jump in oxygen in the line-forming region at -13.6 and -0.5 day. The Si II $\lambda 6355$ line shows little polarization at -13.6 days because the line is partially optically thin, as discussed previously and indicated by the linear blue line wings. Thus there is little asymmetric covering of the underlying photosphere. By -0.5 day, the underlying has entered the Si/S-rich region resulting p of about 0.8%. Compare this to SN 2004dt, with $p(\text{Si ii}) = 1.8\%$ (Höflich et al. 2006; Wang et al. 2006). The line polarization may lower because, for the higher luminosity of SN 2018gv, the Si region is shifted toward lower density and lower optical depth, at a different phase, or we may see the object from a slightly larger inclination. The first effect likely is important because the flux in the blue wing of the Si II line is hardly polarized. Future
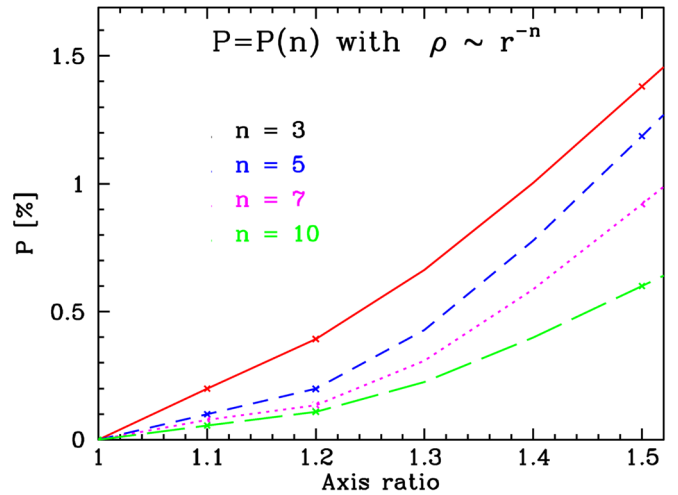
Figure 22. Continuum polarization as a function of asymmetry in a scattering dominated frequency range formed in the region of intermediate-mass elements. We assume an oblate ellipsoid with an axis ratio of A/B and depolarization at a Thomson optical depth of 5.

dense series of earlier-phase spectropolarimetry will allow for a separation of the effects.

Now, we want to shift toward the continuum polarization that, early on, can be understood in terms of an asymmetric density/electron distribution. The low continuum polarization observed gives important limits on the overall asymmetry. During the phase considered, the photosphere is formed in the C/O/Mg/Si/S layers, and the ionization fraction hardly changes because of similar ionization potentials of the main electron donors. As a result, the electron distribution at the photosphere can be approximated by the density distribution. The polarization depends on the density structure and decreases with steeper density slopes because the incoming radiation at the photosphere becomes more isotropic.

In Figure 22, we give the polarization seen equator-on for oblate ellipsoids with an axis ratio of A/B for various density slopes n for structures realized in models. For SN 2018gv, the continuum polarization is $0.20\% \pm 0.13\%$ and $0.15\% \pm 0.16\%$ at about -13.6 days and maximum light, respectively. The outer $(1–2) \times 10^{-2} M_{\odot}$ are aspherical, with a well-defined axis because of the constant polarization angle. The size of asymmetry is about 10%–35% when seen equator-on. We see significant asymmetry early on. By maximum light, p declined, and it is consistent with no polarization. The size of asymmetry is between 0% and 15%. Note that p goes roughly as $\propto \sin^2(\Theta)$, but due to multiple scattering effects, the change of p becomes less steep (Höflich 1991).

It is beyond the scope of this paper to engage in a full analysis, but we would like to put SN 2018gv into the context of a different mechanism for producing asymmetry. First, dynamical or head-on collisions of WD show larger asymmetries and can be ruled out because they predict larger asymmetries in the inner layers or off-center energy sources (Benz et al. 1990; Pakmor et al. 2011; Katz et al. 2016; Sato et al. 2016; García-Berro & Lorén-Aguilar 2017; García-Berro et al. 2017). Second, rapidly rotating WDs close to M_{Ch} produce asymmetric initial configuration and are consistent with the polarization seen in this object (Eriguchi & Mueller 1993; Yoshida 2019); He-triggered detonations do produce strong asymmetries in the outer layers and, consistent with SN 2018gv, show almost spherical inner

layers (Shen & Moore 2014). One problem, though, may be that the early observations place the photosphere into He-rich layers, and its burning products for all but WDs at the upper end of the masses are seen as possible. Both the flux and polarization spectra indicate no "double-chemical" structure of Si/S, starting within the outer $3 \times 10^{-3} M_\odot$. The lack of O I polarization puts an even stronger limit on a He layer atop $10^{-2} M_\odot$.

Though the picture of a rotating WD within the off-center delayed-detonation scenario seems to be consistent, we need earlier observations and denser series of spectroplarimetry obtained than obtained for SN 2018gv.

7. Summary

We present extensive UV and optical photometry, optical spectroscopy, as well as optical linear spectropolarimetry of SN 2018gv. We are able to draw the following conclusions:

(1) The rising light curve is consistent with a power-law exponent $[f(t) \propto (t - t_0)^n]$. Our fitting to the early g'-band light curve yields a rise time of $\sim$18 days and an index of $n \sim 2$.

(2) We adopt the "CMAGIC" method and estimate the host-galaxy reddening toward SN 2018gv to be negligible [i.e., $E(B - V)_{\rm host} = 0.028 \pm 0.027$ mag].

(3) The light curves show that SN 2018gv is a normal SN Ia with a typical B-band peak magnitude of -19.06 ± 0.05 and a luminosity decline rate $\Delta m_{15}(B) = 0.96 \pm 0.05$ in the rest frame.

(4) The comprehensive photometry allows us to construct the UV-optical pseudo-bolometric light curve of SN 2018gv in the 1660–8180 Å range. The bolometric luminosities are estimated after further correcting for the fraction of the NIR flux. The maximum bolometric luminosity gives $L = (1.186 \pm 0.064 \pm 0.022) \times 10^{43}$ erg s^{-1}, yielding a synthesized nickel mass of $0.56 \pm 0.08 M_\odot$.

(5) The early-time spectra of SN 2018gv exhibit strong similarity to those of the normal Type Ia SN 2011fe in most respects. No significant HV component is detected in the Si II λ6355 absorption feature, as early as -15.2 days relative to the B-band maximum. Strong HV features are unambiguously detected in Ca II NIR3 features. At velocities from $-27,000$ to $-20,000$ km s^{-1}, they are detached from the photosphere.

(6) The earliest spectropolarimetry to date of an SN Ia at day -13.6 has been obtained for SN 2018gv. The degree of continuum polarization is as low as $\sim$0.2%. The observation of low continuum polarization overlaid by significant line polarization is inconsistent with the double-degenerate violent merger case but consistent with the single-degenerate delayed-detonation and double-detonation models.

(7) An asymmetric polarization profile of the Si II λ6355 feature around the light-curve peak has been observed. The very strong polarization at line center implies a sharp increase of the opacity gradient in the direction transverse to the line of sight as the photosphere recedes to the interface layer of Fe and IME. The sharp drop of polarization toward lower velocities suggests the presence of a distinct chemical "boundary layer," while the slow decline of polarization toward higher velocities indicates the formation of a rather diffuse and homogeneous ejecta profile above the photosphere.

(8) The flux and polarization spectra are consistent with classical off-center delayed-detonation transitions with $M_{\rm Ch}$ mass WDs but originating from a rapidly rotating WD. However, our observations are insufficient to address a possible alignment of the symmetry axes in density and abundances. Double-detonation models would require masses close to $1.2 M_\odot$.

(9) Such an asymmetric Si II λ6355 polarization profile around the SN peak luminosity may indicate that in opposite directions from the stellar center, IMEs were produced over different distances. This is consistent with an off-center delayed detonation.

To our knowledge, only two SNe Ia have spectropolarimetric geometric probes within 5 days after the explosion. The low continuum polarization at $\sim$5 days (0.2% for SN 2018gv; this work) and $\sim$4 days (0.5% for SN 2019np; P. Hoeflich et al. 2020, in preparation) indicates a rather spherical photosphere that is inconsistent with violent DD mergers. However, even after as little as 4 days, the expanding photosphere has already engulfed and left far behind the companion whose nature thus remains unconstrained. Future spectropolarimetry starting from the earliest possible phases will probe any polarization signals in the continuum and across the prominent spectral features. The continuum polarization may nevertheless be low since scattering may be weak in a thin photosphere at early epochs. Highly polarized high-velocity features at early epochs would give strong clues to the symmetry of the explosion. Such data will also enrich the current sparse sample and test aspect-angle dependency and uniformities of SNe Ia observations. More detailed theoretical modeling to the early spectropolarimetric properties of SNe Ia will be discussed in a separate paper (P. Hoeflich et al. 2020, in preparation).

Taken together, our observations suggest that SN 2018gv resembles other normal SNe Ia in many respects. The polarimetry of infant SNe (SNe discovered within 1–2 days after their explosion) provides an important probe of the kinematics and chemical structures of SNe and their circumstellar environment during the final stages of the progenitor evolution. Wide-field, high-cadence transient surveys, such as the Zwicky Transient Facility (Bellm et al. 2019), ATLAS (Tonry 2011), ASAS-SN (Shappee et al. 2014), and DLT40 (Tartaglia et al. 2018), will discover and monitor nearby infant SNe over the next few years. A large polarimetry sample of such objects will enable stringent constraints on the explosion mechanisms and the circumstellar environment of SNe Ia.

Appendix A
VLT Spectropolarimetry Reduction

All VLT spectropolarimetric observations were conducted with the 300V grism coupled to a $1''$ slit. The high-pass was chosen to stop second-order light, from the flux at $\lambda \lesssim 4400$ Å, contaminating the spectrum at wavelength $\lambda 6500$ Å. This configuration provides a wavelength range of $\sim$4400–9200 Å, with a resolution of 11.0 Å (FWHM) at a central wavelength of 5849 Å and a dispersion of $\sim$2.6 Å pixel^{-1}. At both epochs, the spectropolarimetric observations consisted of four exposures each, with the half-wave retarder plate positioned at angles of $0°$, $45°$, $22°.5$, and $67°.5$, respectively. Exposure times at each plate angle were chosen to be 15 minutes and 2 minutes for epoch 1 and epoch 2, respectively. The spectra were flux calibrated using one 60 s integration of the photometric standard star LTT3218, with the polarimetry optics in place and the retarder plate at $0°$.

Spectra obtained at each retarder plate angle were bias subtracted, flat-field corrected, and wavelength calibrated using standard tasks within IRAF (Tody 1986, 1993). The ordinary and extraordinary beams were processed separately, and the typical rms error on the wavelength calibration gives $\sim$0.25 Å.

The Stokes parameters describe the polarization state of the electromagnetic radiation. I gives the total intensity of the beam; Q and U can be recognized by the projection of the radiation E-vectors to different directions on the plane of the sky ($+Q\leftrightarrow$, $-Q\updownarrow$, $+U\nearrow$, $-U\searrow$). Briefly speaking, the Stokes parameters Q and U can be derived via Fourier transformation, as described in the VLT FORS2 User Manual

(Anderson et al. 2018),

$$Q_0 = \frac{2}{N}\sum_{i=0}^{N-1} F(\theta_i)\cos(4\theta_i)$$
$$U_0 = \frac{2}{N}\sum_{i=0}^{N-1} F(\theta_i)\sin(4\theta_i), \qquad (A1)$$

where $F(\theta_i)$ give the normalized flux difference between the ordinary (f^o) and extraordinary (f^e) beams:

$$F(\theta_i) = \frac{f^o(\theta_i) - f^e(\theta_i)}{f^o(\theta_i) + f^e(\theta_i)}. \qquad (A2)$$

In the case of this study, four observations were carried out at retarder angles of $0°$, $22°.5$, $45°$, and $67°.5$ ($N = 4$). Therefore, $Q_0 = [F(0°) - F(45°)]/2$, and $U_0 = [F(22°.5) - F(67°.5)]/2$. The measured Stokes parameters were also corrected for the offsets to the zero angle of the retarder plate ($-\Delta\chi(\lambda)$). Typical chromatic dependence of the zero angle was less than $4°$, since a super-achromatic half-wave plate is used with FORS2 (see Figure 4.1 of the VLT FORS2 User Manual). The tabulated values are available from the FORS instrument description page.[32]

A small amount of wavelength-dependent instrumental polarization in FORS2 ($\lesssim$0.1%) has been investigated by Fossati et al. (2007) and Siebenmorgen et al. (2014). Further analytical quantification by Cikota et al. (2017) gives:

$$Q^{\mathrm{Instr.}}(\lambda) = 9.66 \times 10^{-8}\lambda + 3.29 \times 10^{-5}$$
$$U^{\mathrm{Instr.}}(\lambda) = 7.28 \times 10^{-8}\lambda - 4.54 \times 10^{-4}, \qquad (A3)$$

where λ is the observed wavelength in Å. In many cases, in order to reduce slit losses, the instrument position angle, χ, is aligned to the parallactic angle and not necessarily aligned to the north celestial meridian (i.e., $\chi \neq 0$). Therefore, the correct measurement of the polarization position angle requires transforming the Stokes parameters from the instrumental reference frame to the sky reference frame. The instrumental polarization tends to be constant among different instrument position angles (see, e.g., Figure 8 of Siebenmorgen et al. 2014) and needs to be corrected before the transformation between the instrument and sky reference frames (see, e.g., Bagnulo et al. 2017). Linear polarization measurement follows the transformation given by Equation (10) in Bagnulo et al. (2009). Therefore, we write the expression of the Stokes parameters as follows:

$$Q = (Q_0 - Q^{\mathrm{Instr.}})\cos(2\chi) + (U_0 - U^{\mathrm{Instr.}})\sin(2\chi),$$
$$U = -(Q_0 - Q^{\mathrm{Instr.}})\sin(2\chi) + (U_0 - U^{\mathrm{Instr.}})\cos(2\chi). \quad (A4)$$

We set χ to 0 deg in our observations and subtract the instrumental polarization calculated from Equation (A3) to correct the instrumental effect. The wavelength scale of the Stokes parameters and calculated polarization were also corrected to the rest frame by adopting the host-galaxy recessional velocity (1582 km s^{-1}).

---

[32] http://www.eso.org/sci/facilities/paranal/instruments/fors/inst/pola.html

Appendix B
"CMAGIC" Extinction Estimation

Following Wang et al. (2003b), we fit the linear region of the magnitude−color diagram from 5 to 27 days after the B-band maximum light with the CMAG relation:

$$B = B_{BV} + \beta_{BV}(B - V). \tag{B1}$$

Here β_{BV} and B_{BV} denote the slope and the value for the intercept at $(B - V) = 0$ of the linear region in the CMAG diagram, respectively. According to Wang et al. (2003b), the term $\mathcal{E}(B - V)$, namely "CMAGIC" color excess, is given by

$$\mathcal{E}(B - V) = \frac{(B_{\max} - B_{BV})}{\beta_{BV}}. \tag{B2}$$

The "CMAGIC" color excess for a reddening-free SN, or $\mathcal{E}_0$, also shows a dependence on the Δm_B^{15}, which characterizes the width of the light curve. By fitting a sample of SNe with little or no color excess ($B_{\max} - V_{\max} < 0.05$ mag) and also correcting that using $E(B - V)$ of Phillips et al. (1999), the linear dependence of $\mathcal{E}_0$ on Δm_{15}^B derived from this low-extinction sample of SNe Ia gives

$$\mathcal{E}_0 = (-0.118 \pm 0.013) + (0.249 \pm 0.043)(\Delta m_{15} - 1.1). \tag{B3}$$

Finally, the color excesses of SNe Ia can be estimated using the formula

$$E_{BV}(B - V) = \mathcal{E}(B - V) - \mathcal{E}_0. \tag{B4}$$

We fit the absolute B magnitude and $B - V$ color of SN 2018gv between $+5$ and $+27$ days to the CMAG relation described by Equation (B2). Both quantities have been corrected for the Galactic extinction. The result gives $\mathcal{E}^{18gv}(B - V) = -0.127 \pm 0.018$ mag, $\mathcal{E}_0^{18gv} = -0.155 \pm 0.020$ mag, and $E_{BV}^{18gv} = 0.028 \pm 0.027$ mag.

A sanity test was carried out by applying the same procedure to the B and V-band photometry of SN 2011fe published in Munari et al. (2013). In order to be consistent with our extinction estimation of SN 2018gv, we applied only the Galactic extinction, $E(B - V) = 0.01$ mag to the photometry and color of SN 2011fe based on the estimated host Na ID absorption features from high-resolution spectroscopy (Patat et al. 2013). A Cepheid distance modulus $\mu_0 = 29.04$ was used for SN 2011fe (Shappee & Stanek 2011). Finally, we conducted the CMAGIC fitting to estimate the host extinction: $\mathcal{E}^{11fe}(B - V) = -0.125 \pm 0.018$ mag, $\mathcal{E}_0^{11fe} = -0.125 \pm 0.020$ mag, and the color excess of SN 2011fe from the host gives $E_{BV}^{11fe} = 0.000 \pm 0.027$ mag. This is consistent with the evidence for very little dust extinction of SN 2011fe in its host galaxy (Patat et al. 2013; Pereira et al. 2013; Tammann & Reindl 2013; Zhang et al. 2016).

Appendix C
Steps of the Pseudo-bolometric Light-curve Construction

(1) *Extinction correction and magnitude conversion.* We correct for the Galactic extinction and the host extinction listed in Table 4 to the $UBg'Vr'i'$-band photometry of SN 2018gv. The UBV-band photometry was converted to the AB system adopting the linear offsets given in Table 1 of Blanton & Roweis (2007). Specifically, $U_{AB} = U_{Vega} + 0.79$, $B_{AB} = B_{Vega} - 0.09$, and $V_{AB} = V_{Vega} + 0.02$.

(2) *Synthetic photometry on template spectra.* We adopt the spectral template of SNe Ia built by Hsiao et al. (2007) and register the spectral templates to the nearest photometric phase. For each photometric epoch, we then perform synthetic photometry on the appropriate spectrum for the $UBg'Vr'i'$ bandpasses.

In practice, our synthetic photometry was carried out by first calculating the mean photon flux density for different bandpasses:

$$\langle \lambda F_b(\lambda) \rangle = \frac{\int \lambda F_\lambda T_b(\lambda) d\lambda}{\int \lambda T_b(\lambda) d\lambda}, \tag{C1}$$

where F_λ is the flux spectrum in unit of erg cm^{-2} s^{-1} Å^{-1} and $T_b(\lambda)$ gives the unitless throughput for a certain bandpass, which is denoted as b. Then we synthesize the magnitude in the AB system to compare with our photometry of the SN. According to the User's Guide for the PySynphot (STScI Development Team 2013), we first obtain the ST magnitude, which is similarly defined as the AB system but gives constant flux per unit wavelength interval rather than unit frequency:

$$\text{STMAG}_b = -2.5 \times \log_{10}\langle \lambda F_b(\lambda) \rangle - 21.1. \tag{C2}$$

The conversion between the ST and AB systems is given by

$$\text{ABMAG}_b = \text{STMAG}_b - 5\log_{10} \lambda_b^{\text{pivot}} + 18.692 - ZP_b. \tag{C3}$$

The source-independent pivot wavelength is defined by

$$\lambda_b^{\text{pivot}} = \sqrt{\frac{\int \lambda T_b(\lambda) d\lambda}{\int T_b(\lambda) d\lambda / \lambda}}, \tag{C4}$$

and the zero-points for $UBgVri$ bandpasses can be found in Table 3 of Pickles & Depagne (2010).

(3) *Scaling factors between template spectra and photometry.* We calculate the differences between the photometry of SN 2018gv after applying the corrections in step (1) and the synthesized AB magnitude of each template spectrum for each band obtained in step (2). The difference magnitudes were converted into flux space to obtain the scale factors between the observations of SN 2018gv and template spectra, shown in the middle panel of Figure 12. Therefore, multiplying the scale factor for each bandpass to $\langle \lambda F_b(\lambda) \rangle$ calculated from the corresponding template spectrum gives the mean photon flux density of SN 2018gv at a certain bandpass. This is shown by the filled symbols in the upper panel of Figure 12. Abscissae are given by the pivot wavelength of each bandpass calculated by Equation (C4). Three different colors and symbols illustrate the construction of the spectral energy distribution (SED) of SN 2018gv at three epochs. For each epoch, the abscissa of the leftmost and the rightmost points are determined by $\lambda_U^{\text{pivot}} - \text{FWHM}_U$ and $\lambda_i^{\text{pivot}} + \text{FWHM}_i$, respectively, while the two ordinates are assigned to $\langle \lambda F_U(\lambda) \rangle / 2$ and $\langle \lambda F_i(\lambda) \rangle / 2$, respectively.

(4) *The supernova SED.* We connect the mean photon flux density at $UBg'Vr'i'$ bandpasses and the leftmost and the rightmost boundaries described in step (3) to construct the optical SED of SN 2018gv (SED-dots), shown by the dotted lines in the upper panel of Figure 12. We also warp the template spectra using linear interpolation to the scale factors (SED-warp). The warped spectra at three epochs are also presented by the solid lines in the upper panel of Figure 12.

(5) *Integrate the SED to obtain the pseudo-bolometric luminosity.* For each epoch, we integrate the SED over the wavelength $\sim$1660–8180 Å for both SED-dots and SED-warp to calculate the pseudo-bolometric luminosity. The pseudo-bolometric luminosities of SN 2018gv before $t = 100$ days calculated using SED-warp are on average $(4.0 \pm 1.1)\%$ higher than those using SED-dots. This discrepancy results from the construction of SEDs (see Brown et al. 2016).

The errors due to photometric uncertainties of each bandpass were computed through a Monte Carlo re-sampling approach using the photometric errors. The typical error before $t = 100$ days amounts to 0.4% of the luminosity. The total error of the pseudo-bolometric luminosity is dominated by the systematical difference between the choices of the SED. We characterize this by calculating the variance between the SED-dots and SED-warp integrations. Finally, for each epoch, we add this systematical uncertainty and the error due to photometry in quadrature to obtain the final uncertainties in the pseudo-bolometric light curve. The median value of the final uncertainties is $3.0\% \pm 0.8\%$. The result of the host-galaxy extinction estimation is consistent with no extinction within the associated uncertainties (see Section 3.1 and Table 4). Therefore, we did not include the uncertainties in the estimation of the host-galaxy extinction.

Appendix D
Isp Estimation

We identify spectral regions that are likely to be intrinsically depolarized due to the overlap of many Fe absorption wings. This "line blanketing" has a significant effect on opacities, and the spectral regions are significantly depolarized since the line-blanketing opacity dominates over electron-scattering opacity. As suggested in Howell et al. (2001) and Maund et al. (2013), we start by considering the wavelength region of 4800–5600 Å (region A) and 5100–5300 Å (region B) as the intrinsically depolarized regions of SN 2018gv. We notice that there are suspicious line polarization patterns, at epoch 1, in the flux-normalized Stokes Q and U spectra (see panels (b)–(c) of Figure 14 and Section 5.4.3), possibly associated with the S II λ5454 and λ5640 lines at a velocity of $v \sim -13{,}800$ km s^{-1}. The expected effects of line blanketing, instead, appear particularly prominent at wavelengths below $\sim$5000 Å (Leonard et al. 2005). We also consider the additional wavelength region C, defined as 4800–5100 Å.

We measure the Stokes parameters by taking the error-weighted mean value across these wavelength ranges. The measured values at epoch 1 are

$$Q^A_{\text{ISP1}} = 0.19\% \pm 0.10\%, \ U^A_{\text{ISP1}} = -0.41\% \pm 0.07\%,$$
$$Q^B_{\text{ISP1}} = 0.26\% \pm 0.06\%, \ U^B_{\text{ISP1}} = -0.39\% \pm 0.08\%$$
$$Q^C_{\text{ISP1}} = 0.08\% \pm 0.07\%, \ U^C_{\text{ISP1}} = -0.37\% \pm 0.06\%. \quad \text{(D1)}$$

At epoch 2, the Stokes parameters over the same wavelength ranges are

$$Q^A_{\text{ISP2}} = 0.08\% \pm 0.12\%, \ U^A_{\text{ISP2}} = -0.49\% \pm 0.08\%,$$
$$Q^B_{\text{ISP2}} = 0.07\% \pm 0.15\%, \ U^B_{\text{ISP2}} = -0.50\% \pm 0.08\%,$$
$$Q^C_{\text{ISP2}} = 0.06\% \pm 0.13\%, \ U^C_{\text{ISP2}} = -0.48\% \pm 0.07\%. \quad \text{(D2)}$$

At epoch 1, the possible polarization associated with S II λ5454 and λ5640 makes the Stokes Q and U measured in regions A and B systematically 0.11% and 0.08% higher than those measured at epoch 2, respectively. It can be seen that Q^C_{ISP1} is consistent with Q^C_{ISP2}. For each spectral region, the measurements at both epochs are consistent within the associated uncertainties. Considering that the observation at epoch 2 achieved a higher S/N, which provides a more accurate estimate of the ISP, we adopt the error-weighted mean Stokes parameters measured over the three regions at epoch 2 to represent the Stokes parameters for the ISP: $Q_{\text{ISP}} = 0.07\% \pm 0.16\%$, $U_{\text{ISP}} = -0.49\% \pm 0.09\%$. The uncertainties were estimated by adding the average errors of the Stokes parameters over the three wavelength ranges, the standard deviation of the Stokes parameters over the three wavelength ranges, and the uncertainties of the weighted mean Stokes parameters in quadrature.

ORCID iDs

Yi Yang (杨轶) ⓘ https://orcid.org/0000-0002-6535-8500
Peter Hoeflich ⓘ https://orcid.org/0000-0002-4338-6586
Dietrich Baade ⓘ https://orcid.org/0000-0003-1637-9679
Justyn R. Maund ⓘ https://orcid.org/0000-0003-0733-7215
Peter. J. Brown ⓘ https://orcid.org/0000-0001-6272-5507
Heloise F. Stevance ⓘ https://orcid.org/0000-0002-0504-4323
Iair Arcavi ⓘ https://orcid.org/0000-0001-7090-4898
Aleksandar Cikota ⓘ https://orcid.org/0000-0001-7101-9831
Avishay Gal-Yam ⓘ https://orcid.org/0000-0002-3653-5598
Melissa. L. Graham ⓘ https://orcid.org/0000-0002-9154-3136
Daichi Hiramatsu ⓘ https://orcid.org/0000-0002-1125-9187
Griffin Hosseinzadeh ⓘ https://orcid.org/0000-0002-0832-2974
D. Andrew Howell ⓘ https://orcid.org/0000-0003-4253-656X
Saurabh W. Jha ⓘ https://orcid.org/0000-0001-8738-6011
Curtis McCully ⓘ https://orcid.org/0000-0001-5807-7893
Ferdinando Patat ⓘ https://orcid.org/0000-0002-0537-3573
David. J. Sand ⓘ https://orcid.org/0000-0003-4102-380X
Steve Schulze ⓘ https://orcid.org/0000-0001-6797-1889
Jason Spyromilio ⓘ https://orcid.org/0000-0001-6815-4055
Stefano Valenti ⓘ https://orcid.org/0000-0001-8818-0795
József Vinkó ⓘ https://orcid.org/0000-0001-8764-7832
Xiaofeng Wang ⓘ https://orcid.org/0000-0002-7334-2357
J. Craig Wheeler ⓘ https://orcid.org/0000-0003-1349-6538
Ofer Yaron ⓘ https://orcid.org/0000-0002-0301-8017
Jujia Zhang ⓘ https://orcid.org/0000-0002-8296-2590

References

Anderson, J., et al. 2018, European Southern Observatory, Very Large Telescope Paranal Science Operations FORS2 User Manual, Doc. No. VLT-MAN-ESO-13100-1543, http://www.eso.org/sci/facilities/paranal/instruments/fors/doc/VLT-MAN-ESO-13100-1543_P03.pdf
Appenzeller, I., Fricke, K., Fürtig, W., et al. 1998, Msngr, 94, 1
Arnett, W. D. 1969, AP&SS, 5, 180
Arnett, W. D. 1982, ApJ, 253, 785
Bagnulo, S., Cox, N. L. J., Cikota, A., et al. 2017, A&A, 608, A146
Bagnulo, S., Landolfi, M., Landstreet, J. D., et al. 2009, PASP, 121, 993
Bellm, E. C., Kulkarni, S. R., Graham, M. J., et al. 2019, PASP, 131, 018002
Benetti, S., Cappellaro, E., Mazzali, P. A., et al. 2005, ApJ, 623, 1011
Benz, W., Bowers, R. L., Cameron, A. G. W., & Press, W. H. 1990, ApJ, 348, 647
Blanton, M. R., & Roweis, S. 2007, AJ, 133, 734
Blondin, S., & Tonry, J. L. 2007, ApJ, 666, 1024
Bloom, J. S., Kasen, D., Shen, K. J., et al. 2012, ApJL, 744, L17

Branch, D., Baron, E., Hall, N., Melakayil, M., & Parrent, J. 2005, PASP, 117, 545

Branch, D., Jeffery, D. J., Young, T. R., & Baron, E. 2006, PASP, 118, 791

Branch, D., & Wheeler, J. C. 2017, Supernova Explosions (Berlin: Springer)

Breeveld, A. A., Landsman, W., Holland, S. T., et al. 2011, in AIP Conf. Ser. 1358, Gamma Ray Bursts 2010, ed. J. E. McEnery, J. L. Racusin, & N. Gehrels (Melville, NY: AIP), 373

Brown, P. J., Breeveld, A., Roming, P. W. A., & Siegel, M. 2016, AJ, 152, 102

Brown, P. J., Breeveld, A. A., Holland, S., Kuin, P., & Pritchard, T. 2014, A&SS, 354, 89

Bulla, M., Sim, S. A., Kromer, M., et al. 2016a, MNRAS, 462, 1039

Bulla, M., Sim, S. A., Pakmor, R., et al. 2016b, MNRAS, 455, 1060

Burns, C. R., Stritzinger, M., Phillips, M. M., et al. 2011, AJ, 141, 19

Cao, Y., Kulkarni, S. R., Howell, D. A., et al. 2015, Natur, 521, 328

Cardelli, J. A., Clayton, G. C., & Mathis, J. S. 1989, ApJ, 345, 245

Childress, M. J., Filippenko, A. V., Ganeshalingam, M., & Schmidt, B. P. 2014, MNRAS, 437, 338

Chonis, T. S., Hill, G. J., Lee, H., et al. 2016, Proc. SPIE, 9908, 99084C

Chugai, N. N. 1992, SvAL, 18, 168

Cikota, A., Patat, F., Cikota, S., & Faran, T. 2017, MNRAS, 464, 4146

Cikota, A., Patat, F., Wang, L., et al. 2019, MNRAS, 490, 578

Conley, A., Howell, D. A., Howes, A., et al. 2006, AJ, 132, 1707

Contreras, C., Phillips, M. M., Burns, C. R., et al. 2018, ApJ, 859, 24

Crawford, S. M., Still, M., Schellart, P., et al. 2010, Proc. SPIE, 7737, 25

Davenport, J. d. M. W. T. D. 2018, pydis: Possibly Useful, Zenodo, doi:10.5281/zenodo.58753

Davies, R. L., Allington-Smith, J. R., Bettess, P., et al. 1997, Proc. SPIE, 2871, 1099

De, K., Kasliwal, M. M., Polin, A., et al. 2019, ApJL, 873, L18

Diamond, T. R., Hoeflich, P., & Gerardy, C. L. 2015, ApJ, 806, 107

Dimitriadis, G., Foley, R. J., Rest, A., et al. 2019, ApJL, 870, L1

Edwards, Z. I., Pagnotta, A., & Schaefer, B. E. 2012, ApJL, 747, L19

Eriguchi, Y., & Mueller, E. 1993, ApJ, 416, 666

Fausnaugh, M. M., Vallely, P. J., Kochanek, C. S., et al. 2019, arXiv:1904.02171

Fesen, R. A., Höflich, P. A., Hamilton, A. J. S., et al. 2007, ApJ, 658, 396

Fink, M., Röpke, F. K., Hillebrandt, W., et al. 2010, A&A, 514, A53

Firth, R. E., Sullivan, M., Gal-Yam, A., et al. 2015, MNRAS, 446, 3895

Folatelli, G., Phillips, M. M., Burns, C. R., et al. 2010, AJ, 139, 120

Folatelli, G., Phillips, M. M., Morrell, N., et al. 2012, ApJ, 745, 74

Fossati, L., Bagnulo, S., Mason, E., & Landi Degl'Innocenti, E. 2007, in ASP Conf. Ser. 364, The Future of Photometric, Spectrophotometric and Polarimetric Standardization, ed. C. Sterken (San Francisco, CA: ASP), 503

Fukugita, M., Ichikawa, T., Gunn, J. E., et al. 1996, AJ, 111, 1748

Gamezo, V. N., Khokhlov, A. M., & Oran, E. S. 2004, PhRvL, 92, 211102

Gamezo, V. N., Khokhlov, A. M., & Oran, E. S. 2005, ApJ, 623, 337

Ganeshalingam, M., Li, W., & Filippenko, A. V. 2011, MNRAS, 416, 2607

Garavini, G., Folatelli, G., Nobili, S., et al. 2007, A&A, 470, 411

García-Berro, E., Badenes, C., Aznar-Siguán, G., & Lorén-Aguilar, P. 2017, MNRAS, 468, 4815

García-Berro, E., & Lorén-Aguilar, P. 2017, in Dynamical Mergers, ed. A. W. Alsabti & P. Murdin (Cham: Springer), 1237

García-Berro, E., Lorén-Aguilar, P., Aznar-Siguán, G., et al. 2012, ApJ, 749, 25

Garg, A., Stubbs, C. W., Challis, P., et al. 2007, AJ, 133, 403

Gehrels, N., Chincarini, G., Giommi, P., et al. 2004, ApJ, 611, 1005

Goldhaber, G., Groom, D. E., Kim, A., et al. 2001, ApJ, 558, 359

González Hernández, J. I., Ruiz-Lapuente, P., Tabernero, H. M., et al. 2012, Natur, 489, 533

Hayden, B. T., Garnavich, P. M., Kessler, R., et al. 2010, ApJ, 712, 350

Henden, A. A., Templeton, M., Terrell, D., et al. 2016, yCat, 2336, 0

Hillebrandt, W., Kromer, M., Röpke, F. K., & Ruiter, A. J. 2013, FrPhy, 8, 116

Hoeflich, P. 2017, in Handbook of Supernovae, ed. A. W. Alsabti & P. Murdin (Cham: Springer), 1151

Hoeflich, P., Hsiao, E. Y., Ashall, C., et al. 2017, ApJ, 846, 58

Hoeflich, P., & Khokhlov, A. 1996, ApJ, 457, 500

Hoeflich, P., Khokhlov, A. M., & Wheeler, J. C. 1995, ApJ, 444, 831

Hoeflich, P., Wheeler, J. C., Hines, D. C., & Trammell, S. R. 1996, ApJ, 459, 307

Höflich, P. 1991, A&A, 246, 481

Höflich, P., Gerardy, C. L., Fesen, R. A., & Sakai, S. 2002, ApJ, 568, 791

Höflich, P., Gerardy, C. L., Marion, H., & Quimby, R. 2006, NewAR, 50, 470

Höflich, P., & Stein, J. 2002, ApJ, 568, 779

Hosseinzadeh, G., Sand, D. J., Valenti, S., et al. 2017, ApJL, 845, L11

Howell, D. A. 2011, NatCo, 2, 350

Howell, D. A., Höflich, P., Wang, L., & Wheeler, J. C. 2001, ApJ, 556, 302

Hoyle, F., & Fowler, W. A. 1960, ApJ, 132, 565

Hristov, B., Collins, D. C., Hoeflich, P., Weatherford, C. A., & Diamond, T. R. 2018, ApJ, 858, 13

Hsiao, E. Y., Conley, A., Howell, D. A., et al. 2007, ApJ, 663, 1187

Iben, I., Jr., & Tutukov, A. V. 1984, ApJS, 54, 335

Itagaki, K. 2018, TNSTR, 57, 1

Jiang, J.-A., Doi, M., Maeda, K., et al. 2017, Natur, 550, 80

Jiang, J.-A., Doi, M., Maeda, K., & Shigeyama, T. 2018, ApJ, 865, 149

Johnson, H. L. 1966, ARA&A, 4, 193

Jordi, K., Grebel, E. K., & Ammon, K. 2006, A&A, 460, 339

Kasen, D. 2010, ApJ, 708, 1025

Kasen, D., Nugent, P., Wang, L., et al. 2003, ApJ, 593, 788

Kasen, D., Thomas, R. C., & Nugent, P. 2006, ApJ, 651, 366

Katz, M. P., Zingale, M., Calder, A. C., et al. 2016, ApJ, 819, 94

Khokhlov, A. M. 1991, A&A, 245, 114

Krisciunas, K., Contreras, C., Burns, C. R., et al. 2017, AJ, 154, 211

Kromer, M., Sim, S. A., Fink, M., et al. 2010, ApJ, 719, 1067

Kushnir, D., Katz, B., Dong, S., Livne, E., & Fernández, R. 2013, ApJL, 778, L37

Leonard, D. C., Li, W., Filippenko, A. V., Foley, R. J., & Chornock, R. 2005, ApJ, 632, 450

Li, W., Bloom, J. S., Podsiadlowski, P., et al. 2011, Natur, 480, 348

Li, W., Wang, X., Vinkó, J., et al. 2019, ApJ, 870, 12

Livne, E. 1990, ApJL, 354, L53

Lorén-Aguilar, P., Isern, J., & García-Berro, E. 2009, A&A, 500, 1193

Maguire, K., Sullivan, M., Thomas, R. C., et al. 2011, MNRAS, 418, 747

Maoz, D., Mannucci, F., & Nelemans, G. 2014, ARAA, 52, 107

Marion, G. H., Brown, P. J., Vinkó, J., et al. 2016, ApJ, 820, 92

Maund, J. R., Höflich, P., Patat, F., et al. 2010, ApJL, 725, L167

Maund, J. R., Spyromilio, J., Höflich, P. A., et al. 2013, MNRAS, 433, L20

Maund, J. R., Wheeler, J. C., Baade, D., et al. 2009, ApJ, 705, 1139

Maund, J. R., Wheeler, J. C., Patat, F., et al. 2007, MNRAS, 381, 201

Mazzali, P. A., Benetti, S., Altavilla, G., et al. 2005, ApJL, 623, L37

McCully, C., Volgenau, N. H., Harbeck, D.-R., et al. 2018, Proc. SPIE, 10707, 107070K

Miller, A. A., Cao, Y., Piro, A. L., et al. 2018, ApJ, 852, 100

Milne, P. A., Williams, G. G., Porter, A., et al. 2017, ApJ, 835, 100

Moll, R., Raskin, C., Kasen, D., & Woosley, S. E. 2014, ApJ, 785, 105

Mulligan, B. W., & Wheeler, J. C. 2018, MNRAS, 476, 1299

Mulligan, B. W., Zhang, K., & Wheeler, J. C. 2019, MNRAS, 484, 4785

Munari, U., Henden, A., Belligoli, R., et al. 2013, NewA, 20, 30

Munari, U., & Zwitter, T. 1997, A&A, 318, 269

Niemeyer, J. C., Hillebrandt, W., & Woosley, S. E. 1996, ApJ, 471, 903

Nomoto, K. 1982a, ApJ, 257, 780

Nomoto, K. 1982b, ApJ, 253, 798

Nomoto, K., Sugimoto, D., & Neo, S. 1976, Ap&SS, 39, L37

Nugent, P., Baron, E., Branch, D., Fisher, A., & Hauschildt, P. H. 1997, ApJ, 485, 812

Nugent, P. E., Sullivan, M., Cenko, S. B., et al. 2011, Natur, 480, 344

Olling, R. P., Mushotzky, R., Shaya, E. J., et al. 2015, Natur, 521, 332

Pakmor, R., Hachinger, S., Röpke, F. K., & Hillebrandt, W. 2011, A&A, 528, A117

Pakmor, R., Kromer, M., Röpke, F. K., et al. 2010, Natur, 463, 61

Pakmor, R., Kromer, M., Taubenberger, S., et al. 2012, ApJL, 747, L10

Pakmor, R., Kromer, M., Taubenberger, S., & Springel, V. 2013, ApJL, 770, L8

Parrent, J. T., Thomas, R. C., Fesen, R. A., et al. 2011, ApJ, 732, 30

Patat, F., Baade, D., Höflich, P., et al. 2009, A&A, 508, 229

Patat, F., Cordiner, M. A., Cox, N. L. J., et al. 2013, A&A, 549, A62

Patat, F., Höflich, P., Baade, D., et al. 2012, A&A, 545, A7

Patat, F., & Romaniello, M. 2006, PASP, 118, 146

Penney, R., & Hoeflich, P. 2014, ApJ, 795, 84

Pereira, R., Thomas, R. C., Aldering, G., et al. 2013, A&A, 554, A27

Perlmutter, S., Aldering, G., Goldhaber, G., et al. 1999, ApJ, 517, 565

Phillips, M. M., Lira, P., Suntzeff, N. B., et al. 1999, AJ, 118, 1766

Pickles, A., & Depagne, É. 2010, PASP, 122, 1437

Piersanti, L., Tornambé, A., & Castellani, V. 2004, MNRAS, 353, 243

Plewa, T., Calder, A. C., & Lamb, D. Q. 2004, ApJL, 612, L37

Porter, A. L., Leising, M. D., Williams, G. G., et al. 2016, ApJ, 828, 24

Poznanski, D., Ganeshalingam, M., Silverman, J. M., & Filippenko, A. V. 2011, MNRAS, 415, L81

Quimby, R. M., Wheeler, J. C., Höflich, P., et al. 2007, ApJ, 666, 1093

Ramsey, L. W., Adams, M. T., Barnes, T. G., et al. 1998, Proc. SPIE, 3352, 34

Rasio, F. A., & Shapiro, S. L. 1994, ApJ, 432, 242

Raskin, C., Kasen, D., Moll, R., Schwab, J., & Woosley, S. 2014, ApJ, 788, 75

Reilly, E., Maund, J. R., Baade, D., et al. 2016, MNRAS, 457, 288

Reinecke, M., Hillebrandt, W., & Niemeyer, J. C. 2002, A&A, 391, 1167
Remming, I. S., & Khokhlov, A. M. 2014, ApJ, 794, 87
Ricker, G. R., Winn, J. N., Vanderspek, R., et al. 2015, JATIS, 1, 014003
Riess, A. G., Filippenko, A. V., Challis, P., et al. 1998, AJ, 116, 1009
Riess, A. G., Filippenko, A. V., Li, W., et al. 1999, AJ, 118, 2675
Riess, A. G., Macri, L. M., Hoffmann, S. L., et al. 2016, ApJ, 826, 56
Riess, A. G., Rodney, S. A., Scolnic, D. M., et al. 2018, ApJ, 853, 126
Roming, P. W. A., Kennedy, T. E., Mason, K. O., et al. 2005, SSRv, 120, 95
Röpke, F. K. 2007, ApJ, 668, 1103
Saio, H., & Nomoto, K. 1985, A&A, 150, L21
Saio, H., & Nomoto, K. 1998, ApJ, 500, 388
Sato, Y., Nakasato, N., Tanikawa, A., et al. 2016, ApJ, 821, 67
Scalzo, R., Aldering, G., Antilogus, P., et al. 2014, MNRAS, 440, 1498
Schlafly, E. F., & Finkbeiner, D. P. 2011, ApJ, 737, 103
Science Software Branch at STScI 2012, PyRAF: Python Alternative for IRAF,
    Astrophysics Source Code Library, ascl:1207.011
Segretain, L., Chabrier, G., & Mochkovitch, R. 1997, ApJ, 481, 355
Seitenzahl, I. R., Ciaraldi-Schoolmann, F., Röpke, F. K., et al. 2013, MNRAS,
    429, 1156
Serkowski, K., Mathewson, D. S., & Ford, V. L. 1975, ApJ, 196, 261
Shapiro, P. R., & Sutherland, P. G. 1982, ApJ, 263, 902
Shappee, B. J., Holoien, T. W. S., Drout, M. R., et al. 2019, ApJ, 870, 13
Shappee, B. J., Prieto, J. L., Grupe, D., et al. 2014, ApJ, 788, 48
Shappee, B. J., & Stanek, K. Z. 2011, ApJ, 733, 124
Shen, K. J., Kasen, D., Weinberg, N. N., Bildsten, L., & Scannapieco, E. 2010,
    ApJ, 715, 767
Shen, K. J., & Moore, K. 2014, ApJ, 797, 46
Siebenmorgen, R., Voshchinnikov, N. V., & Bagnulo, S. 2014, A&A,
    561, A82
Siebert, M. R., Dimitriadis, G., & Foley, R. J. 2018, TNSCR, 75, 1
Silverman, J. M., & Filippenko, A. V. 2012, MNRAS, 425, 1917
Silverman, J. M., Kong, J. J., & Filippenko, A. V. 2012, MNRAS, 425, 1819
Silverman, J. M., Vinkó, J., Marion, G. H., et al. 2015, MNRAS, 451, 1973
Sim, S. A., Seitenzahl, I. R., Kromer, M., et al. 2013, MNRAS, 436, 333
Smith, M. P., Nordsieck, K. H., Burgh, E. B., et al. 2006, Proc. SPIE, 6269,
    62692A
Smitka, M. T., Brown, P. J., Suntzeff, N. B., et al. 2015, ApJ, 813, 30
Stevance, H. F., Maund, J. R., Baade, D., et al. 2017, MNRAS, 469, 1897
Stevance, H. F., Maund, J. R., Baade, D., et al. 2019, MNRAS, 485, 102
Stritzinger, M., & Leibundgut, B. 2005, A&A, 431, 423

STScI Development Team 2013, pysynphot: Synthetic Photometry Software
    Package, Astrophysics Source Code Library, ascl:1303.023
Taam, R. E. 1980, ApJ, 242, 749
Tammann, G. A., & Reindl, B. 2013, A&A, 549, A136
Tanaka, M., Mazzali, P. A., Benetti, S., et al. 2008, ApJ, 677, 448
Tartaglia, L., Sand, D. J., Valenti, S., et al. 2018, ApJ, 853, 62
Thomas, R. C., Aldering, G., Antilogus, P., et al. 2011, ApJ, 743, 27
Tody, D. 1986, Proc. SPIE, 627, 733
Tody, D. 1993, in ASP Conf. Ser. 52, Astronomical Data Analysis Software
    and Systems II, ed. R. J. Hanisch, R. J. V. Brissenden, & J. Barnes (San
    Francisco, CA: ASP), 173
Tonry, J. L. 2011, PASP, 123, 58
Tully, R. B. 2015, AJ, 149, 171
Valenti, S., Sand, D., Pastorello, A., et al. 2014, MNRAS, 438, L101
van de Hulst, H. C. 1957, Light Scattering by Small Particles (New York:
    Wiley)
Walker, E. S., Baltay, C., Campillay, A., et al. 2015, ApJS, 219, 13
Wang, L., Baade, D., Höflich, P., et al. 2003a, ApJ, 591, 1110
Wang, L., Baade, D., Höflich, P., et al. 2006, ApJ, 653, 490
Wang, L., Baade, D., & Patat, F. 2007, Sci, 315, 212
Wang, L., Goldhaber, G., Aldering, G., & Perlmutter, S. 2003b, ApJ, 590, 944
Wang, L., Howell, D. A., Höflich, P., & Wheeler, J. C. 2001, ApJ, 550, 1030
Wang, L., & Wheeler, J. C. 1996, ApJL, 462, L27
Wang, L., & Wheeler, J. C. 2008, ARA&A, 46, 433
Wang, L., Wheeler, J. C., & Höflich, P. 1997, ApJL, 476, L27
Wang, X., Filippenko, A. V., Ganeshalingam, M., et al. 2009, ApJL, 699, L139
Wang, X., Wang, L., Filippenko, A. V., et al. 2012, ApJ, 749, 126
Webbink, R. F. 1984, ApJ, 277, 355
Whelan, J., & Iben, I., Jr. 1973, ApJ, 186, 1007
Woosley, S. E., & Weaver, T. A. 1994, ApJ, 423, 371
Woosley, S. E., Weaver, T. A., & Taam, R. E. 1980, in Texas Workshop on
    Type I Supernovae, ed. J. C. Wheeler (Fort Davis, TX: Univ. Texas), 96
Yaron, O., & Gal-Yam, A. 2012, PASP, 124, 668
Yoon, S.-C., Podsiadlowski, P., & Rosswog, S. 2007, MNRAS, 380, 933
Yoshida, S. 2019, MNRAS, 486, 2982
Zhai, Q., Zhang, J.-J., Wang, X.-F., et al. 2016, AJ, 151, 125
Zhang, K., Wang, X., Zhang, J., et al. 2016, ApJ, 820, 67
Zhao, X., Wang, X., Maeda, K., et al. 2015, ApJS, 220, 20
Zheng, W., Filippenko, A. V., Mauerhan, J., et al. 2017, ApJ, 841, 64
Zheng, W., Silverman, J. M., Filippenko, A. V., et al. 2013, ApJL, 778, L15